# Silicon Nanowire Based Sensors for Bacterial Tests

YINGTAO YU

UPPSALA
UNIVERSITET

**Abstract**

Yu, Y. 2023. Silicon Nanowire Based Sensors for Bacterial Tests. *Digital Comprehensive Summaries of Uppsala Dissertations from the Faculty of Science and Technology* 2326. 95 pp. Uppsala: Acta Universitatis Upsaliensis. ISBN 978-91-513-1935-3.

Rapid and reliable antibiotic susceptibility testing (AST) is urgently required to diagnose bacterial infectious diseases and avoid antibiotic misuse, providing valuable information on the efficacy of antibiotic agents and their dosages for treatment. However, the currently employed phenotypic ASTs normally demand the growth of bacteria into colonies, which usually takes more than two days. In this thesis, silicon nanowire field-effect transistors (SiNWFETs) are emploied to realize rapid ASTs, and a novel suspended SiNW-net sensor is also developed as a potential device platform for bacterial motility detection.

The thesis first introduces SiNWFET sensors for rapid ASTs. The extracellular pH change generated by bacterial metabolism is an efficient indicator of bacterial activity, which is monitored by our SiNWFET sensors. Rapid ASTs are achieved by using SiNWFET sensors array with a total assay time of less than 30 minutes for different bacterial strains. As a follow-up, the metabolic response of E. coli under ampicillin treatment is systematically studied. When exposed to bactericidal antibiotics, the bacterial respiration rate will be accelerated, thereby enhancing the lethality of the antibiotics. This work demonstrates the capabilities of SiNWFETs for rapid ASTs and bacterial metabolism investigations.

To further improve the detection limit of SiNWFET, Schottky junction gated SiNWFET (SJGFET) is developed, in which the noisy Si channel/gate oxide interface is replaced by a PtSi/Si junction. Ultra-low low-frequency noise is demonstrated in SJGFETs fabricated on high-quality bonded silicon-on-insulator (SOI) substrate. The best achieved $S_{vg}$ are $1.2 \times 10^{-10}$ and $1.1 \times 10^{-11}$ V$^2$μm$^2$/Hz at 1 Hz and 10 Hz, respectively. Then, a thorough investigation of low-frequency noise (LFN) is performed using the CNF + CMF model specifically modified for SJGFET structure on SOI substrate. The observed LFN dependence on substrate voltage and channel width is mainly ascribed to the nonuniform energy distribution of interface traps.

For the purposes of bacterial mobility detection, we propose a novel SiNW-net-based nanoelectromechanical sensor, with a 30-μm suspended SiNW-net and a metal Lorentz loop stacked on top. The lock-in amplifier measurement setup is optimized to significantly reduce the system noise. During rapid thermal processing in the device fabrication, lateral boron autodoping is discovered, which happens via ambient diffusion limited by the redeposition step at the interface. This technique enables shallow junction formation and will be integrated into SiNW-net fabrication to form well-controlled piezoresistors.

*Keywords:* silicon nanowire, field-effect transistor, antibiotic susceptibility test, bacterial metabolism, nanoelectromechanical sensor, multiplexed detection

*Yingtao Yu, Department of Electrical Engineering, Solid-State Electronics, Box 65, Uppsala University, SE-751 03 Uppsala, Sweden.*

*To those in mind*

# List of Papers

This thesis is based on the following papers, which are referred to in the text by their Roman numerals.

I.     Xu, X., Chen, S., **Yu, Y**., Virtanen, P., Wu, J., Hu, Q., Koskiniemi, S., Zhang, Z. (2022) All-Electrical Antibiotic Susceptibility Testing within 30 Min Using Silicon Nano Transistors. *Sens. Actuators B Chem.*, *357*, 131458.

II.     **Yu, Y.**, Jones, A., Alhoush, G., Koskiniemi, S., Zhang, Z. (2023) Scrutinize early metabolic response of E. coli to ampicillin treatment using nanoscale silicon transistors, *in manuscript.*

III.     **Yu, Y.**, Chen, S., Hu, Q., Solomon, P., Zhang, Z. (2021) Ultra-Low Noise Schottky Junction Tri-Gate Silicon Nanowire FET on Bonded Silicon-on-Insulator Substrate. *IEEE Electron Device Lett.*, *42* (4), 469–472.

IV.     **Yu, Y.**, Zhang, Z., Chen, S. (2022) Analysis of Low Frequency Noise in Schottky Junction Trigate Silicon Nanowire FET on Bonded SOI Substrate. *IEEE Trans. Electron Devices*, *69* (8), 4667–4673.

V.     **Yu, Y**., Gauthier, N., Primetzhofer, D., Zhang, Z. (2023) Shallow Junction Formation via Lateral Boron Autodoping during Rapid Thermal Process. *J. Phys. Appl. Phys.*, *56* (45), 45LT01.

Reprints were made with permission from the respective publishers.

# Author's Contributions

I      Fabricated the SiNWFETs sensors. Participated in system calibration and wrote part of the manuscript.

II     Planned and performed SiNWFETs sensor fabrication, bacterial tests, data analysis, and manuscript writing.

III    Planned and performed the device fabrication and characterization, and data analysis, and wrote part of the manuscript.

IV    Planned and performed the device fabrication, model development, and data interpretation, and wrote the manuscript.

V     Planned and performed the device fabrication, characterization, model building, and data analysis, and wrote the manuscript.

# List of Papers Not Included in the Thesis

I     Xu, X., **Yu, Y.**, Hu, Q., Chen, S., Nyholm, L., and Zhang, Z., (2021) "Redox Buffering Effects in Potentiometric Detection of DNA Using Thiol modified Gold Electrodes," *ACS sensors*, 6, 2546-2552.

# Contents

# Abbreviations

| | |
|---|---|
| $A$ | Gate area |
| ACK | Acetate kinase |
| adhE | Aldehyde-alcohol dehydrogenase |
| ADP | Adenosine diphosphate |
| AFM | Atomic Force Microscopy |
| ALD | Atomic layer deposition |
| AMP | Ampicillin |
| ATP | Adenosine triphosphate |
| atpA | ATP synthase subunit alpha |
| AST | Antibiotic susceptibility test |
| $C_{BOX}$ | Capacitance of BOX |
| $C_{EDL}$ | EDL capacitance |
| CEF | Cefotaxime |
| CIP | Ciprofloxacin |
| $C_{it}$ | Capacitance of interface traps |
| $C_m$ | Boron gas phase concentration |
| CMF | Correlated mobility fluctuation |
| CNF | Carrier number fluctuation |
| COMS | Complementary metal-oxide-semiconductor |
| $C_{Si}$ | Capacitance of Si channel |
| D | Drain |
| $D$ | Diffusivity |
| $E$ | Young's modules |
| $\vec{E}$ | Electric field |
| $E.\ coli$ | Escherichia coli |
| EBL | Electron beam lithography |
| EDL | Electrical double layer |
| Etest | Epsilometer testing |
| $F$ | Force |
| $f$ | Frequency |
| $FEM$ | Finite elements method |
| FGA | Forming gas annealing |

| | |
|---|---|
| G | Gate |
| $G$ | Piezoresistance gauge factor |
| GEN | Gentamicin |
| $g_m$ | Transconductance |
| $h$ | Height |
| HF | Hydrofluoric acid |
| HMF | Hooge mobility fluctuation |
| HSQ | Hydrogen silsesquioxane |
| $I$ | Second moment of area |
| $I_{DS}$ | Drain-to-source current |
| IG | Gate leakage current |
| ISFET | Ion-sensitive field-effect transistor |
| JFET | Junction gated FET |
| $\vec{j}$ | Current density |
| $k$ | Boltzmann constant |
| $k_e$ | Effective segregation coefficient |
| $L$ | Length |
| LAMP | Loop-mediated isothermal amplification |
| LB | Luria-Bertani broth |
| LFN | Low frequency noise |
| LOD | Limit of detection |
| $LPF$ | Low pass filter |
| $M$ | Bending moment |
| MEMS | Microelectromechanical systems |
| MIC | Minimum inhibitory concentration |
| MOSFET | Metal-oxide-semiconductor field-effect transistor |
| $N(t)$ | Cell number |
| $n(x)$ | Carrier density at position $x$ |
| ND | Dopants concentration |
| NEMS | Nanoelectromechanical system |
| $N_t(E_{fn})$ | Trap density at quasi-Fermi level |
| $N_{total}$ | Total carrier number |
| OCR | Oxygen consumption rate |
| PBPs | Penicillin-binding proteins |
| PCR | Polymerase chain reaction |
| PDH | pyruvate dehydrogenase |
| PDMS | Polydimethylsiloxane |
| PEP | Phosphoenolpyruvate |
| PFL | Pyruvate formate lyase |

| | |
|---|---|
| PL | Photoluminescence |
| PSD | Power spectrum density |
| PTA | Phosphotransacetylase |
| $q$ | Elemental charge |
| R | Resistance |
| RE | Reference electrode |
| $R_H(t)$ | Proton generation rate |
| RIE | Reactive ion etching |
| RMS | Root mean square |
| ROS | Reactive oxygen species |
| RTP | Rapid thermal processing |
| S | Source |
| SEM | Scanning electron microscope |
| $S_{id}$ | Drain current power spectrum density |
| SIMOX | Separated by implantation of oxygen |
| SiNW | Silicon nanowire |
| SiNWFET | Silicon nanowire field-effect transistor |
| SJGFET | Schottky junction gated SiNWFET |
| SMU | Source measure units |
| SOI | Silicon-on-insulator |
| SPR | Surface plasmon resonance |
| SS | Subthreshold swings |
| $S_{vfb}$ | Flat-band voltage power spectrum density |
| $S_{vg}$ | Gate-referred voltage noise |
| $T$ | Temperature |
| $t$ | Time |
| TCA | Tricarboxylic acid cycle |
| ToF-SIMS | Time-of-flight secondary ion mass spectroscopy |
| $t_{Si}$ | Height of channel |
| UTI | Urinary tract infection |
| $V_{bi}$ | Build-in potential |
| $V_D$ | Drain voltage |
| $V_G$ | Gate voltage |
| $V_{sub}$ | Substrate voltage |
| $V_T$ | Threshold voltage |
| $w$ | Width |
| WT | Wild type |
| $Z$ | Section modules |
| $\alpha_H$ | Hooge parameter |

| | |
|---|---|
| $\beta_{\text{int}}$ | Intrinsic buffer capacity |
| $\gamma$ | Attenuation coefficient of the electron in oxide |
| $\varepsilon_{\text{Si}}$ | Dielectric constant of silicon |
| $\theta$ | Phase |
| $\mu_{\text{c}}$ | Coulomb scattering limited mobility |
| $\mu_{\text{sr}}$ | Surface roughness scattering limited mobility |
| $\Pi$ | Piezoresistive coefficient tensor |
| $\varphi_{\text{s}}$ | Surface potential |
| $\lambda$ | Poison's ratio |
| $\rho$ | Resistivity |
| $\tau$ | Doubling time |
| $\epsilon$ | Strain |
| $\Delta_{max}$ | Maximum deflection |

# 1. Introduction

## 1.1 Development of antibiotics and emergency of antimicrobial resistance

The antibiotic revolution was launched by Sir Alexander Fleming (1881-1955), who discovered penicillin on a contaminated Petri dish in 1928 [1]. Then, Ernst Chain and Howard Florey purified the first penicillin, penicillin G, in 1942 [2], and became widely available outside the Allied military in 1945. The history of
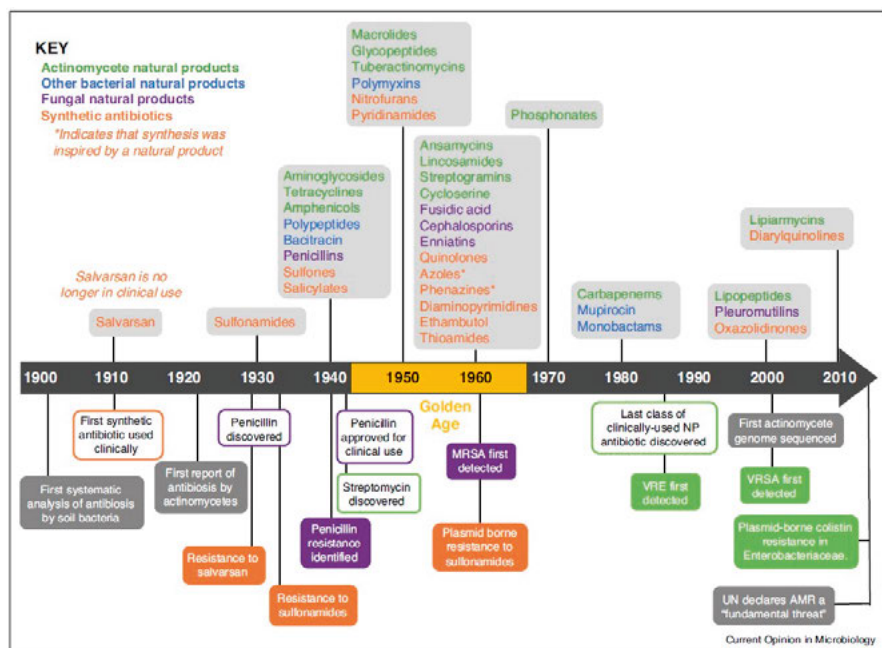


*Figure 1.1. Timeline showing the decade new classes of antibiotic reached the clinic. The antibiotics are colored per their source: green = actinomycetes, blue = other bacteria, purple = fungi and orange = synthetic. Reprinted with persimsion from [3]. Copyright (2019) Elsevier Current Opinion in Microbiology.*

antibiotics is illustrated in Fig. 1.1 [3]. Since the beginning of the antibiotic era, the average human life span increased from 47 years in 1900 to 76.4 years in 2021, US [4]. There is no doubt that antibiotic is one of the most successful forms of chemotherapy in the history of medicine.

However, with the massive usage of antibiotics, antibiotic resistance emerged and was becoming one of the biggest threats to global health [5], [6]. Antibiotic resistance, which is defined microbiologically as the presence of genetically determined resistance mechanism, can be acquired by naturally susceptible bacteria via genetic mutation or transfer from other bacteria [7]. The antibiotic resistance genes carried by mobile genetic elements, such as plasmid and transposons, can be transferred by conjugation, transduction, or transformation [8]. Under the pressure of antibiotics, the antibiotic-resistant mutated strains become more competitive and have survival advantage in this selection. These mutated bacteria can pass on the antibiotic genes to other bacteria, leading to the spreading of antibiotic resistance. Worse still, the misuse of antibiotics, like suboptimal dose treatment, further promotes the resistance selection and leads to the dominance of resistant strains.

Nowadays, antibiotic resistance is becoming more and more challenging. In the early antibiotic era, new antibiotics could be easily developed to replace the resisted antibiotics. But now, multidrug-resistant organisms become increasingly common, resulting in difficult-to-treat or even untreatable infections with conventional antimicrobials[9]. It is estimated that deaths from drug-resistant infections will increase from 0.7 to 10 million worldwide annually by 2050 unless a global response is initiated [10]. The increasing prevalence of drug-resistant bacteria in the community forces physicians to either risk treatment failure with older antibiotics or use effective last-resort antibiotics, which will rapidly drive resistance to these drugs.

## 1.2 Development and status of rapid AST

To diagnose bacterial infectious diseases and avoid antibiotic misuse, antimicrobial susceptibility testing (AST) is imperative, which can provide valuable information on the efficacy of antibiotic agents and their dosages for treatment [11]–[13]. Since early and effective treatment is crucial to avoid costly and perhaps even lethal complications (such as septic infections) for most infectious

diseases, rapid ASTs are greatly desired for quick selection of effective drugs to treat infections at early stage. Since the discovery and utilization of antibiotics, AST was also proposed and developed significantly until now, as summarized in Fig. 1.2 [14].
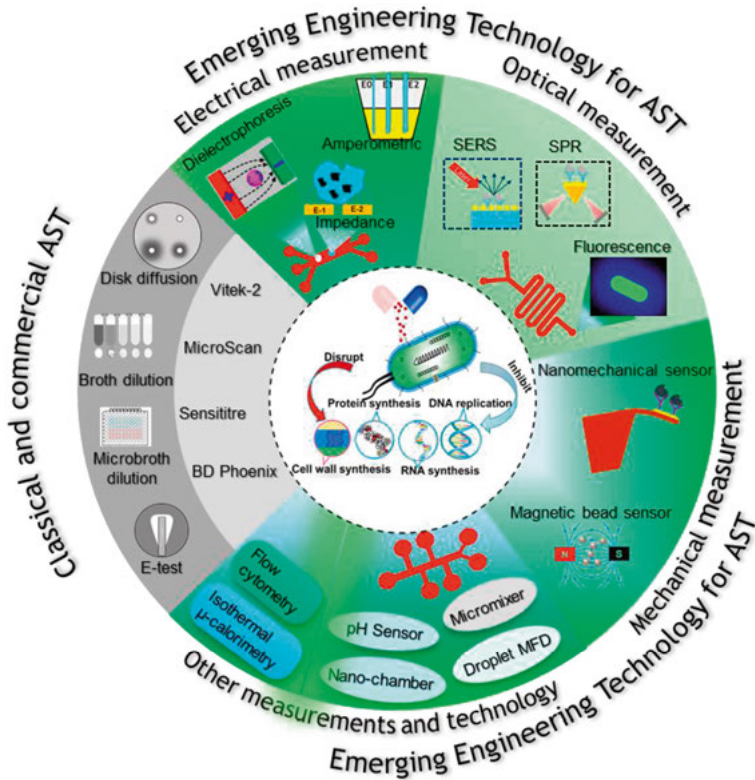


*Figure 1.2. Summary and highlights of existed techniques for AST applications. Reprinted with permission from [14]. Copyright (2019) Elsevier Biosensors and Bioelectronics.*

The conventional AST methods can be categorized into phenotype and genotype. For phenotype AST methods, the disk diffusion method introduced by Bauer and Kirby [15] is the gold standard for determining the susceptibility of bacteria. In the diffusion method, the incubated bacterial suspension is inoculated onto a solidified agar plate impregnated with antibiotics. After overnight incubation, the antibiotic will diffuse from the filter paper into the ager, and form inhibition zone around the paper disc. The size of the inhibition zone is a direct measurement of the susceptibility of the bacteria to the antibiotic [16]. The diffusion method has the advantages of low cost, simplicity, and

intuitiveness. However, it generally takes 16-24 hours to determine the susceptibility and is haunted by inaccuracy from evaporation, sterilization, and cumbrous operation. In addition, for many infectious diseases, retrieving bacterial samples of adequate amount for the tests is also a major challenge. This usually demands a pre-cultivation step for at least 1 day before starting the ASTs.

Dilution using broth and agar is one of the oldest methods to determine the minimum inhibitory concentration (MIC) of antibiotic [17]. In the broth dilution method, the bacteria are incubated in micro-centrifuge tubes with two-fold diluted antibiotics overnight. The turbidity of the culture is examined to determine the MIC. Similarly, in the agar dilution method, a certain number of bacteria are incubated on an agar plate containing diluted concentrations of antibiotic. The antibiotic efficacy can be examined by counting the spots on plate after overnight incubation. The dilution method requires a large volume of reagents. In addition, tedious operation, cross-contamination, and long incubation time also limit its application.

Epsilometer testing (Etest) that combines the principle of both diffusion and dilution methods was also developed to determine MIC [18]. In this procedure, plastic strips with pre-defined antibiotic concentrations are placed on streaked agar plate. After overnight incubation, the intersection of the growth inhibition ellipse zone and strip edge indicates the MIC of antibiotics [19]. This method is well-known for its sensitivity and simplicity, however, it's expensive for large-scale ASTs and incompatible with certain antibiotics, such as Penicillin, ciprofloxacin, ofloxacin, and rifampicin [20].

In contrast to phenotypic ASTs, genotypic ASTs are based on the direct detection of specific genetic markers associated with resistance (resistance genes, mutations) using standard molecular biology tools such as Polymerase chain reaction (PCR)[21], DNA microarray and DNA chips [22], and loop-mediated isothermal amplification (LAMP) [23]. Genotypic methods can avoid overnight bacteria incubation and cross-contamination, thus improving the efficiency and sensitivity of susceptibility tests. However, there are several drawbacks that diminish the usage of genotypic methods [24]. For instance, the detected resistance genes are not always associated with the actual resistance, due to coincidental mutations which will lead to false positives. And those unidentified resistance genetic mechanisms are unable to be determined. In addition, genotypic methods require expensive reagents and instruments, demanding skilled operators.

To simplify the test procedure and achieve rapid AST, extensive efforts have been invested in developing rapid AST approaches, with many emerging techniques generated in the last decade. Optical measurements have been involved in rapid ASTs. For instance, Raman spectroscopy, which measures molecular vibration and relies on inelastic scattered photons, can provide information on biomolecules and profile the phenotypic response of bacteria to antibiotics [25]. Laser tweezers combined with Raman spectroscopy, principal component analysis, and power spectrum density analysis were applied to trap single cells [26]. Then the morphological change can be evaluated to identify bacterial species and study metabolic activity. Other optical techniques, such as surface plasmon resonance (SPR) [27], optical path difference [28], photoluminescence (PL) [29], direct single-cell imaging [30], *etc*., were also investigated for rapid ASTs. Although these optical approaches have capabilities of high sensitivity, label-free, and real-time detection, they still suffer from high costs and complicated optical systems.

Electrical biosensing, featuring an accessible, rapid, label-free, and reliable technique, plays a more and more important role in emerging ASTs. Many of those techniques have been transplanted to ASTs, such as dielectrophoresis [31], impedance spectroscopy [32], amperometry biosensors [33], etc. In this work, we were utilizing silicon nanowire field-effect transistor (SiNWFET) to real-time monitor the metabolism of bacteria under the presence of different antibiotics, by measuring the metabolism induced pH change in the growth media. Since this method does not require the change of cell number or morphology, it is significantly faster than the traditional cell culturing methods. Label-free AST within 30 min has been demonstrated in this thesis work. *Escherichia coli* (*E. coli*) metabolic response under ampicillin treatment is also investigated using our SiNWFETs, attributing to its sensitivity and real-time monitoring capability. In addition, the nanoscale size of SiNWFETs could allow the analysis of extremely small volumes, via their integration with microscale culturing chambers (around 100 picoliters, assuming a chamber size of 50 µm × 50 µm × 50 µm). Even a single bacterial cell in such a small volume will make an effective cell concentration of $10^7$/mL, which is sufficiently high to generate detectable pH signal for ASTs. This can potentially facilitate direct testing of the real UTI samples with no need for pre-cultivation.

The motility of bacteria, as a phenotypic indicator, has been investigated for rapid AST using nanomechanical sensors as an emerging approach in the last

decade. Atomic Force Microscopy (AFM) cantilever was applied to study the micro-motions of bacteria [34]. The vibration from motile cells can be transferred to the amplitude of dynamic cantilever fluctuation with capability of real-time measurement. Benefiting from the high sensitivity of AFM tips, the characterization of motility of cells becomes reality, and the susceptibility of antibiotics can be determined within 10 minutes. However, this method relies on expensive instruments and lacks portability.

In this thesis, a novel suspended silicon nanowire net (SiNW-net) based nanoelectromechanical sensor (NEMS) was developed for bacterial motility measurements to achieve rapid ASTs. The CMOS-compatible SiNW-net can be integrated on chip, with low cost and high portability. The complicated optical detecting system in AFM is replaced by a piezoresistive Si resistor in a simple Wheatstone bridge designed for electrical measurement, which can simplify the signal processing and further reduce the cost for ASTs.

## 1.3 Device introduction

The advance of nanofabrication techniques has boosted enormous developments of nanoelectronics sensors, which feature their ability of label-free, rapid, and real-time sensing [35]–[37]. Additionally, the high-density integration with low production costs further promotes the wide application of nanoelectronics sensors. In this thesis, SiNWFET is applied to achieve rapid ASTs, and a novel suspended SiNW-net is also developed as a potential device platform to monitor bacterial motility. These devices are introduced in the following sections.

### 1.3.1 SiNWFET sensor

A conventional metal-oxide-semiconductor field-effect transistor (MOSFET) fabricated on silicon-on-insulator (SOI) substrate is depicted in Fig. 1.3 (a) (top), with three terminals, source (S), drain (D), and gate (G). The gate terminal is isolated from the channel with gate dielectric. The voltage bias applied to the metal gate ($V_G$) can modulate the potential energy thus the density of the charged carriers in the channel between the source and drain. Therefore, the channel current from source to drain ($I_{DS}$) driven by drain voltage ($V_D$) can be efficiently modulated by $V_G$ as illustrated in Fig. 1.3(a).

By replacing the metal gate with an electrolyte and adding an ion sensing layer at the device/liquid interface, an ion-sensitive FET (ISFET) can be achieved, as shown in Fig. 1.3 (b) (bottom).
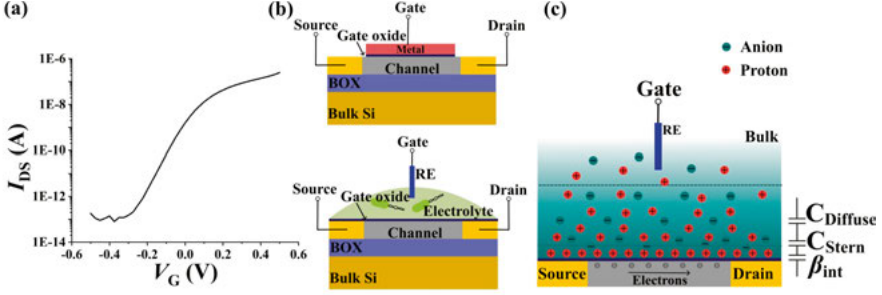


Figure 1.3. (a) a typical $I_{DS}$ vs. $V_G$ curve of MOSFET. (b) Schematics of MOSFET and ISFET, and (c)electrical double layer.

The $V_G$ on the liquid gate is normally applied by a reference electrode (RE), as illustrated in Fig. 1.3 (c). For $p$H sensing, the gate oxide can act as the sensing layer. The -OH group on the oxide surface can selectively interact with $H^+$ ions in the liquid sample, via the following reversible surface reactions [38]–[40]:

$$M - OH \leftrightarrow M - O^- + H_s^+ \qquad (1.1)$$
$$M - OH_2^+ \leftrightarrow M - OH + H_s^+ \qquad (1.2)$$
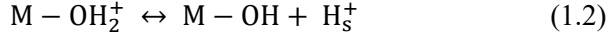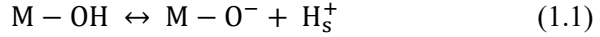
where $H_s^+$ denotes the surface $H^+$. Depending on the pH value, the surface reactions can move either forward or reverse, thus changing the total amount of net charge on the sensing surface. Therefore, the potential drop across the electrical double layer (EDL) formed at the solid-liquid interface changes with pH, which generates the original signal in pH sensing, the change of the surface potential ($\Delta\varphi_s$). The pH signal on an ISFET sensor was well described with the side-binding model[39], where the dynamic equilibrium between the –OH group on the surface and $H^+$ ions can buffer the $p$H change at the surface ($pH_s$). This buffering effect is represented by the intrinsic buffer capacity ($\beta_{int}$), which is an equivalent capacitance connected with EDL capacitance ($C_{EDL}$) in series (see Fig. 1.3(c)). The change of bulk $p$H ($pH_b$) will induce $\Delta\varphi_s$ across $C_{EDL}$, described as [38], [41]

$$\frac{\Delta\varphi_s}{\Delta pH_b} = -2.3\alpha\frac{kT}{q}, \text{with}\alpha = \frac{1}{\frac{2.3kTC_{EDL}}{q^2\beta_{int}}+1}, \qquad (1.3)$$

where $k$ is the Boltzmann constant, $T$ is the temperature, and $q$ is the elemental charge. For an ideal oxide surface with infinite $\beta_{int}$, $\alpha$ equals 1, and equation (1.3)

is written as

$$\frac{\Delta\varphi_s}{\Delta pH_b} = -2.3\frac{kT}{q}. \qquad (1.4)$$

The equation (1.4) indicates that one order of magnitude change of bulk H$^+$ concentration can generate surface potential change of $2.3kT/q$ = 59.2 mV at room temperature, called as the Nernstian response limit [38].

For the bacteria tests using SiNWFET, *E. coli* cells are incubated in a container on top of SiNWFET sensors with D-glucose as the carbon source. The cell metabolism transfers D-glucose to acetate via the glucose overflow mechanism[42], [43]. The released acetate changes bulk *p*H in the culturing media, which could be precisely monitored by the SiNWFET sensors. Therefore, SiNWFET sensors can be used to real-time monitor the metabolism of bacteria cells under the presence of the different antibiotics.

## 1.3.2 Suspended SiNW-net based NEMS sensor

Bacteria actively move around in liquid environments with the thrust generated by their powerful rotating flagellar motor [44], [45]. Despite the structural diversity of the flagella among bacterial species, those bacteria share a common rotary motor located at the base of the filament. The motor is fueled by an inward-directed electrochemical gradient of protons or sodium ions across the cytoplasmic membrane[46] and can generate a maximum rotational speed of 300 revolutions per second in *E. coli* and *Salmonella* and 1700 revolutions per second in a *marine bacterium* [47]. The rotational speed of the flagellar motor is much higher than that of a manufactured car engine such as the Formula one car. Rapid AST was recently demonstrated by determining bacterial viability (life or death) from their motions.

NEMS based on suspended SiNWs represents the next stage in the miniaturization of microelectromechanical systems (MEMS) sensors, with higher sensitivity and lower energy consumption [48]. The reported giant piezoresistancce effect  also highlig{Citation}hts the advantage of SiNW in potential applications in NEMS [49]. In this thesis, a fully suspended SiNW net NEMS is designed and demonstrated, aiming to detect bacterial motility based on the giant piezoresistive effect in the SiNW.

The estimated force generated by a single *E. coli* cell is approximately at *p*N level [34], [50], [51]. To detect bacterial motility, the SiNW-net device must be engineered for extremely high force sensitivity. The piezoresistive signal

correlated to strain can be represented as [52]

$$\frac{\Delta R}{R} = G \times \epsilon, \text{ with } G = 1 + 2\lambda + \frac{\Delta \rho / \rho}{\epsilon} \quad , \tag{1.5}$$

in which R and $\rho$ are the resistance and resistivity, and G, $\epsilon$, and $\lambda$ are piezoresistance gauge factor, strain, and Poison's ratio, respectively. In metal gauges, the first two terms $(1 + 2\lambda)$, represent the dominant change in resistance due to dimensional changes. However, the resistivity variation term (the third term) is much larger than the dimensional term by about a factor of 50 in semiconductor gauges [52]. The resistivity piezo gauge factor is determined by the material lattice properties. The strain ($\epsilon$) generated by loading force, depends on the mechanical property and the geometry structure of the device. Therefore, the signal output can be enhanced by increasing the strain via device's geometry optimization. Here, we take a suspended SiNW beam with fixed ends as an example to illustrate the strain dependence of beam dimension.
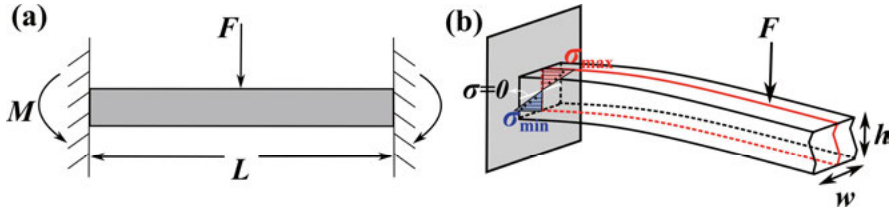


*Figure 1.4. Schematics of (a) double clamped SiNW beam under loading force (F), and (b) bending stress distribution on vertical cross-section at one of the fixed ends.*

As shown in Fig. 1.4, a suspended SiNW with length ($L$), width ($w$), and height ($h$) is loaded with force ($F$) at middle of the beam. The bending moment ($M$) at the fixed end and maximum deflection ($\Delta_{max}$) at center can be calculated with

$$M_{end} = \frac{F \times L}{8}, \text{ and } \Delta_{max} = \frac{F \cdot L^3}{192 E \cdot I}, \tag{1.6}$$

where $E$ is Young's modules, and $I$ is the second moment of area. The stress distributed in the vertical cross-section is presented in Fig. 1.4 (b), in which the stress is neutral at the middle plane and raises to the maximum value ($\sigma_{max}$) at the top surface, whereas decreases to minimum value ($\sigma_{min}$) at the bottom surface. The maximum stress can be calculated with cross-section parameters via $\sigma = M/Z$, in which $Z$ is the section modulus equals to $wh^2/6$ for a rectangle cross-section. Therefore, the $\sigma_{max}$ can be extracted from eq. (1.6) as

$$\sigma_{max} = \frac{3}{4} \cdot \frac{FL}{wh^2}.\tag{1.7}$$

Eq. (1.7) clearly expresses that the bending stress at fixed ends is determined by the dimension of SiNW. It is linearly proportional to length, but reversely proportional to width and square of height. Guided by these conclusions, we designed the SiNW-net as presented in Fig. 1.5. To improve the stress gain of
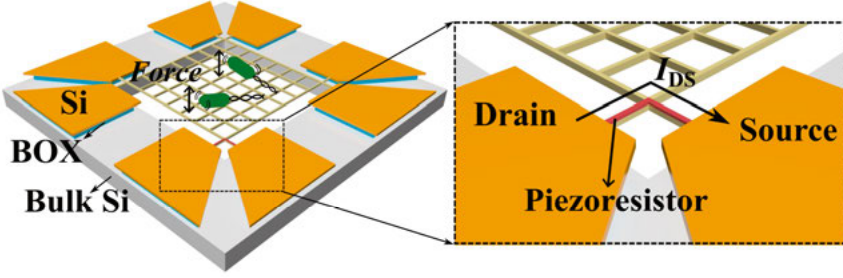


*Figure 1.5. Schematic of suspended SiNW-net and zoom-in view of piezoresistor on fixed end.*

piezoresistor, first of all, the piezoresistor is placed at the stress-concentrated region, top surface on SiNW at the fixed end. Secondly, the device is fabricated on an SOI substrate with 55 nm thickness of top silicon. The width of the SiNW is shrunk to 100 nm, and a 30-um-length SiNW-net is successfully suspended with our fabrication process. Considering the damping from liquid culture in real tests, the device is designed as a network, which might also capture live bacteria during measurement.

# 1.4 Thesis organization

The main focus of this thesis is to explore rapid ASTs with SiNW-based sensors. Chapter 2 demonstrates rapid AST results based on multiplexed SiNWFET array. In Chapter 3, the SiNWFET is optimized by replacing gate oxide with PtSi Schottky junction. The ultra-low low frequency noise is systematically analyzed with an optimized CNF+CMF model. Chapter 4 introduces a SiNW-based NEMS designed for bacterial motility tests.

A brief summary of papers listed in this thesis is presented as following. In **paper I,** we demonstrate rapid ASTs using SiNWFET sensors. Our sensors profile bacterial metabolic kinetics by monitoring the metabolism induced acidification in the growth media with the absence and the presence of different antibiotics. Rapid AST results could be determined from the metabolic profiles with a total assay time less than 30 minutes. In **paper II,** with this powerful transistor array system, *E. coli* metabolic early response under ampicillin treatment is studied. The possible mechanism of metabolism dependence on ampicillin is investigated. **In paper III and IV**, ultra-low noise Schottky junction tri-gated SiNWFETs are achieved by replacing the noisy gate oxide/semiconductor interface with Schottky junction and optimizing bottom BOX/silicon interface to eliminate carrier trapping/detrapping processes at both interfaces. However, the LFN dependence on device width and substrate bias ($V_{sub}$) indicates that the BOX/silicon interface is still the major noise source. Then, the low frequency noise (LFN) in SJGFETs fabricated on bonded SOI substrate is systematically analyzed with an optimized CNF+CMF model. **Paper V** presents a novel boron lateral autodoping in normal rapid thermal process (RTP) and used it to controllably form shallow junctions for device fabrication. The autodoping process is systematically characterized and simulated. It could potentially be used to form the piezoelements in our suspended SiNW net based NEMS sensor to detect bacterial motility.

# 2. Antibiotic Susceptibility Test on Multiplexed Nano Transistor Array

Under the threat posed by multidrug-resistant organisms with heightened lethality, rapid and reliable antibiotic susceptibility testing (AST) holds immense importance for selecting effective drug to treat infections at the early stage. The most widely used tests in clinical practice are traditional phenotypic ASTs. However, the currently employed phenotypic ASTs in clinics normally require the growth of bacteria into colonies on culture media in the presence of different antibiotics. This procedure needs at least 25 generations of growth and usually takes more than two days. In addition, for many infectious diseases, retrieving bacterial samples of adequate amounts for the tests is also a major challenge. This usually demands a precultivation step for at least one day before starting the ASTs. Even with the most recent modern rapid AST protocol, the traditional test still takes too long for patients to wait for therapy. In this chapter, a SiN-WFET-based AST method is introduced with insight into its working principle and rapid AST demonstration. Benefit from the high sensitivity of the SiN-WFET sensor, the early metabolic response of *E. coli* under ampicillin treatment is carefully investigated, revealing some interesting aspects of the killing mechanism of ampicillin.

## 2.1 pH change in the growth media induced by bacterial metabolism

pH change in the growth media has been widely observed during bacterial incubation. Depending on the species of carbon source, the direction of pH shift can be reversed. For instance, extracellular pH decreases if glucose, glycerol, or octanoate are used as carbon sources. However, the growth media becomes alkalinized with more oxidized carbon sources, such as citrate, 2-furoate, and 2-oxoglutarate [53]. The carbon sources participate in cell metabolism including respiration and anabolism, *etc*., and release organic acid, amines, or small

molecules like ammonia and protons. Therefore, extracellular pH change can serve as a real-time indicator of bacteria activity with specific carbon sources and is thus applied in ASTs.

In our work, the pH response from *E. coli* MG1655 was monitored with abundant glucose as the carbon source. As a commonly used carbon source, D-glucose metabolic pathways were well-understood [43]. In Fig. 2.1, the central metabolic pathway is presented. After the uptake of glucose by transporter protein, it is converted to pyruvate through glycolysis, experiencing phosphoenolpyruvate (PEP). Subsequently, the pyruvate is transformed to acetyl-CoA through either pyruvate dehydrogenase (PDH) enzyme or pyruvate formate lyase (PFL). Depending on the oxygen condition in the medium, the metabolic pathway will be altered. In an anaerobic environment, the lactate dehydrogenase (LDH) pathway will be activated to generate lactate accompanied by PFL which forms acetyl-CoA and formate, so-called mixed acid fermentation. However, in the oxygen-rich condition, pyruvate will be converted to acetyl-CoA through PDH, then acetyl-CoA enters the tricarboxylic acid cycle (TCA) as citrate [54]. The TCA cycle, also well-known as Krebs cycle and citric acid cycle, is the second stage of cellular respiration, by which acetyl-CoA is oxidized to $CO_2$, generating ATP as energy fuel with the consumption of $H_2O$ and $O_2$ [55].
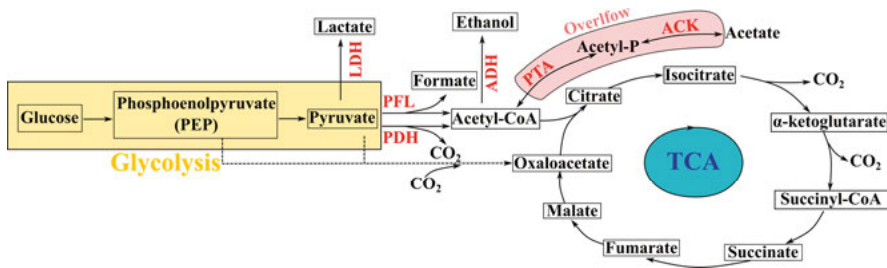


*Figure 2.1. Schematic of central metabolic pathways of E. coli.*

When specific glucose uptake exceeds its maximum respiration rate, the extra acetyl-CoA will be converted to acetate via phosphotransacetylase (PTA) and acetate kinase (ACK). This process is reversible and called the overflow mechanism, which takes around 9% of carbon of the glucose consumed [56]. Therefore, the bacterial respiration and activity can be effectively reflected by overflow acetate concentration, and detected by means of pH monitoring on our SiNWFET. In this thesis work, we have successfully demonstrated real-time metabolism monitoring using a minimal amount of bacterial samples within the

testing container, demonstrating the reliability of our SiNWFET for rapid ASTs.

## 2.2 SiNWFET fabrication and multiplexed sampling system

Our SiNWFET array was fabricated on a silicon-on-insulator (SOI) substrate, using fully CMOS-compatible process. To realize real-time $p$H monitoring with high accuracy, both the device and signal readout system were specifically designed.

In the aspect of SiNWFET device, some features such as high $p$H response, low leakage current, and proper working voltage range are highly required. To satisfy these requirements, certain process steps are optimized as below. First, the gate oxide over the SiNW channel, which serves as $H^+$ ions sensing layer and isolator, is one of the most critical parts of the device. $HfO_2$ as a broadly used high-$k$ dielectric material is selected as gate oxide coated via atomic layer deposition (ALD) ending with 5 nm thickness. The high relative constant (18 ~ 25) results in greatly improved gate oxide capacitance (around five times higher



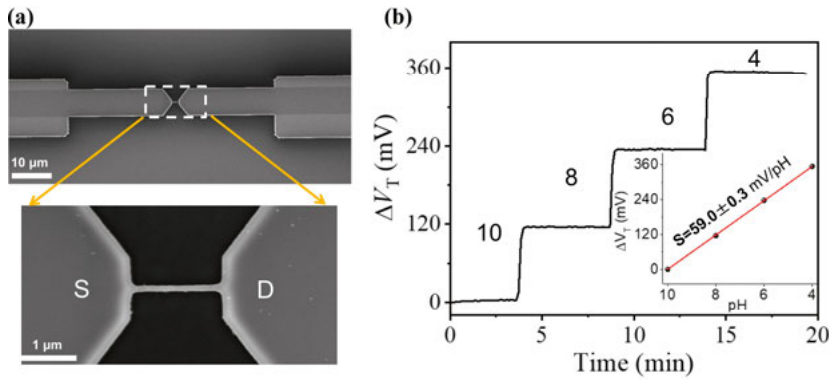*Figure 2.2. (a) SEM image of SiNWFET (upper) and its zoom-in channel region (lower). (b) $\Delta V_T$ vs. t curve for a SiNWFET measured in buffer solutions with pH changing from 10 to 4. Inset: SiNWFET sensitivity calibration curve, i.e., $\Delta V_T$ vs. pH. Note that each data point is averaged from three independent measurements and error bars representing standard deviations are also included in the inset.*

than SiO$_2$ with the same thickness), thus the voltage signal generated by pH change is less shared by gate capacitance (mostly couple to the channel). As an oxide layer, HfO$_2$ also shows good pH sensitivity and linearity [57], [58], and it can also effectively suppress the leakage current down to $10^{-11}$ A. Second, the SiNW channel was downscaled to 100 nm width for a higher surface aspect ratio as shown in Fig. 2.2(a). Since the device is operated in the aqueous medium with a reference electrode (RE), parasitic electrochemistry reactions such as water electrolysis on RE must be avoided. Therefore, the working gate voltage region is set below the water electrolysis voltage (1.23 V) by optimizing the channel and S/D dopants level. More detailed processing information can be found in **Paper I**. Finally, the threshold voltage ($V_T$) of the SiNWFET shifts positively with decreasing pH, showing a near-Nernstian response with a sensitivity of $59.0 \pm 0.3$ mV/pH (see Fig. 2.2(b)).

The experimental setup is shown in Fig. 2.3(a). The SiNWFET chip is placed on a metal stage heated up to 37 °C and stabilized by a feedback temperature controller. A PDMS container on chips contains 150 uL of medium biased by
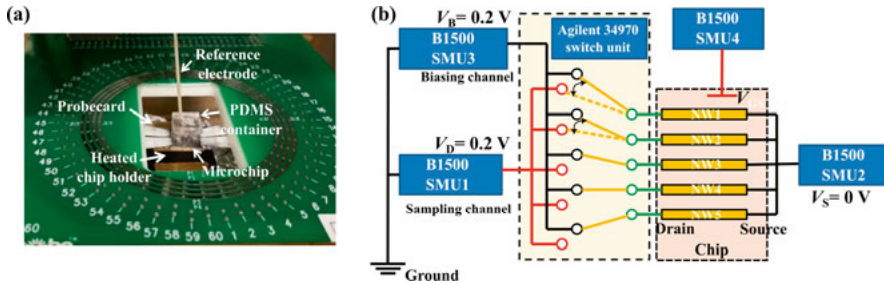


Figure 2.3. (a) photo image of experimental setup during bacteria culturing. (b) schematic of the multiplexed sampling system.

an Ag/AgCl reference electrode. To measure several devices in parallel, a switch unit (Agilent 34970) is incorporated between SiNWFETs and the source measure units (SMU), as illustrated in the schematic in Fig. 2.3(b). During the measurement, all the chosen devices are connected in parallel and biased via SMU to ensure they remain in working condition. When a particular device is selectively read out, the switch unit will reroute the drain terminal of the device to the sampling channel. Since the bias conditions remain unchanged after switching, the transient charging current can be greatly reduced. By sweeping switches periodically, multiplexed sampling is executed on selected devices. To ensure measurement accuracy while maintaining an acceptable sweeping

speed, four devices are monitored simultaneously in all of our measurements. The results are then averaged and plotted with standard error bars.

All experimental runs are in the following protocol. Bacteria were cultured overnight in LB medium at 37 °C, with agitation at 200 rpm. The chip was connected to the measurement setup via a probe card, and the transfer charac-
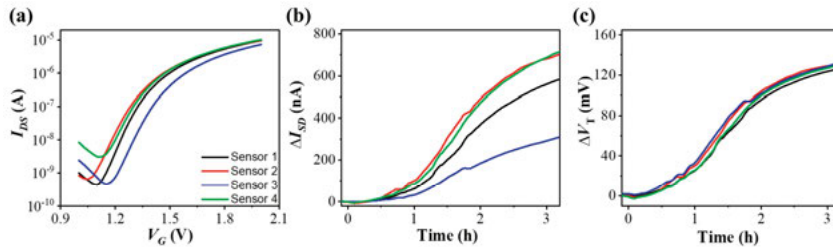


*Figure 2.4. (a) Transfer curves of 4 SiNWFETs measured in the culture medium (LB + 1 wt. % glucose). (b) $\Delta I_{DS}$ versus t, and (c) converted $\Delta V_T$ versus t sampling curves with initial E.coli density of $5 \times 10^7$ cfu/mL.*

teristics (Fig. 2.4(a)), as well as the $\Delta I_{DS}$ vs. time (Fig. 2.4(b)), were recorded with only the culture medium (LB + 1wt% glucose, 80 µL) at 37°C until a stable baseline was established. Subsequently, 100 µL of the bacterial sample was centrifuged at 1950 g (relative centrifugal force) for 3 min and then re-suspended in 20 µL of fresh culture medium. Next, 20 µL of the bacterial sample, either with or without antibiotics, was injected into the 80 µL culture medium, and the $I_{DS}$ vs. time curve was monitored. Because the transconductance varies over different devices, the current sampling results are then converted to threshold voltage shifting ($\Delta V_T$) according to the corresponding transfer curves. The converted $\Delta V_T$ signal aligns very well (see Fig. 2.4(c)) indicating that the medium inside the container is uniform and the sensitivity of each device remains consistent.

## 2.3 Rapid ASTs within 30 min using SiNWFETs

### 2.3.1 Rapid AST for *E. coli*

*E. coli*, a typical Gram-negative bacterial strain, normally lives in the intestines and gut of some animals. Some *E. coli* strains can cause diarrhea from contaminated food, and 75 to 95% of urinary tract infections. In this work, *E. coli* K12 MG1655 is selected as the model pathogen due to its well-established model and well-characterized genetics. The susceptibility of *E. coli* to three antibiotics, namely ampicillin (AMP), cefotaxime (CEF), and ciprofloxacin (CIP), was first investigated. The initial concentration of E. coli employed in this measurement was $2.2 \times 10^9$ cfu/mL, as confirmed through parallel cell plating. Figs. 2.5(a), (b), and (c) display $\Delta V_T$ vs. *t* curves for the susceptible *E. coli* in response to 100 mg/L (33 × MIC) AMP, 20mg/L (22 × MIC) CEF, and 1mg/L (125 × MIC) CIP, respectively. The reference curves without antibiotics show continuous growth, indicating decreased *p*H due to organic acid released from living *E. coli*. In contrast, the antibiotic treatment curves for susceptible *E. coli* significantly deviate from reference results within 25 minutes, demonstrating the
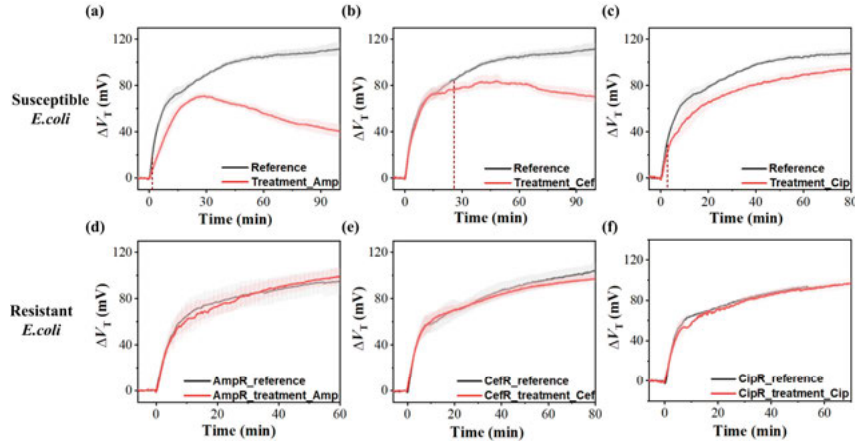


*Figure 2.5. $\Delta V_T$ as a function of t for susceptible E. coli treated with different antibiotics: (a) AMP (100 mg/L), (b) CEF (20mg/L), and (c) CIP (1mg/L). Resistant E. coli ASTs with corresponding antibiotics: (d), (e) and (f). The shade area represents the standard deviation calculated from 3 biological replicates with each replicate being averaged with data from 3 to 4 sensors. The AST response time is marked with dashed lines in (a), (b), and (c).*

rapid AST capability of our SiNWFETs sensors. As anticipated, the deviations are absent in resistant *E. coli* ASTs as shown in Fig. 2.5(d), (e), and (f). These

results evidence that our SiNWFETs could clearly distinguish susceptible and resistant bacterial strains.

In addition to susceptibility, Fig. 2.5 also exhibits distinct profiles for susceptible *E. coli* under different antibiotic treatments, which may indicate different killing mechanisms. AMP and CEF, belonging to β-lactam antibiotics, can disrupt bacterial cell wall synthesis by inhibiting the activity of Penicillin-binding proteins (PBPs) [59], ultimately causing the bacteria to lose their structural integrity, and leading to bacterial cell death. The lysed *E. coli* under AMP and CEF treatment could release their cytoplasm, leading to alkalization of the medium. As a result, the increased pH was observed indicated by a decrease in $\Delta V_T$. Compared with CEF, AMP-treated susceptible *E. coli* shows faster onset of bactericidal action and a higher killing rate, which could be attributed to their different binding affinity to corresponding PBPs. Inspired by the distinct patterns under antibiotic treatment, our SiNWFETs hold great promise for the investigation of bacterial metabolism and antibiotic killing mechanisms. The detailed study will be introduced in the later section.

## 2.3.2 AST for Gram-positive bacteria

To demonstrate the universality of our SiNWFET-based AST method, Gram-positive bacterial strains, i.e., *S. aureus* and *S. saprophyticus*, were also studied. The incubation curves without antibiotics are depicted in Fig. 2.6(a). In contrast to *E. coli*, *S. aureus* and *S. saprophyticus* behave in different $\Delta V_T$ slopes, indicating varying rates of acidification in the following order: *E. coli* > *S. aureus*
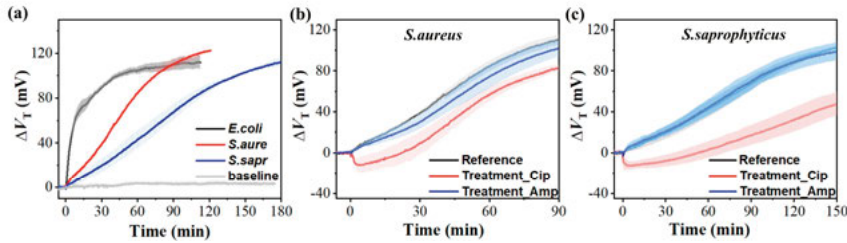


Figure 2.6. (a) $\Delta V_T$ vs. time curves of E. coli, S. aureus, and S. saprophyticus with corresponding initial concentration of $2.2 \times 10^9$, $2.5 \times 10^9$ and $3.6 \times 10^9$ cfu/mL. CIP (4 mg/L) and AMP (100 mg/L) ASTs results for S. aureus and S. saprophyticus in (b) and (c) with reference measurement without antibiotic.

> *S. saprophyticus*. Both *S. aureus* and *S. saprohuticus* were treated with CIP and AMP for ASTs, as shown in Fig. 2.6(b) and (c). Under CIP treatment, DNA

replication and reparation would be hindered as shown by the immediate $\Delta V_T$ drop and slower acidification (red lines). However, no significant variations were detected between the reference (black lines) and AMP-treated samples (blue lines) in Fig. 2.6(b) and (c) within the measurement duration. In contrast to *E. coli*, the response of *S. aureus* and *S. saprophyticus* to AMP was delayed, which could be attributed to the thicker cell wall of Gram-positive bacteria requiring longer lysis time. To verify this hypothesis, OD600 measurements were conducted, revealing that it took 70 and 125 min, respectively, for AMP to impact the growth of *S. aureus* and *S. saprophyticus* (see **Paper I**).

### 2.3.3 Analysis of E. coli metabolic dynamics during growth

With our SiNWFET sensor, the real-time *p*H response from *E. coli* was precisely monitored. In this section, an analysis model of $H^+$ concentration is developed to describe the metabolic kinetics during bacterial growth.

The $H^+$ concentration in the medium at time *t*, $H(t)$ can be calculated through

$$H(t) = H_0 \cdot 10^{\Delta V_T(t)/S}, \tag{2.1}$$

in which $H_0$ is the initial $H^+$ concentration, $6 \times 10^{16}$ $H^+/L$ for *p*H = 7.0, and S is the pH sensitivity. The calculated $H(t)$ is plotted in Fig. 2.7.(b). By differentiate (2.1), the acidification rate can be derived as

$$R_H(t) = \frac{H_0 \cdot 10^{\Delta V_T(t)/S}}{S} \cdot \frac{d\Delta V_T(t)}{dt}. \tag{2.2}$$

$R_H(t)$ is also correlated with cell number ($N(t)$) and $H^+$ production rate per cell ($v$) via

$$R_H(t) = N(t) \cdot v. \tag{2.3}$$

For ASTs with the saturation cell density, $2 \times 10^9$ cfu/mL, the cell number remains constant during testing, whereas cells in log-growth phase with lower density can be described as

$$N(t) = N_0 \cdot 2^{t/\tau}. \tag{2.4}$$

Substituting (2.4) into (2.3), $R_H(t)$ can be reorganized as

$$log_2^{R_H(t)} = \frac{1}{\tau} \cdot t + log_2^{N_0 \cdot v}. \tag{2.5}$$

The cell doubling time, $\tau$, can be obtained by viable cell counting and the doubling time of $R_H$, $\tau_H$, was extracted by linear fitting of $\log_2{}^{R_H(t)}$ versus $t$ as shown in Fig. 2.7(c). Consequently, when $v$ remains constant, $\tau_H$ should be equal to the cell doubling time $\tau$. In other words, the H$^+$ releasing rate per cell can be qualitatively evaluated by comparing $\tau_H$ and $\tau$, depicted in Fig. 2.7(d). Obviously, the extracted $\tau_H$ are generally shorter than the measured $\tau$, indicating that the H$^+$ releasing rate per cell is boosted in higher cell density conditions, which has not been previously documented in literature as we know. Here we propose a plausible explanation. In high cell density condition (stationary phase), both cell growth and death could happen simultaneously, and the dead cell may function as metabolic adjuvants, stimulating cellular metabolism. Thus, raised $v$ with $t$ and cell density was observed. More discussion on kinetics can be found in **Paper I**.
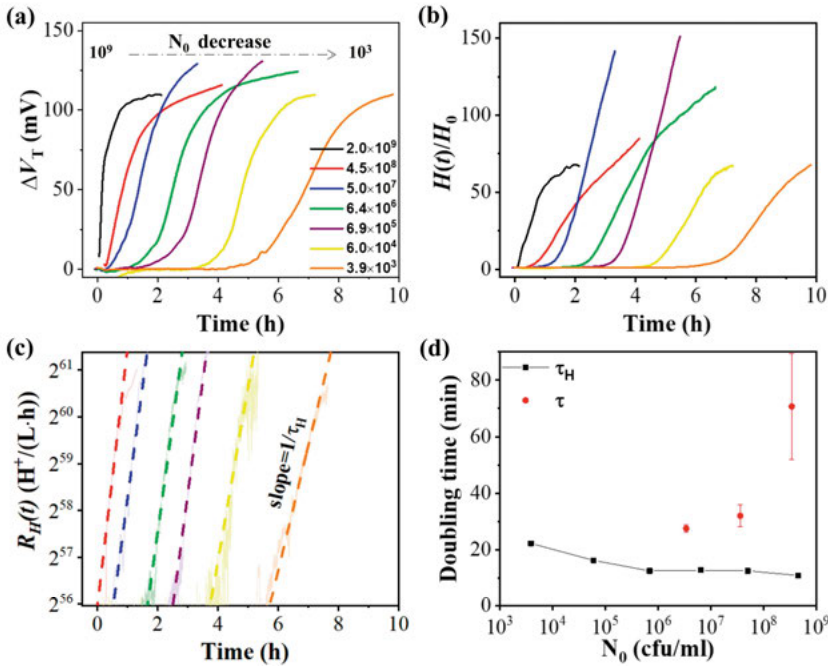


Figure 2.7. (a) $\Delta V_T$ and (b) normalized $H(t)$ vs. time with different initial bacterial concentrations. (c) $R_H(t)$ vs. $t$ plotted in semi-log$_2$ scale, in which dashed lines are linear fitting results and shaded lines are the raw data. (d) doubling time of H$^+$ production ($\tau_H$) and cell density ($\tau$) extracted from model fitting and viable cell counting, respectively.

## 2.4 Metabolic response analysis under ampicillin treatment

### 2.4.1 Metabolic response induced by antibiotics

Over the past few decades, tremendous efforts have been invested into research on antibiotic-killing mechanisms and achieved remarkable success. Nevertheless, those studies have primarily focused on profiling their direct target, such as ampicillin's interaction with penicillin-binding proteins (PBPs), resulting in a somewhat oversimplified view that antibiotic-induced cell death exclusively arises from the inhibition of specific targets [59]. The recently emerged high-throughput technologies enabled the systematic study of bacterial response to antibiotic-induced stress. And it has been confirmed that bacterial metabolism is closely linked to antibiotic lethality via a complex, multifaceted process[60]–[62]. The cell death mediated by antibiotics cannot be totally attributed to the interaction of antibiotics with their direct targets.

The antibiotics can be sorted into bactericidal or bacteriostatic types, defined by their effect on bacteria that results in cell death or stasis respectively. It is accepted that bactericidal antibiotics trigger overflow mechanisms and accumulation of reactive oxygen species (ROS), indicating accelerated respiration [63], [64], whereas bacteriostatic antibiotics can inhibit metabolism and thus effectively keep bacteria in the stationary phase of growth. Conversely, the bacterial metabolic state can also impact antibiotic lethality, as confirmed by combined bacteriostatic and bactericidal treatment [63]. Therefore, understanding the dependency of bacterial metabolism on antibiotics is important for new antibiotics development and improvement of therapeutic methodologies.

Despite the great importance of metabolism response, the underlying mechanism has not been thoroughly understood. In section 2.3, we have demonstrated the capabilities of our SiNWFET sensor, which enables rapid AST within 30 min. Furthermore, the mechanism of different antibiotics can be discerned based on tested profiles. The observed acidification of the medium can be attributed to acetate overflow that occurs once TCA respiration reaches its maximum rate. Consequently, pH shift serves as an indicator of the bacterial respiration state and was used to monitor cellular metabolic response during antibiotic treatment. In this section, we investigated the real-time and early metabolic response to ampicillin treatment on SiNWFET sensors.

## 2.4.2 Measurement procedure optimization

The bacterial metabolism is highly sensitive to culturing environment, including factors such as cell density, temperature, and oxygen concentration. To improve experimental repeatability and precision, we further optimized the testing procedure. During metabolism monitoring, the bacteria were maintained at the stationary phase concentration to rule out the signal contribution of cell division, and the medium was replaced by fresh LB broth right before bacterial injection. The detailed procedure is briefed as the following. After overnight *E. coli* culturing, 200 µL of bacterial suspension was first centrifuged at 4500 rpm. The supernatant was subsequently removed, and the precipitate was resuspended in fresh LB to a volume of $V_1$. During measurement, the resuspended bacteria ($V_2$) were pipette-injected into the container where certain amounts of
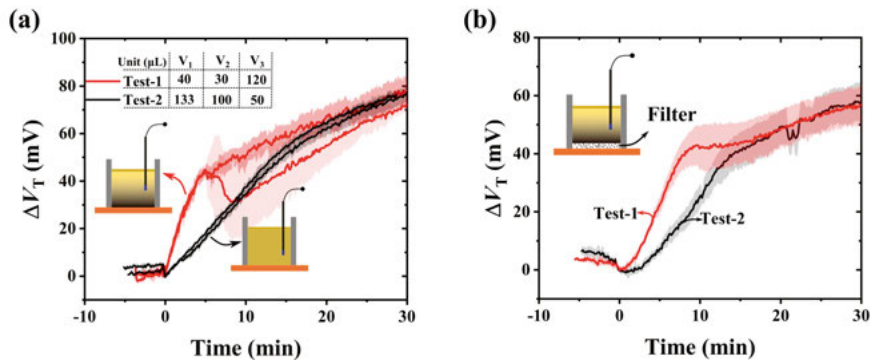


*Figure 2.8. Acidification curves, $\Delta V_T$ vs. time (a) for repeated tests with different dilution processes, (b) with a filter to isolate bacteria from chip surface. The final bacterial amount in the container is the same in all tests with a volume of 150 µL, while the injected bacterial suspension is increasingly diluted from Test-1 to -2.*

background LB ($V_3$) were already placed for baseline settlement. The final bacterial concentration in the container ($V_2+V_3$) was adjusted to saturated value by modulating the dilution ratio in this washing process. Since our stage cannot be shaken during testing, the medium must the effectively mixed during the injection step. Here, different initial conditions with various dilution parameters ($V_1$, $V_2$, and $V_3$) along with their repeated test result are presented in Fig. 2.8(a).

The incubation curves with the same amount of bacteria in the container are obviously dependent on the injected bacterial density as shown in Fig. 2.8(a). For higher injection concentration, such as Test-1, the measured $\Delta V_T$ increases to saturated value more rapidly, which coincides with the previous results in

Fig. 2.5. But the sharp signal drop is often observed in repeated measurements. When the injected bacterial suspension gets diluted with higher $V_1$ in Test-2, the slope of $\Delta V_T$ vs. time decreases but reaches the same level as Test-1 after 20 min with excellent repeatability. The only difference between the two tests was the initial cell density of the injected bacteria. When the high-density bacterial suspension (Test-1) was injected, over-condensed bacteria could settle to the surface of the sensor bottom, where cells could attach to the SiNW channel leading to a locally higher signal response. Additionally, the temperature gradient in the container could also cause the signal dependence on location. To verify these hypotheses, both Test-1 and -2 were repeated with a filter paper of 0.45 um pore size embedded in the container to isolate cells from the channel surface. As shown in Fig. 2.8(b), the acidification rate gap did still exist between the two tests, excluding the contribution from cell attachment. Another possible explanation could be the temperature gradient in the container. Since the heat source is under the metal stage, temperature decreases from the bottom Si chip surface to the top liquid-to-air interface due to the temperature gap between the stage and air. When the injected bacteria are condensed on the bottom interface, the metabolism could be accelerated by local higher temperature. Acidification profile dependence on temperature was characterized as shown in Fig. 2.9 (a). Obviously, the acidification was accelerated at a higher medium temperature. A plausible explanation is that increased kinetic energy of cellular components at higher temperatures could lead to an elevated overall metabolic rate[65], involving the acetate overflow reactions. Despite the observed temperature dependence, rapid acidification as Test-1 did not appear even at 40 °C, implying that heated medium cannot sufficiently boost the acidification process. As possible objective factors were ruled out, the variation of acidification curves in Test-1 most probably originated from the bacteria themselves. In our previous work, it has been observed that the $H^+$ ion production rate per cell increases with cell density, which was ascribed to the metabolic adjuvant role of dead cells (cell growth and death could both take place when the cell density is high). Therefore, the metabolic rate of the locally condensed bacteria in Test-1 could also be accelerated for the same reason, resulting in the measured rapid acidification. To guarantee the experimental repeatability, all the measurements in this work will follow Test-2.
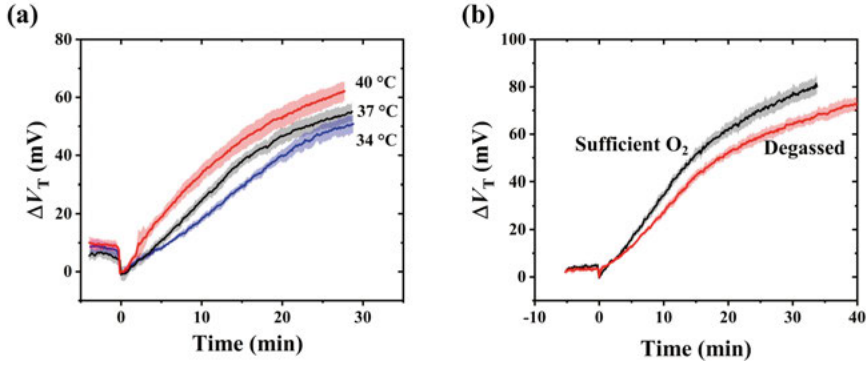
*Figure 2.9. $\Delta V_T$ vs. t at different temperatures (a), and with or without degas process for LB broth.*

In addition to temperature and mixing, the oxygen level is another critical parameter during culturing [66]. In the previous experiments, the fresh LB medium was degassed by boiling for 5 min to avoid air bubble formation which could interrupt current sampling. However, it was accompanied by the elimination of dissolved oxygen and altered cellular metabolism. To relieve this concern, the LB broth was shaken at 37° overnight before usage. As shown in Fig. 2.9(b), the growth is clearly suppressed in a degassed LB medium, where less dissolved oxygen results in lower glucose uptake and even mixed acid fermentation. To make sure that the acidification is dominated by acetate overflow, the degas step was replaced by overnight shaking in all subsequent experiments.

## 2.4.3 Analysis of glucose metabolism using SiNWFETs

Since our measurements were carried out in an LB medium containing tryptones, it is crucial to identify the carbon source that determines acidification mechanisms. The correlation between acidification rate and glucose consumption during testing should also be taken into consideration. Hence, a series of tests was conducted with varying initial glucose concentrations, as presented in Fig. 2.10(a).

In pure LB medium without glucose, $\Delta V_T$ increases slightly in the initial 10 min and then decreases continually. The short increasing stage could be due to the trace amount of sugar in LB, and the continual alkalization origins from released ammonia in the amino acid metabolism process with tryptone as carbon source. When additional glucose was included in LB, a constant acidification rate was observed regardless of initial glucose concentration as shown in

Fig. 2.10(a). Interestingly, even with the lowest concentration of glucose (0.1 g/L), the acidification rate, as indicated by $\Delta V_T$ slope, remains at the same value as high concentration conditions before glucose is fully consumed as seen at 12 min. This phenomenon has been observed in other published studies [67], providing evidence that acetate overflow is independent of glucose levels. In other words, the glucose uptake process is dominated by cellular absorption with the highest priority compared with other carbon sources in LB broth. It further highlights the advantages of glucose as a carbon source in our measurements that the metabolic rate is independent of environmental glucose concentrations and solely relies on the respiration state. When glucose in the medium was completely consumed, $\Delta V_T$ decreased as the released acetate could be reabsorbed as a new carbon source [53]. More discussion can be found in **Paper II.**

Furthermore, the ampicillin-treated tests are presented in Fig. 2.10(b). With 0.1 g/L glucose, the acidification curve turns downward after 15 min when the glucose was fully depleted, consistent with the result from the untreated sample in Fig. 2.10(a). The other samples with higher glucose concentrations show the same deviation time of 20 min, indicating that the ampicillin-treated metabolism cannot be affected by glucose levels, either. The contribution of glucose levels could thus be ruled out when analysing metabolic response under antibiotic treatment. Interestingly, the alkalization caused by AMP has the same deceasing slope as the result of 0.1 g/L glucose, which might imply that the alkalization induced by AMP might also attribute to acetate reabsorption due to the
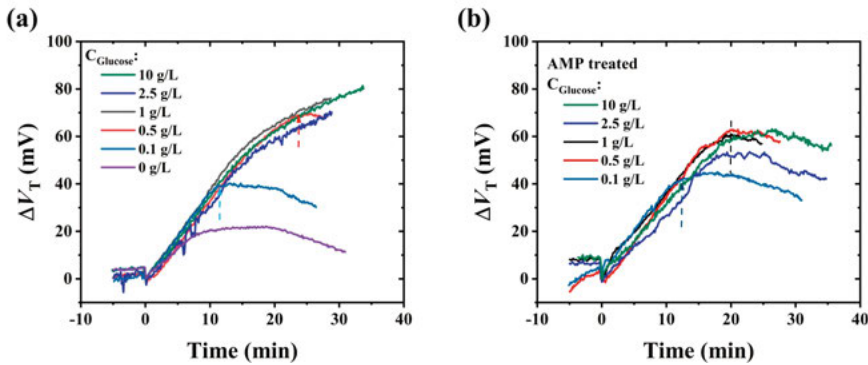


Figure 2.10. $\Delta V_T$ vs. t with different glucose concentrations without (a) and with (b) AMP treatment.

boosted respiration rate which occupies more acetyl-CoA from the acetate over-flow pathway.

To recognize the metabolic response under antibiotic treatment, the reference results without antibiotics, AMP treated, and gentamicin (GEN) treated results are illustrated parallelly in Fig. 2.11. Under AMP treatment, the acidification curve starts to deviate from the reference after 20 min. Relative to untreated control, gentamicin induces an immediate acidification rate response, whereas the response of ampicillin is delayed. Both AMP and GEN belong to bactericidal antibiotics and the respiration rate was accelerated leading to an inhibited acidification rate as expected. These results indicate that different bactericidal antibiotics stimulate varied respiration activities and thus display distinct acidification profiles. The delayed response of AMP and the immediate response of GEN are consistent with published results, in which the oxygen consumption rate (OCR) was monitored as an indicator of respiration rate, and immediately enhanced OCR was observed on GEN-treated sample while the AMP-treated sample responded after 30 min [64]. Based on these fine tests, our SiNWFET sensor is demonstrated to be capable of real-time metabolism monitoring, and label-free and non-destructive measurements can be achieved on our sensors.
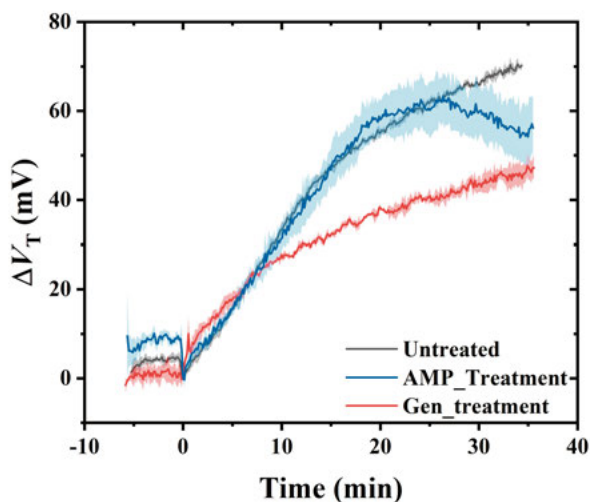


Figure 2.11. $\Delta V_T$ vs. t with different antibiotics treatment including AMP and GEN.
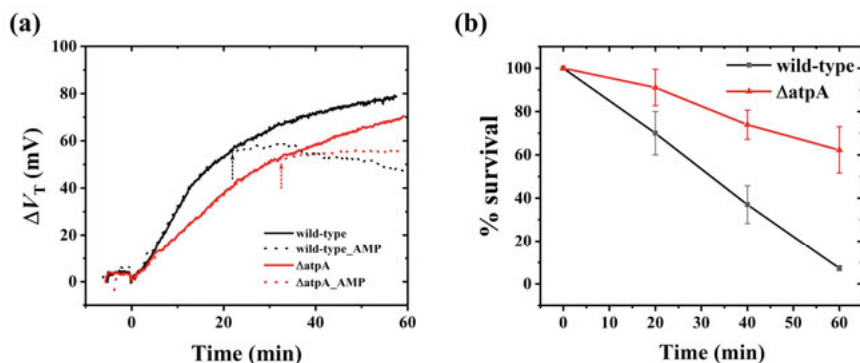
*Figure 2.12. (a) $\Delta V_T$ vs. time curves, and (b) time-killing kinetics for wild-type E. coli and $\Delta atpA$ mutant, with 100 μg/mL AMP and initial cell density of $4 \times 10^9$ cfu/mL.*

To further exploit the mechanism of metabolic response under antibiotic treatment and investigate the link between metabolic state and antibiotic lethality, specific *E. coli* MG1655 mutants were prepared by genetically kicking out genes of targeted enzymes. In this work, three mutants coded as $\Delta atpA$, $\Delta adhE$, and $\Delta nuoG$ were tested under 100 μg/mL AMP treatment in LB with 1% glucose. The results of $\Delta atpA$ are illustrated in Fig. 2.12. Both strains exhibited antibiotic susceptibility, while acidification rate was suppressed, and the AMP effect was clearly delayed in the $\Delta atpA$ mutant. The observed AMP lethality from the measured acidification curves coincided well with time-killing assay results as shown in Fig. 2.12(b), which count for the survival rate in samples measured parallelly with electrical tests. Interestingly, 60% $\Delta atpA$ bacteria survived after 1 h AMP treatment, significantly higher than that of wild-type with ~8% survival rate.

The distinct acidification profile of the $\Delta atpA$ mutant indicates a suppressed cellular metabolism, comparing to the wild-type. It is well known that ATP is required to convert glucose to glyceraldehyde-3-P in glycolysis steps 1-3. In the absence of *atpA*, the ATP/ADP ratio in the $\Delta atpA$ mutant is much lower than the wild-type after overnight culturing in LB. The shortage of ATP in the $\Delta atpA$ therefore suppressed cellular metabolism in the early period of the profiling. However, with the proceeding of cellular metabolism, more ATP could be produced and gradually accumulated, which could further facilitate the glycolysis process and acetate release. This hypothesis is consistent with the observed acidification curve as shown in Fig. 2.12(a) orange line, in which the
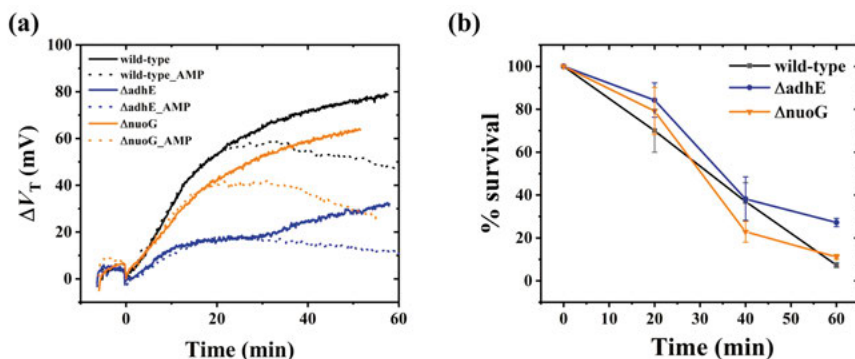
*Figure 2.13. (a) $\Delta V_T$ vs. time curves, and (b) time-killing kinetics for wild-type E. coli, $\Delta adhE$, and $\Delta nuoG$ mutants, with 100 µg/mL AMP and initial cell density of $4 \times 10^9$ cfu/mL.*

slope of $\Delta atpA$ strain in the early 30 minutes is lower than wild-type but approaching subsequently. The suppressed cellular metabolism in the early period indeed leads to attenuation of AMP lethality, as evidenced by both the acidification curves and the time-killing assay results.

In addition to $\Delta atpA$, $\Delta adhE$, and $\Delta nuoG$ were also studied as shown in Fig. 2.13. *adhE* gene encodes the protein that catalyzes the reduction of acetyl-CoA to ethanol, which is highly sensitive to oxygen levels in the medium. However, the regulation of *adhE* in aerobic conditions has not been fully clarified. The acetate excretion is apparently inhibited in $\Delta adhE$ strain in aerobic conditions, indicating suppressed metabolism which subsequently hinders the AMP lethality (see Fig. 2.13(a) blue line). In $\Delta nuoG$ mutant, the NADH-quinone oxidoreductase enzyme in the respiration electron transport chain is defunctionalized, which could result in the accumulation of NADH in the cell and inhibit metabolism. It is out of our expectation that the survival rate of $\Delta nuoG$ mutant is very close to the wild-type strain (Fig. 2.13(b)), which implies that the extra NADH might be depleted in other processes such as lactate fermentation to release the stress. Further investigations on the respiration state in $\Delta nuoG$ will be carried out soon, based on the oxygen consumption rate measured on the Seahorse XF analyzer.

In this section, the early metabolic response of *E. coli* to ampicillin treatment was systematically investigated using SiNWFET sensors. The dependences of extracellular pH, as a proxy of glucose metabolism activity, on environmental factors, such as cell distribution, temperature, carbon source, and oxygen level, were carefully evaluated first. Our sensors detected early metabolic response

indicated by medium alkalization before cell lysis, for the bacteria sample exposed to near-MIC AMP. The detected early response was attributed to acetate uptake due to the accelerated TCA cycle induced by AMP. The sensors also revealed attenuated antibiotic lethality to gene-engineered mutant with suppressed metabolism. These studies further highlight our SiNWFET sensor as a promising all-electrical and robust platform for investigating the interplay between the bacterial metabolism and antibiotic efficacy.

# 3. Upgrade from SiNWFET to SJGFET

SiNWFET with $HfO_2$ dielectric gate oxide has been demonstrated as a powerful tool for biosensing by $p$H monitoring in Chapter 2. Its capability of chemicals and biomolecular detection in electrolytes was also widely proven in many studies. As a sensor, the limit of detection (LOD) is one of the most critical parameters for extremely low concentration detection, and it's ultimately determined by the sensitivity and noise floor of the whole system. In the case of our SiNWFET, the $p$H signal response was optimized to 58 mV/dec, close to the Nernstian limit. To further improve LOD or even achieve single molecular detection, the noise of the system must be reduced.

In our measurement system, the overall noise consists of external noise, such as environmental noise and read-out instrument noise, and internal noise, including electrolyte/oxide sensing interface noise, thermal motion of ions, RE electrochemical processes, and intrinsic device noise, in which the intrinsic device noise has for long been considered as the dominant component [68], [69]. In MOS-type devices, the random carriers trapping/detrapping in the vicinity of gate oxide/Si channel interface is attributed to be the main noise source at low frequency [70], showing $1/f$ like power spectrum density (PSD). To eliminate the noisy oxide/Si interface, Schottky junction gated SiNWFET (SJGFET) was proposed [69], [71], [72], emulating junction gated FET (JFET) The measured $1/f$ noise on SJGFETs fabricated on SIMOX (separated by implantation of oxygen) SOI substrate was greatly reduced compared to the MOSFET reference device, validating the superiority of the Schottky junction gate. However, the observed noise dependence on substrate bias ($V_{sub}$) indicates that the bottom interface between the Si channel and BOX becomes the dominant noise source as noise from the top oxide/Si interface is substantially eliminated.

To explore the true potential of the Schottky junction gate, we designed and fabricated SJGFETs on bonded SOI wafers from SOITEC with well-known improved BOX/Si interface quality[73]. In this Chapter, the device fabrication, electrical characterization, and noise analysis are systematically discussed.

# 3.1 Schottky junction tri-gate SiNWFET

The 3-dimensional (3D) schematic with its cross-section views of the channel is shown in Fig. 3.1(a). The BOX and top silicon thickness after PtSi formation are 145 and 35 nm respectively. To study the impact of channel dimension on device performance, the channel width is ranged from 90 to 500 nm with a fixed gate length of 900 nm. Both the top and two sidewall surfaces of the SiNW channel are wrapped with PtSi junction to eliminate the gate oxide/Si interface, called tri-gate structure. Source/drain terminals are heavily $n$-doped while the SiNW channel is moderately doped to $N_D$, $6\times10^{17}$ cm$^{-3}$, via arsenic (As) im-
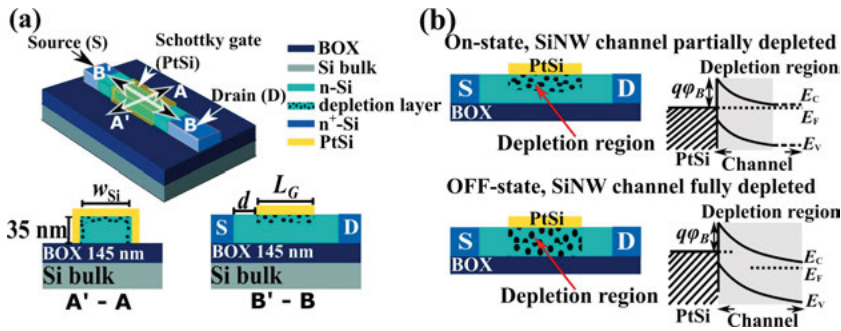


*Figure 3.1. (a) 3-D sketch and cross-sections of a SJGFET with the depletion layer marked as the cyan dotted region. (b) the working principle of a SJGFET illustrated with cross-sections and band diagrams.*

plantation. The working principle of SJGFET with cross-section sketches and energy band diagrams are displayed in Fig. 3.1(b). When the PtSi gate is positively biased, the channel is partially depleted and the SJGFET is at on-state. With the gate voltage ($V_G$) turned to negative, the depletion region expands, and pinches off the whole channel, resulting in off-state. By further reducing $V_G$, the carrier density and $I_{DS}$ decrease exponentially, defined as the subthreshold region which is commonly chosen as the working region in SiNWFETs sensors owing to its linear relationship between the logarithm of $I_{DS}$ and $V_G$. In this thesis, most noise characterizations are carried out in the subthreshold region.

## 3.2 Fabrication of SJGFETs

The SJGFETs were fabricated on bonded SOI substrates using standard Si technology. The key process steps were sketched in Fig. 3.2. Starting from 100 mm SOI wafer with 45-nm-thick top silicon layer, the channel doping level was defined by universally moderate As implantation. Then S/D was heavily im-
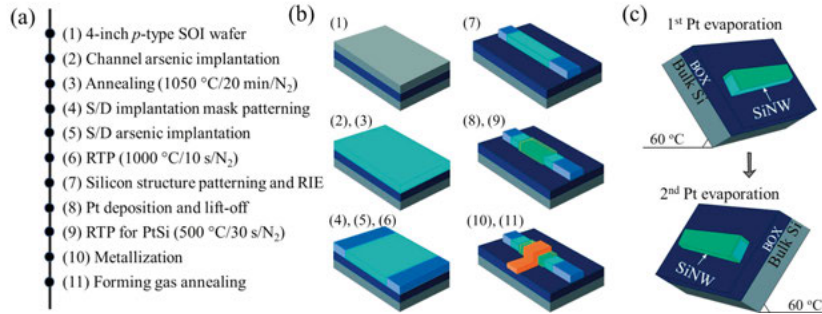


*Figure 3.2. Schematics of (a), (b) key fabrication steps for SJGFET, (c) two-step Pt evaporation with substrate tilting to ensure conformal Pt coverage of the SiNW channel.*

planted with channel region masked by patterned photoresist. Device structure was defined by electron beam lithography (EBL) and reactive ion etching (RIE). The PtSi junction gate was formed by electron beam evaporation with lift-off process, followed by rapid thermal processing (RTP) at 500 °C for 30 s in $N_2$. To ensure a conformal Pt coverage on the sidewalls of the SiNW, the SOI wafer was tilted first clockwise and then anticlockwise for 60º during Pt evaporation. The device was metalized on the gate and source/drain contacts by 100 nm Al with a 10-nm Ti as the adhesion layer. Finally, the device fabrication was completed with forming gas annealing (FGA) at 400 ºC for 30 min.

## 3.3 DC and LFN characterization of SJGFET

The transfer curves, $I_D$ vs. $V_G$ of SJGFETs with different channel width were characterized as shown in Fig. 3.3 (a). The on-to-off current ratio reaches 5 orders of magnitude within 0.3 V $V_G$ on 500-nm-wide SJGFET (named as SJG500). The best achieved subthreshold swings (*SS*) is 66 mV/dec, close to an ideal value of 63 mV/dec, calculated with [74]

$$SS = 2.3 \frac{kT}{q} \left(1 + \frac{C_{BOX}}{C_{Si}+C_{it}}\right), \tag{3.1}$$

where $C_{BOX}$, $C_{Si}$, and $C_{it}$ are the capacitance of BOX, Si channel and interface traps at Si/BOX interface, respectively.

The threshold voltage ($V_{th}$) of SJGFETs were designed lower than 0.2 V to avoid excessive gate leakage ($I_G$) in forward-biased condition. In a wide channel, $i.e.$, 500 nm, the depletion from the sidewall gate is negligible, thus, $V_{th}$ can be calculated assuming a flat-band condition at Si/BOX interface as[69]

$$V_{th} = V_{bi} - qN_D t_{Si}^2/2\varepsilon_{Si} \tag{3.2}$$

in which $V_{bi}$ is the build-in potential of PtSi/Si junction, $t_{Si}$ the height of the channel, and $\varepsilon_{Si}$ the dielectric constant of silicon. In a shrunken channel, the depletion from the sidewall gate is evidently embodied as a positive $I$-$V$ shift in Fig. 3.3(a). Similar $V_{th}$ shifting is also observed in Fig. 3.3(b) by applying substrate bias ($V_{th}$), which curves the energy band at Si/BOX interface, requiring extra $V_G$ for compensation. Detailed data analysis can be found in **Paper III**.
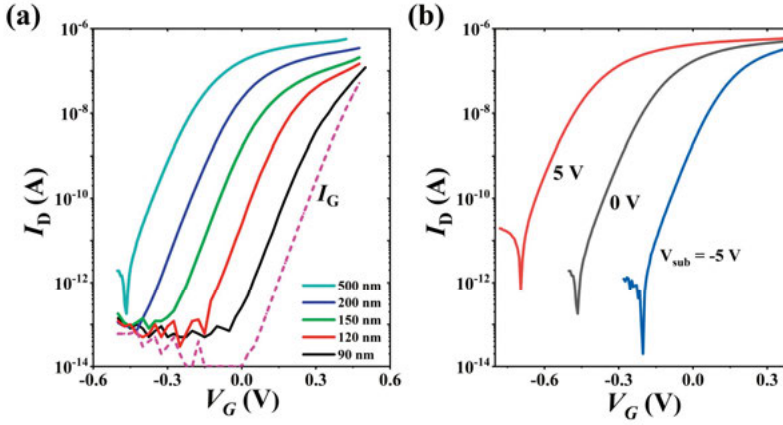


*Figure 3.3. Transfer curves for SJGFETs with different channel widths (a), measured at $V_{sub} = 0$ V, and (b) for SJG500 measured at different $V_{sub}$, under $V_{DS} = 0.1$ V.*

Low-frequency noise (LFN) of SJGFETs was characterized using a Keysight E4727A advanced noise analyzer. During LFN measurements, $V_{DS}$ was constantly biased at 0.1 V, while the $V_G$ was determined by noise analyzer depending on $I_D$ set value and measured transfer curve of the SJGFET.

The $I_D$ PSD, $S_{id}$, and gate-referred voltage noise, $S_{vg}$, were systematically characterized on different devices under various working conditions. As shown in Fig. 3.4, the area normalized $S_{id}$, $A \times S_{id}$, is plotted versus $f$, which exhibits typical $1/f$ noise spectrum in low frequency region. At higher $I_D$, the measured $A \times S_{id}$, increases due to more carrier number fluctuation from the trapping/detrapping process and more intensive mobility fluctuation from enhanced scattering under a high density of carriers.

Table 3.1. Comparison of $A \times S_{vg}$ for different FETs. All data are values representing the best noise performance and some data have been converted from the original work for comparison purpose.

| $A \times S_{vg}$ $\left(\mu m^2 V^2/Hz\right)$ | SOITEC-SJGFET | SIMOX-SJGFET [69] | Ref [68] | Ref [76] | Ref [77] |
|---|---|---|---|---|---|
| 1 Hz | $1.2 \times 10^{-10}$ | $2.1 \times 10^{-9}$ | $1.1 \times 10^{-9}$ | | $5 \times 10^{-10}$ |
| 10 Hz | $1.1 \times 10^{-11}$ | $1.3 \times 10^{-10}$ | | $8 \times 10^{-11}$ | |

$S_{vg}$ is a fictitious quantity derived for comparison between different devices, which is correlated with $S_{id}$ by transconductance, $g_m$, expressed as [75]
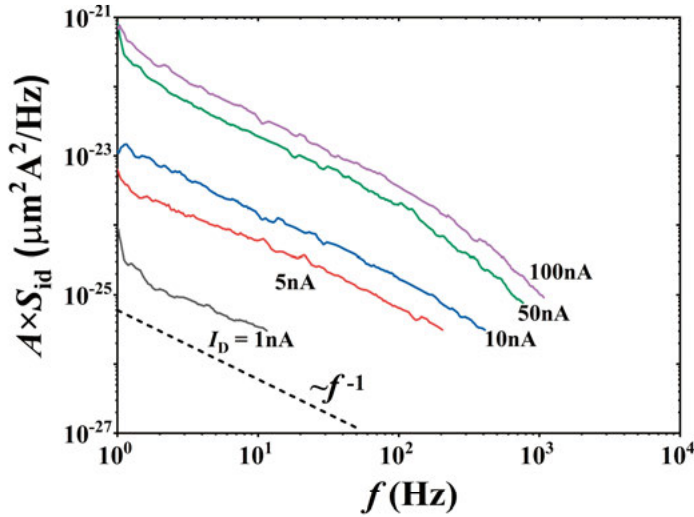
$$S_{vg} = \frac{S_{id}}{g_m^2}.$$

(3.3)



Figure 3.4. Area normalized $S_{id}$ spectrum measured under different $I_D$.

Since $S_{vg}$ is inversely proportional to gate area, the measured $S_{vg}$ were normalized by area, $A \times S_{vg}$, for comparison. The $A \times S_{vg}$, of SJG500 under 10 A $I_D$ are $1.2 \times 10^{-10}$ and $1.1 \times 10^{-11} \mu m^2 V^2/Hz$ at 1 Hz and 10 Hz, respectively. To benchmark the LFN of SJGFETs, collected $A \times S_{vg}$ from published literatures are listed in Table 3.1 for comparison. $A \times S_{vg}$ of SJG500 is considerably lower than state-of-the-art SiNWFET-based sensors [68], [76], [77] and one order of magnitude lower than SJGFETs on SIMOX-SOI substrate[69], which clearly evidences the advantages of Schottky junction gate for noise reduction, and confirms higher Si/BOX interface quality of SOI substrate from SOITEC than that of SIMOX.

LFN dependence on channel dimension and $V_{sub}$ was observed as shown in Fig. 3.5. In SJG500, $A \times S_{vg}$ can be further reduced by applying positive $V_{sub}$, while it is increased under negative $V_{sub}$. A similar tendency also arises on devices with different channel widths (see also Fig. 3.5). A narrower channel width will result in enhanced depletion from the sidewall gate, which could push the current path away from the bottom channel/BOX interface, similar to the effect under negative $V_{sub}$. More detailed discussion can be found in **Paper**
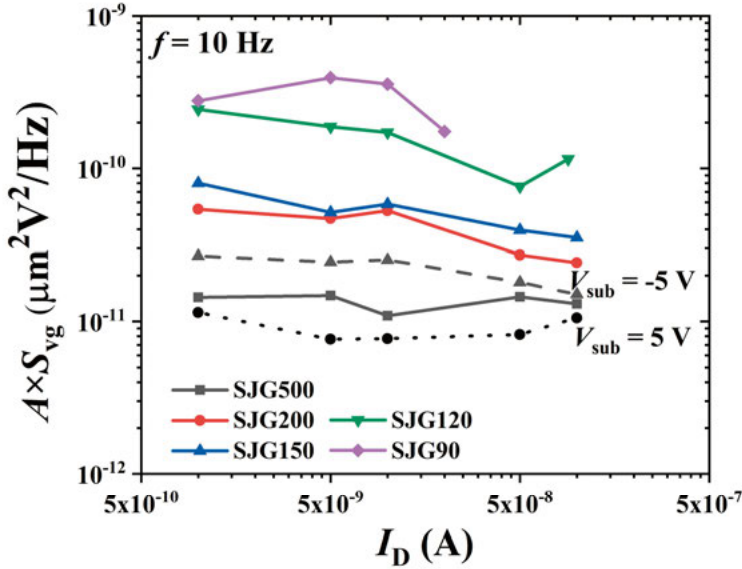


*Figure 3.5. $A \times S_{vg}$ (10 Hz) versus $I_D$ for different SJGFETs at $V_{sub}$ = 0 V. $A \times S_{vg}$ of SJG500 under different $V_{sub}$ is also plotted (black lines).*

**III**. This noise dependence, however, is opposite to previously observed results on SIMOX-SJGFETs, in which $A \times S_{vg}$ can be lowered by up to 3 orders of magnitude under negative $V_{sub}$, attributing to dramatically reduced Coulomb scattering at channel/BOX interface [72]. Obviously, the channel/BOX interface is still a major noise source for SOITEC-SJGFETs, but its noise mechanism is clearly different from SIMOX-SJGFETs. To further improve the device performance, noise mechanism has to be well understood.

## 3.4 1/$f$ noise modeling

1/$f$ noise, also called flicker noise, refers to the spectrum density, $S(f)$, of a stochastic process with a form as [78]

$$S(f) = constant/f^\alpha, \tag{3.4}$$

where $f$ is the frequency with exponent α in the range 0.7-1.3. 1/$f$ noise was first found by Johnson (1925), then wildly observed in various phenomenon. In MOSFETs, the 1/$f$ noise can mainly be interpreted by two mechanisms, i.e., the carrier number fluctuation (CNF) model [79] and the Hooge mobility fluctuation (HMF) model[80]. In the CNF model, the 1/$f$ noise is explained by random trapping/detrapping of carriers to the traps in the vicinity of Si/SiO$_2$ interface. Taking the correlated mobility fluctuation (CMF) into account, the CNF model is extended to include the CMF, describing $S_{id}$ as [75], [81]

$$S_{id}(f) = S_{vfb} g_m^2 \left(1 + \Omega \frac{I_D}{g_m}\right)^2, \tag{3.5}$$

in which $S_{vfb}$ is the flat-band voltage PSD and $\Omega$ is the CMF noise term. The HMF model follows an empirical formula as

$$\frac{S_{id}}{I_D^2} = \frac{q\alpha_H}{f N_{total}}, \tag{3.6}$$

where $N_{total}$ is the total carrier number and $\alpha_H$ is the Hooge parameter[80]. By plotting $S_{id}/I_D^2$ vs. $I_D$ with fitting curves using Eq. (3.5), the noise origin is identified as the CNF+CMF mechanism, while the HMF cannot match the LFN data as $S_{id}/I_D^2$ clearly deviates from reciprocal of $I_D$ (see Fig. 3.6).

Since the carriers random trapping/detrapping process is attributed to the dominant noise source in SJGFETs, the noise spectrum can be derived based on CNF+CMF, ignoring the noise contribution from Schottky junction gate. To simplify the modeling, the SiNW channel is idealized as planar structure as

shown in Fig. 3.7(a), and the charges and traps distributed are illustrated in Fig, 3.7(b). The $S_{id}$ can be represented by [82], [83]
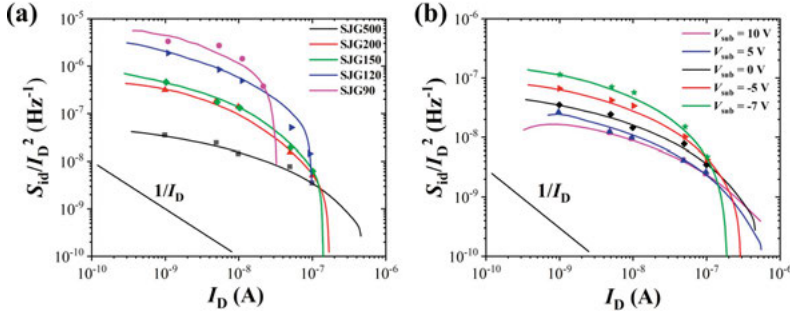


Figure 3.6. $S_{id}/I_D^2$ versus $I_D$ for (a) SJGFETs with different channel widths at $V_{sub} = 0$ V, and (b) SJG500 at different $V_{sub}$. Solid lines represent model fitting results in both figures.

$$S_{id}(f) = \frac{kT I_D^2}{\gamma f w L^2} \int_0^L N_t(E_{fn}) \left[ \frac{R(x)}{n(x)} \pm \alpha_{sc}\mu_{eff} \right]^2 dx, \qquad (3.7)$$

where $kT$ is the thermal voltage, $\gamma$ the attenuation coefficient of the electron wave function in oxide ($\sim 10^8$ cm$^{-1}$ for Si-SiO$_2$ system), $L$ the channel length, $N_t(E_{fn})$ the trap density $N_t$ at quasi-Fermi level $E_{fn}$, $n(x)$ the carrier density at position $x$. $R(x)$ is the ratio of fluctuation in carrier number to fluctuation in occupied trap number, i.e., $R = \delta\Delta N/\delta\Delta N_t$, where $\Delta N$ and $\Delta N_t$ are carrier and trap numbers in a differential element at position $x$, with area of $w\Delta x$ as illustrated in Fig. 3.7(a). To simplify the model, $N_t(E_{fn})$ are assumed to be uniform along the $x$-axis in the SiNW channel channel at low $V_D = 0.1$ V (see coordinate system in Fig. 3.7(a)).
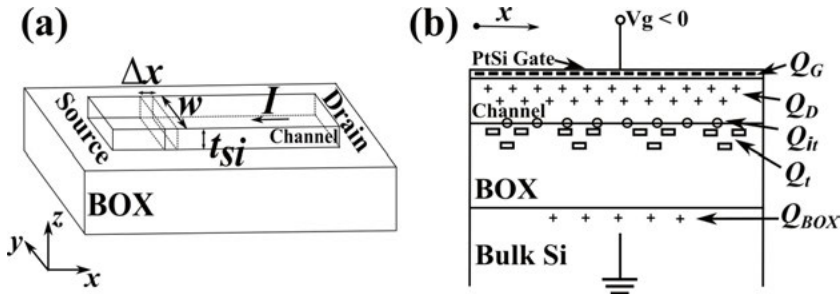


Figure 3.7. (a) 3-D and (b) cross-section schematics of the SiNW channel with charges and traps illustrated.

To simplify the integration in Eq. (3.7), $R(x)/n(x)$ must be extracted. Here, we assume that the trapping/detrapping of carriers at BOX/SiNW interface leads to fluctuations in surface potential ($\delta\Psi_s$) and number of occupied traps ($\delta\Delta N_t(x)$). The surface potential fluctuation will trigger the re-distribution of charges in whole system via capacitance coupling, including number of carriers ($\delta\Delta N(x) = w\Delta x C_{ch}(x)\cdot\delta\Psi_s$) in channel, interface traps ($\delta Q_{it} = w\Delta x\, C_{it}\cdot\delta\Psi_s$), charges on gate ($\delta Q_G = w\Delta x\, C_{Si}\cdot\delta\Psi_s$), and bottom side of BOX ($\delta Q_{BOX} = w\Delta x\, C_{BOX}\cdot\delta\Psi_s$). $C_{ch}(x)$, $C_{BOX}$, $C_{Si}$, and $C_{it}$ are area normalized channel carrier differential capacitance, BOX capacitance, SiNW channel geometric capacitance, and interface trap capacitance, respectively. To maintain the charge neutrality, the total charge fluctuation must equal to zero, resulting in $q\delta\Delta N_t(x) = q\delta\Delta N(x)+\delta Q_G+\delta Q_{it}+\delta Q_{BOX}$ [84]. Then $R$ can be derived

$$R = \frac{-C_{ch}(x)}{C_{BOX}+C_{Si}+C_{ch}(x)+C_{it}}. \tag{3.8}$$

In $R(x)/n(x)$ term, the mobility fluctuation is ignored, which is reflected in the later $\alpha_{sc}\mu_{eff}$ term. Since $I_D$ is proportional to $n(x)$, we get

$$\frac{dI_D(x)}{I_D(x)} = \frac{dn(x)}{n(x)}. \tag{3.9}$$

Then, $n(x)$ can be mathematically represented by $I_D(x)$ and transconductance $g_m(x)$ according to (3.9)

$$n(\mathrm{x}) = I_D(x)\cdot\frac{dn(x)}{dI_D\,(x)} = I_D(x)\cdot\frac{dV_G(x)}{dI_D\,(x)}\cdot\frac{dn(x)}{dV_G(x)}$$

$$= \frac{I_D(x)}{g_m(x)}\frac{C_{ch}(x)\cdot C_{Si}}{q\cdot(C_{Si}+C_{BOX}+C_{ch}(x)+C_{it})}. \tag{3.10}$$

Substituting (3.8) and (3.10) into (3.7), the integration in (3.7) yields

$$S_{id}(f) = \frac{q^2 kT g_m^2 N_t(E_{fn})}{\gamma f w L C_{Si}^2}\left(1+\Omega\frac{I_D}{g_m}\right)^2 \tag{3.11}$$

where $\Omega = \alpha_{sc}\mu_{eff}\cdot C_{Si}$ represents the total corelated carrier mobility fluctuation dominated by Coulomb scattering. With reference to the general expression for $S_{id}$, (3.5), according to the CNF+CMF model, $S_{vfb}$ of the SJGFETs on a SOI substrate can be derived,

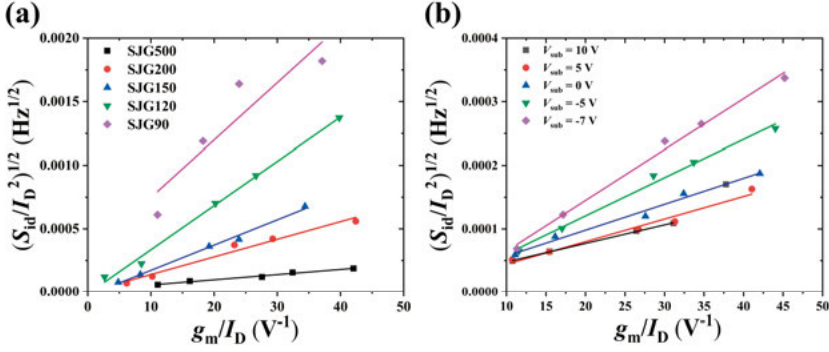$$S_{vfb} = \frac{q^2 kT N_t(E_{fn})}{\gamma f w L C_{Si}^2}. \tag{3.12}$$

*Figure 3.8. $(S_{id}/I_D^2)^{1/2}$ versus $g_m/I_D$ (10 Hz) for (a) SOITEC-SJGFETs with different w at $V_{sub}$ = 0 V and (b) SJG500 at different $V_{sub}$ values. Linear fitting results are plotted as solid lines in both figures.*

$N_t$ of the BOX/SiNW channel interface can be calculated from $S_{vfb}$ in (3.12), which can be extracted from the slope of $(S_{id}/I_D^2)^{1/2}$ versus $g_m/I_D$ curves according to re-arranged (1) as

$$\left(\frac{S_{id}}{I_D^2}\right)^{1/2} = S_{vfb}^{1/2}\left(\frac{g_m}{I_D} + \Omega\right). \qquad (3.13)$$

As seen in Fig. 3.8(a), $(S_{id}/I_D^2)^{1/2}$ shows good linear relationship with $g_m/I_D$ for different SOITEC-SJGFETs at $V_{sub}$ = 0 V. The extracted $S_{vfb}$ at 10 Hz are summarized in Table 3.2. More information is available in **Paper IV**.

In the model derivation, the SiNW is treated as an ideal planar structure and the modulation from sidewall gate is ignored. In reality, the carriers located at the corner of channel are depleted more by sidewall gate, resulting in narrower effective channel width ($w_{eff}$), and traps close to gate could be screened. The sidewall gate effect in narrow device must be quantified to extract accurate $N_t$. As shown in Fig. 3.9(a), the BOX/SiNW channel interface is divided into small segments with 2 nm in width. Area normalized geometric capacitance between each segment and the Schottky junction tri-gate, $C'_{Si}$, as well as the noise contribution from the traps in each segment, $S'_{vfb}$, are individually calculated, plotted in Fig. 3.9(b). The total $S_{vfb}$ can be calculated by the sum of $S'_{vfb}$ from all segments (see **Paper IV** for detailed calculation).

$N_t$ for SOITEC-SJGFETs extracted with $w_{eff}$ using (3.12) are also summarized in Table 3.2. $N_t$ in SJG500 ranges from $7.9 \times 10^{15}$ to $4.0 \times 10^{16}$ cm$^{-3}$eV$^{-1}$, which is about 3 orders of magnitudes lower than the $N_t$ values in SIMOX-

Table 3.2 Extracted $S_{vfb}$ and $N_t(E_{fn})$ for SJG500 under different $V_{sub}$ and SJGFETs with different widths under $V_{sub} = 0$ V

| $V_{sub}$ (V) | 10 | 5 | 0 | -5 | -7 |
|---|---|---|---|---|---|
| $S_{vfb}$ (V$^2$/Hz) | $1.6\times10^{-11}$ | $1.3\times10^{-11}$ | $1.7\times10^{-11}$ | $3.3\times10^{-11}$ | $6.4\times10^{-11}$ |
| $N_t(E_{fn})$ of SJG500 (cm$^{-3}$eV$^{-1}$) | $1.0\times10^{16}$ | $7.9\times10^{15}$ | $1.0\times10^{16}$ | $2.1\times10^{16}$ | $4.0\times10^{16}$ |
| $w$ (nm) | 500 | 200 | 150 | 120 | 90 |
| $S_{vfb}$ (V$^2$/Hz) | $1.7\times10^{-11}$ | $1.9\times10^{-10}$ | $4.0\times10^{-10}$ | $1.2\times10^{-9}$ | $2.0\times10^{-9}$ |
| $N_t(E_{fn})$ (cm$^{-3}$eV$^{-1}$) | $1.0\times10^{16}$ | $2.8\times10^{16}$ | $4.8\times10^{16}$ | $8.1\times10^{16}$ | $6.7\times10^{16}$ |

SJGFETs. The increase of $N_t$ with a negative $V_{sub}$ indicates a nonuniform energy distribution of interface traps, *i.e.*, higher $N_t$ when the BOX/SiNW channel interface is under depletion. It is also observed that SOITEC-SJGFET with a
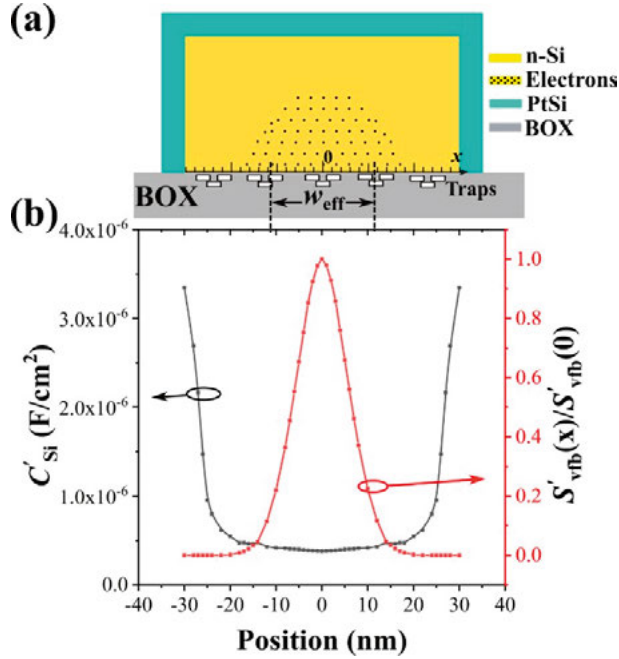


Figure 3.9. (a) Sketch of the SiNW channel cross-section showing electron distribution in the channel, (b) calculated $C'_{Si}$ and normalized $S'_{vfb}$, $S'_{vfb}(x)/S'_{vfb}(0)$, for the segments in different positions.

smaller $w$ has a higher $N_t$, despite the same $V_{sub} = 0$ V. This is expected as the
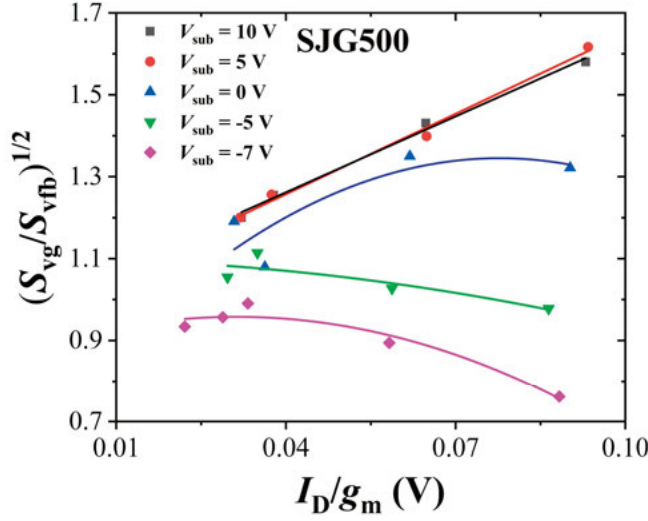
*Figure 3.10. $(S_{vg}/S_{vfb})^{1/2}$ versus $I_D/g_m$ measured at 10 Hz for SJG500 at different $V_{sub}$.*

two sidewall junction gates can also deplete the BOX/SiNW channel interface in the narrow channel, exhibiting a similar effect as applying a negative $V_{sub}$.

Based on (3.11), the correlated mobility fluctuation can be quantified with reorganized formation as [75]

$$\left(\frac{S_{vg}}{S_{vfb}}\right)^{1/2} = 1 + \Omega \cdot \frac{I_D}{g_m}. \tag{3.14}$$

The CMF term, $\Omega$, extracted from the slope of the $(S_{vg}/S_{vfb})^{1/2}$ versus $I_D/g_m$ curve, generally describes the dependence of $\mu_{eff}$ on surface potential $\Psi_s$ at the BOX/SiNW channel interface [86],

$$\Omega = \frac{1}{\mu_{eff}} \frac{\delta \mu_{eff}}{\delta \Psi_s}. \tag{11}$$

$\mu_{eff}$ is dependent on both Coulomb scattering limited mobility ($\mu_c$) and surface roughness scattering limited mobility ($\mu_{sr}$) and can be calculated according to Matthiessen's rule as $\mu_{eff}^{-1} = \mu_c^{-1} + \mu_{sr}^{-1}$ [74], [86]. $\mu_c$ and $\mu_{sr}$ fluctuations will both contribute to $\Omega$.

In Fig. 3.10, $(S_{vg}/S_{vfb})^{1/2}$ versus $I_D/g_m$ curves for SJG500 at different $V_{sub}$ is presented. The close proximity of $S_{vg}/S_{vfb}$ to 1 suggests that the contribution of CMF near the BOX/SiNW channel is insignificant in SOITEC-SJGFETs. Notably, when the BOX/SiNW channel is under accumulation ($V_{sub}$ = 5 V and 10 V), the curves exhibit excellent linearity with a constant and positive slope. Because now current path is near the interface and closest to the traps, with $\Omega$

55

primarily attributed to Coulomb scattering [87], i.e., $\delta\mu_{\text{eff}}/\delta\Psi_s \sim \delta\mu_c/\delta\Psi_s > 0$. The extracted $\alpha_{sc}$ is $4.2 \times 10^4$ V·s/C. In stark contrast, the extracted $\alpha_{sc}$ value in SIMOX-SJGFETs is approximately 50 times larger [72], indicating a much more dominating CMF contribution to the overall LFN in the SIMOX-SJGFETs which have considerably higher $N_t$ and roughness at the BOX/SiNW channel interface.

When the BOX/SiNW channel interface of our SJG500 is biased to depletion with $V_{\text{sub}}$ stepped from 0 to -7 V, $\Omega$ gradually shifts to negative values, as shown in Fig. 3.10. Such shift could be attributed to a transition into surface roughness scattering dominant region where $\delta\mu_{\text{eff}}/\delta\Psi_s \sim \delta\mu_{sr}/\delta\Psi_s < 0$ [86]. To elucidate this phenomenon, a possible explanation is provided as follows. The negative $V_{\text{sub}}$ effectively displaces the current path away from the BOX/SiNW channel interface and deep into the channel bulk. Consequently, Coulomb scattering is significantly reduced owing to the increased distance between the electron centroid and interface traps. On the other hand, the PtSi/silicon interface is rough due to the relatively large PtSi grain size. The rough junction interface could lead to enhanced surface roughness scattering especially when the current path is brought closer to the trigate junction by the negative $V_{\text{sub}}$. The combination of the two effects therefore accounts for the observed transition of the scattering mechanisms.

# 4. A Piezoresistive Nanomechanical Sensor Based on Suspended SiNW-Net for Bacterial Motility Test

In Chapter 2, we have demonstrated rapid ASTs achieved via monitoring extracellular $p$H with SiNWFET sensors. Besides extracellular $p$H, motility is another phenotypic indicator for bacterial activity. As we know, bacteria can move actively in liquid medium with the thrust generated by their powerful flagellar motors. These flagellar motors act like screw propellers powered by inward-directed electrochemical gradient of protons or sodium ions across the cytoplasmic membrane. The rotational speed of flagellar can reach up to 300 revolutions per second in *E. coli* and *Salmonella*, which is closely correlated with the metabolic activity of these bacteria. Recently, rapid ASTs based on bacterial motility detection were demonstrated by using AFM. In this Chapter, we proposed a novel piezoresistive nanomechanical sensor based on suspended SiNW-net to detect bacterial motility for rapid ASTs. This sensor does not involve any sophisticated optical system, thus with the potential to avoid the requirements of highly specialized laboratory or operator. The device design, fabrication, optimization, and characterization will be thoroughly introduced in this chapter.

## 4.1 Piezoresistive effect in SiNW

The property of a crystalline material is determined by both the constituent elements and the lattice structure. An applied external force can change the microscopic lattice parameters and lead to macroscopic deformation in a crystalline material. Consequently, certain physical property also changes under macroscopic deformation, which is called the piezo effect. In crystalline silicon, the deformation of the lattice structure leads to alterations in the energy band, resulting in variation in both the density and effective mass of carriers [52]. This

is electrically manifested as the piezoresistive effect. As discussed in Chapter 1 (1.5), the piezoresistive gauge factor of silicon is dominated by relative resistivity variation instead of dimensional deformation. To estimate the piezoresistive output, both the gauge factor and mechanical properties of silicon should be considered.

The elasticity correlating stress ($\sigma$) to strain ($\varepsilon$) can be described by Hooke's law with compliance $S$ or stiffness $C$ as [88]

$$\sigma = C\varepsilon, and \ \varepsilon = S\sigma. \tag{4.1}$$

Both stress and strain are second-rank tensors containing shear and normal components as illustrated in Fig. 4.1 (a). To satisfy moment equilibrium, the symmetric off-diagonal terms, $\sigma_{zx}$, $\sigma_{zy}$, and $\sigma_{xy}$ equal to $\sigma_{xz}$, $\sigma_{yz}$, and $\sigma_{yx}$ accordingly. Therefore, the 3×3 matrix tensor can be reorganized to ($\sigma_{xx}$, $\sigma_{yy}$, $\sigma_{zz}$, $\sigma_{yz}$, $\sigma_{zx}$, $\sigma_{xy}$) and denoted as ($\sigma_1$, $\sigma_2$, $\sigma_3$, $\sigma_4$, $\sigma_5$, $\sigma_6$). The same simplification rules are also applied to strain ($\varepsilon$) and resistivity afterward. In isotropic cases, stiffness
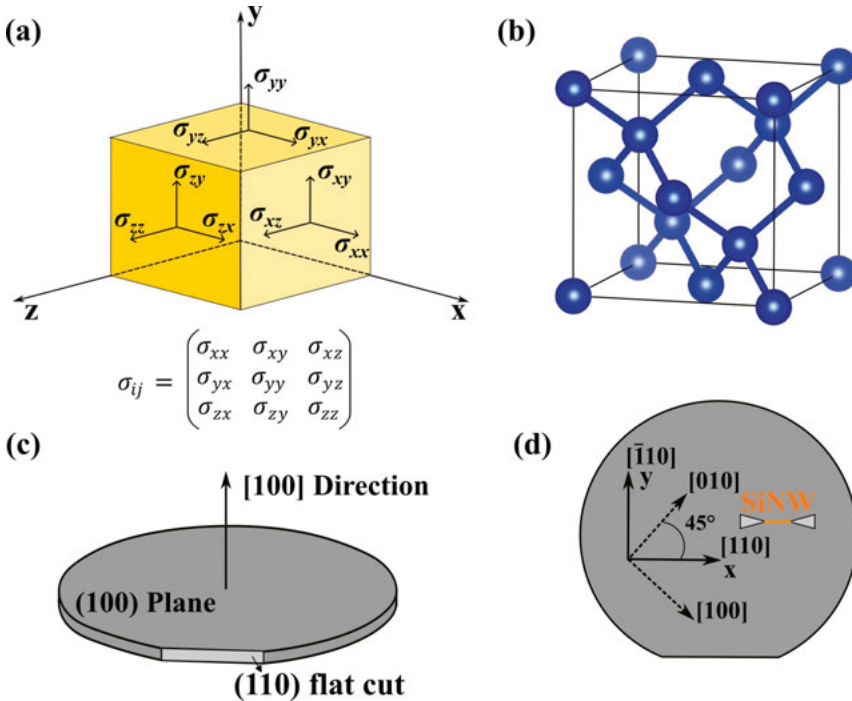


*Figure 4.1. Schematics of (a) stress tensors, (b) silicon lattice structure, (c) orientation of a 100-mm diameter wafer with a flat cut of the (110) plane, and (d) direction and axes in a (100) wafer.*

can be represented by a single scalar, Young's modulus, to correlate σ and ε. However, in anisotropic cases like silicon, a 6×6 matrix is required to project $\varepsilon$ to $\sigma$. Benefiting from the high symmetry of silicon lattice, which belongs to cubic $Fd\bar{3}m$ space group as shown in Fig. 4.1(b), the stiffness tensor can be simplified and specified with only three independent components 11, 12, and 44 as:

$$\begin{bmatrix} \sigma_1 \\ \sigma_2 \\ \sigma_3 \\ \sigma_4 \\ \sigma_5 \\ \sigma_6 \end{bmatrix} = \begin{pmatrix} C_{11} & C_{12} & C_{12} & 0 & 0 & 0 \\ C_{12} & C_{11} & C_{12} & 0 & 0 & 0 \\ C_{12} & C_{12} & C_{11} & 0 & 0 & 0 \\ 0 & 0 & 0 & C_{44} & 0 & 0 \\ 0 & 0 & 0 & 0 & C_{44} & 0 \\ 0 & 0 & 0 & 0 & 0 & C_{44} \end{pmatrix} \begin{bmatrix} \varepsilon_1 \\ \varepsilon_2 \\ \varepsilon_3 \\ \varepsilon_4 \\ \varepsilon_5 \\ \varepsilon_6 \end{bmatrix}. \tag{4.2}$$

The matrix in (4.2) is derived in the specific coordinate system of axes, where the $x$-axis, $y$-axis, and $z$-axis represent [100], [010], and [001] directions of the crystalline structure, respectively. However, our starting wafer has a (100) surface and a flat cut of the (110) plane as shown in Fig. 4.1(c) and (d). Since the SiNW is aligned with [110] direction, the coordinate system has to be rotated by 45° in the (100) plane to fit our SiNW. Therefore, the stiffness matrix is also changed to [88]

$$\begin{bmatrix} \sigma_1 \\ \sigma_2 \\ \sigma_3 \\ \sigma_4 \\ \sigma_5 \\ \sigma_6 \end{bmatrix} = \begin{pmatrix} 194.5 & 35.7 & 64.1 & 0 & 0 & 0 \\ 35.7 & 194.5 & 64.1 & 0 & 0 & 0 \\ 64.1 & 64.1 & 165.7 & 0 & 0 & 0 \\ 0 & 0 & 0 & 79.6 & 0 & 0 \\ 0 & 0 & 0 & 0 & 79.6 & 0 \\ 0 & 0 & 0 & 0 & 0 & 50.9 \end{pmatrix} \begin{bmatrix} \varepsilon_1 \\ \varepsilon_2 \\ \varepsilon_3 \\ \varepsilon_4 \\ \varepsilon_5 \\ \varepsilon_6 \end{bmatrix}$$

(in GPa). (4.3)

This stiffness matrix was calculated based on measured data from bulk Si. We applied this matrix in our finite elements method (FEM) simulation operated in COMSOL. However, with Si beam downscaling, the surface-to-volume ratio increases dramatically, and the impact from defects on the surface cannot be ignored anymore [89]–[91]. In addition, the temperature rise due to thermal heating could also change the mechanical properties of SiNW. These factors are not considered during our simulation for simplicity. Therefore, the simulated results should be carefully evaluated in real signal analysis.

The relationship between current density $(\vec{J})$ and electric field $(\vec{E})$ can be described with microscopic Ohm's law as

$$\vec{J} = \sigma\vec{E}, and \ \vec{E} = \rho\vec{J}, \tag{4.4}$$

in which $\sigma$ is conductivity and $\rho$ is resistivity. In single crystal material, the $\sigma$ and $\rho$ are generally anisotropic. Therefore, they are second rank tensors relating vector $\vec{J}$ and $\vec{E}$, which can be formatted by a 3×3 matrix similar to strain. For silicon single crystal with cubic symmetry, the diagonal components equal to resistivity, $\rho_{xx} = \rho_{yy} = \rho_{zz} = \rho_0$, while others equal to zero, $\rho_{xy} = \rho_{yz} = \rho_{zx} = 0$. When the symmetry of the silicon lattice deteriorates under stress, the resistivity sensor transforms into a symmetric matrix as

$$\begin{pmatrix} \rho_1 & \rho_6 & \rho_5 \\ \rho_6 & \rho_2 & \rho_4 \\ \rho_5 & \rho_4 & \rho_3 \end{pmatrix} = \rho_0 \begin{pmatrix} 1 & 0 & 0 \\ 0 & 1 & 0 \\ 0 & 0 & 1 \end{pmatrix} + \rho_0 \begin{pmatrix} \Delta_1 & \Delta_6 & \Delta_5 \\ \Delta_6 & \Delta_2 & \Delta_4 \\ \Delta_5 & \Delta_4 & \Delta_3 \end{pmatrix}, \tag{4.5}$$

where $\Delta_i$ represents the relative change of cthe orresponding resistivity including 6 components. Under stress, $T$, the relative change of resistivity can be calculated through $(\Delta) = (\Pi)(T)$. $(\Pi)$ is the piezoresistive coefficient tensor represented as a 6×6 matrix. This complicated piezoresistive coefficient tensor can be simplified in the same way as stiffness tensor according to the symmetry of silicon lattice, then we can get [92]

$$\begin{pmatrix} \Delta_1 \\ \Delta_2 \\ \Delta_3 \\ \Delta_4 \\ \Delta_5 \\ \Delta_6 \end{pmatrix} = \begin{pmatrix} \pi_{11} & \pi_{12} & \pi_{12} & 0 & 0 & 0 \\ \pi_{12} & \pi_{11} & \pi_{12} & 0 & 0 & 0 \\ \pi_{12} & \pi_{12} & \pi_{11} & 0 & 0 & 0 \\ 0 & 0 & 0 & \pi_{44} & 0 & 0 \\ 0 & 0 & 0 & 0 & \pi_{44} & 0 \\ 0 & 0 & 0 & 0 & 0 & \pi_{44} \end{pmatrix} \begin{bmatrix} T_1 \\ T_2 \\ T_3 \\ T_4 \\ T_5 \\ T_6 \end{bmatrix}. \tag{4.6}$$

There are only three independent components in $(\Pi)$, which are $\pi_{11}$, $\pi_{12}$, and $\pi_{44}$. These components were experimentally characterized by C. S. Smith [92] as listed in Table 4.1. Please note that this piezoresistive coefficient tensor was derived in the crystallographic coordinate system. In an arbitrary coordinate system, the tensors in $(\Delta) = (\Pi)(T)$ need to be transformed with new base

vectors to $(\Delta') = (\Pi')(T')$, in which $(\Delta')$ and $(T')$ equal to $(R) (\Delta)$ and $(R) (T)$ accordingly. With rotation matrix, $(R)$, we can obtain

$$\Pi' = R \cdot \Pi \cdot R^{-1}. \tag{4.7}$$

Since our devices were fabricated on *p*-type (100) wafer, as shown in Table 4.1, the shear piezoresistive coefficient, $\pi_{44}$, is more significant than the $\pi_{11}$ and $\pi_{12}$. To collect the highest piezoresistive gain, the SiNW was patterned along [110] direction parallel to the wafer flat cut, with the longitude piezoresistive gauge equals to $(\pi_{11}+\pi_{12}+\pi_{44})/2$ [92].

Table 4.1. piezoresistive coefficient tensor components of silicon (unit in $10^{-11}$ Pa$^{-1}$)

|  | $\pi_{11}$ | $\pi_{12}$ | $\pi_{44}$ |
|---|---|---|---|
| *p-type* | 6.6 | -1.1 | 138.1 |
| *n-type* | -102.2 | 53.4 | -13.6 |

The piezoresistive gauges in Table 4.1 are measured on high-resistivity bulk silicon material. However, it has been observed that the piezoresistive coefficient is relevant to the doped impurity level [52]. For *p*-type silicon at room temperature, the $\pi_{44}$ decreases from ~$140\times10^{-11}$ Pa$^{-1}$ at $10^{15}$ cm$^{-3}$ to ~$50\times10^{-11}$ Pa$^{-1}$ at $10^{18}$ cm$^{-3}$. To maintain a decent piezoresistive coefficient, the piezoresistor in our device was moderately doped (instead of heavy doping) at about $5\times10^{18}$ cm$^{-3}$. Another surprising phenomenon observed in SiNW is giant piezoresistance with dimension downscaling. In the [111] direction, the piezoresistive coefficient of bottom-up growing *p*-type SiNW reaches $-3550\times 10^{-11}$ Pa$^{-1}$ in comparison with a bulk value of $-94\times 10^{-11}$ Pa$^{-1}$[49]. A similar trend was also found in top-down fabricated SiNW [93], while the piezoresistive coefficient was strongly dependent on surface condition [94]. More careful studies are still needed to draw a solid conclusion on giant piezoresistance. In this thesis work, the piezoresistive effect of SiNW is conservatively treated as a bulk condition.

## 4.2 Finite elements simulation on SiNW-net

As discussed in Chapter 1.3.2, a nanoelectromechanical sensor based on a SiNW-net was designed to detect bacterial motility. To enhance the piezoresistive gain, the piezoresistive element should be placed at the strain-concentrated region. By modulating the dimensional parameters of SiNW-net, the strain could also be enhanced. In this section, we performed FEM analysis using COMSOL to engineer the geometry of the device.
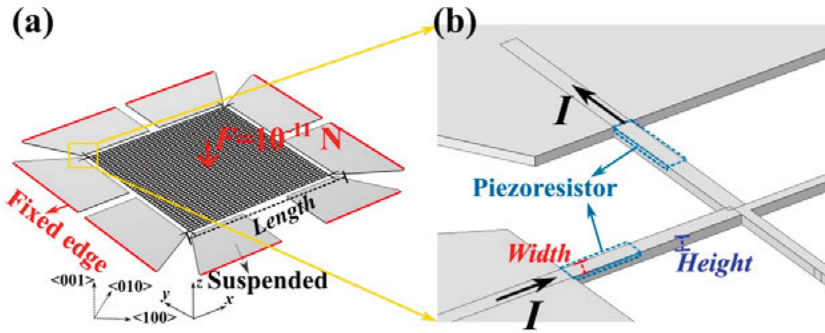


*Figure 4.2 (a) Device geometry of the model simulated in COMSOL. (b) Zoom-in view of the piezoresistive element at the corner of the device.*

In Fig. 4.2(a) the device model is illustrated with a loading force and boundary conditions. The fully suspended area in the device with a span length of 50 μm is composed of the SiNW-net region and supporting pads in which the edges are fixed during simulation. The loading force applied at the center of the SiNW-net is set to $10^{-11}$ N of the same magnitude as the force generated by *E. coli*. As discussed in section 4.1, both piezoresistive gauge and stiffness are fourth rank tensors with specific expressions in different coordinate systems. In this simulation, the device geometry is positioned within a global system where the SiNW follows either the x-axis or y-axis, while the material coordinate system is rotated along the z-axis by 45°. Subsequently, the *p*-type SiNW is patterned along [110] direction, which is the superior direction as calculated in the 4.1 section. As a suspended net, it's obvious that the stress will be concentrated at the supporting ends at the corner depicted in Fig. 4.2(b). Therefore, the piezoelements are located adjacent to the ends of the SiNW-net as marked by dashed boxes in Fig. 4.2(b). Three geometric parameters are carefully evaluated during simulation, including the span of the suspended SiNW-net, the height, and width of the SiNW in supporting ends.

The simulated stress distribution in a device of 30 μm (length) × 55 nm (height) × 100 nm (width) dimension is plotted in Fig. 4.3(a). As we expected, the stress is mainly concentrated on the top and bottom surfaces symmetrically. The stress tensor at the top of the slice cross-section is read as

$$(T) = \begin{pmatrix} 7.5 \times 10^5 & -3.8 \times 10^5 & 1785.9 \\ -3.8 \times 10^5 & -6.4 \times 10^4 & 1132.8 \\ 1785.9 & 1132.8 & 175.7 \end{pmatrix} \text{(in Pa)}.$$

In the stress tensor, the components $\sigma_{xx}$ and $\sigma_{xy}$ are more dominant than others, thus the stress tensor is simplified to $(7.5 \times 10^5, 0, 0, 0, 0, -3.8 \times 10^5)$ (in Pa). The simulated stress tensors are illustrated on a slice surface perpendicular to the
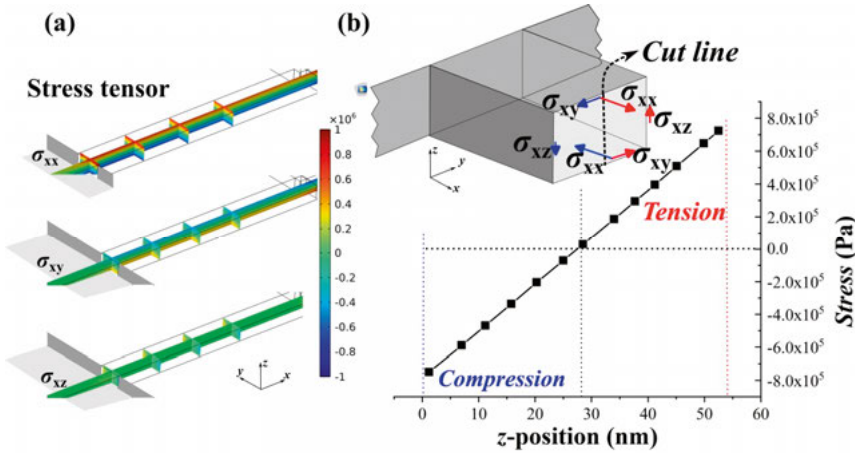


Figure 4.3 (a) Simulated stress tensors distribution in sliced cross-section with color bar in units of Pa. (b) Schematic of stress tensor $\sigma_{xx}$ in cross-section of SiNW and tensor component $\sigma_{xx}$ versus z-position in the cutting line.

SiNW, in which the length of arrows represents the relative value of tensors, as seen in Fig. 4.3(b). The stress $\sigma_{xx}$ is dominant and plotted versus the z-position along the dashed cutting line. The nutrient surface is located in the middle without any stress. $\sigma_{xx}$ increases linearly to its maximum at the top surface and decreases negatively towards the bottom surface. In the following part, only stress at the top surface is taken into account for piezoresistance calculation.

Since the material coordinate system is rotated by 45°, the piezoresistive coefficient tensor in global coordinate can be derived by multiplying the rotation matrix as (4.7), which is comprised of direction cosines ($l$, $m$, $n$) as
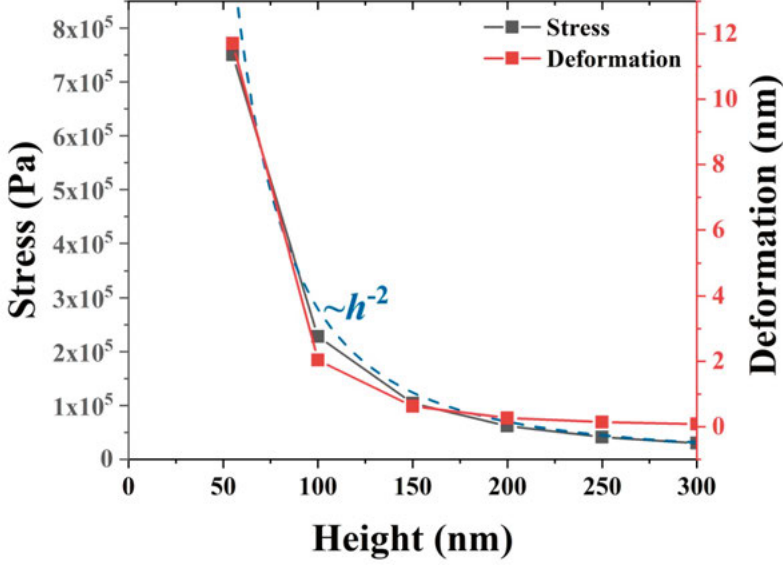
Figure 4.4 Simulated stress tensor $\sigma_{xx}$ at top surface and maximum deformation of SiNW-net versus SiNW height with dashed line representing $h^{-2}$ behavior. Device size: 30 $\mu m$ span length and 100 nm width.

$$(R) = \begin{pmatrix} l_1 & m_1 & n_1 \\ l_2 & m_2 & n_2 \\ l_3 & m_3 & n_3 \end{pmatrix} = \begin{pmatrix} \sqrt{2}/2 & \sqrt{2}/2 & 0 \\ -\sqrt{2}/2 & \sqrt{2}/2 & 0 \\ 0 & 0 & 1 \end{pmatrix}.$$

Then, the relative resistivity variation can be calculated by

$$\Delta = R^{-1} \cdot \Pi \cdot R \cdot T. \tag{4.8}$$

Since the current in SiNW is forced along the x-axis, the relative change of resistance equals $\Delta_{xx}$ as

$$\frac{\Delta R}{R} = \Delta_{xx} = \sigma_{xx}\pi'_{11} + \sigma_{xy}\pi'_{16}, \tag{4.9}$$

in which

$$\pi'_{11} = \pi_{11} - 2(\pi_{11} - \pi_{12} - \pi_{44})(l_1^2 m_1^2 + l_1^2 n_1^2 + m_1^2 n_1^2),$$
$$\text{and } \pi'_{16} = (\pi_{11} - \pi_{12} - \pi_{44})(l_1^3 l_2 + m_1^3 m_2 + n_1^3 n_2). \tag{4.10}$$

64

In this case, $\pi'_{11} = (\pi_{11} + \pi_{12} + \pi_{44})/2$ and $\pi'_{16} = 0$. Then the relative change of resistance, $\Delta R/R = (\pi_{11} + \pi_{12} + \pi_{44}) \times \sigma_{xx}/2$, is solely proportional to $\sigma_{xx}$. Finally, the piezoresistance signal can be easily calculated by simulating the $\sigma_{xx}$ term individually.

To enhance the piezoresistance signal, the geometry of the SiNW-net should be fastidiously optimized to amplify the stress collected by the piezoresistor at the top surface of the SiNW. Guided by Eq. (1.7), $\sigma_{max} = 3FL/4wh^2$, the width, height, and span of SiNW-net are simulated. $\sigma_{xx}$ and deformation dependence of height are plotted in Fig. 4.4. As SiNW gets thinner, both $\sigma_{xx}$ and deformation increase roughly following the $h^{-2}$ tendency (see the dashed line). This behavior coincides well with Eq. (1.7), indicating that we should reduce the thickness of SiNW. Even though sub-10-nm SiNW has been demonstrated in our Lab [95], it's too challenging to precisely control the dopant distribution at the top surface. Considering the mechanical strength and process feasibility, the SOI wa-
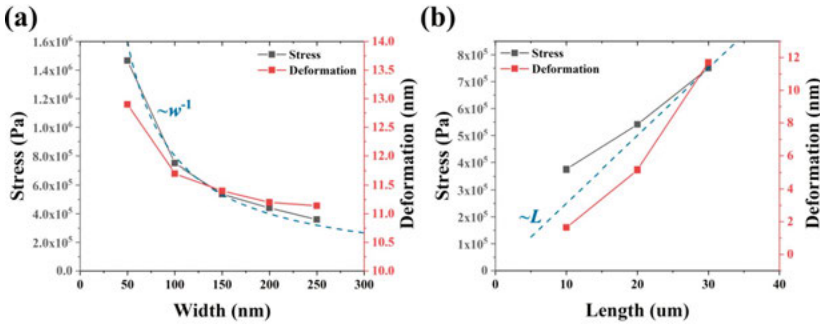


*Figure 4.5 Simulated stress tensor $\sigma_{xx}$ at top surface and maximum deformation of SiNW-net versus (a) SiNW width with length of 30 µm and thickness of 55 nm, and (b) span length of SiNW-net with thickness of 55 nm and width of 100 nm.*

fer from SOITEC company with 55 nm top Si was chosen as the substrate. Besides thickness, the width and span length of SiNW-net are optimized as shown in Fig. 4.5(a) and (b), respectively. When the supporting SiNW gets wider, the stress will be diluted and behave reversely proportional to the width. For our device, sub-100-nm SiNW can be easily achieved. As the span length of the SiNW-net increases, the torque sensed by piezoelement generated due to loading force will be multiplied by the incremental length. This is supported by simulation results depicted in Fig. 4.5(b). Another anticipated benefit of enlarged span length is the enhanced efficiency in capturing bacteria. And more captured bacteria could provide a larger loading force. However, a larger net

could undergo more destructive force during fabrication, especially the suspension step. In the device fabrication section, this concern will be addressed through an optimized SiNW-net suspension process.

## 4.3 SiNW-net fabrication

According to the FEM simulation results, the fabrication process has been optimized to achieve dimensions of ~100 nm in width and ~50 µm in span length. The simplified process flow is illustrated in Fig. 4.6. The starting material is an SOI wafer with 55 nm top Si and 145 nm BOX from SOITEC. Then the S/D, piezoelements, and net region were selectively doped via photoresist-masked $BF_2$ implantation. After resist stripping and dopants activation, the device struc-
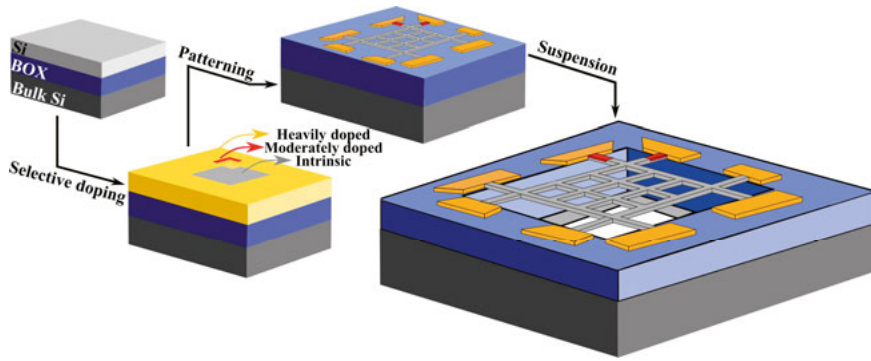


*Figure 4.6. Schematic of simplified process flow.*

ture was defined by combined UVN and HSQ exposure using electron beam lithography (EBL), followed by reactive ion etching (RIE) stopped by the BOX layer. Ni was deposited on the S/D area by electron beam evaporation and lift-off process, then NiSi formed with rapid thermal process (RTP). After depositing Au on S/D with Cr as an adhesion layer, the metal contact was formed. In the next step, the SiNW-net was suspended by etching off the BOX layer underneath. This was the most critical step in the fabrication flow. More detailed information can be found in the following sections. The last step is the surface passivation with $HfO_2$ deposited via atomic layer deposition (ALD) ending with forming gas annealing (FGA). In the below sections, the key steps will be

introduced including structure patterning, wire suspension, and metal arm formation on suspended SiNW-net.

## 4.3.1 SiNW structure patterning

To achieve a sub-100 nm SiNW-net with a span length of 50 μm, the HSQ resist was used to pattern the fine structure, while contact pads were exposed with
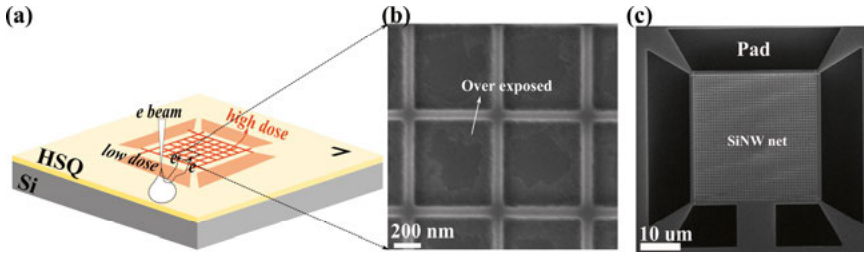


*Figure 4.7. (a) Schematic of electron beam lithography with adjusted electron dose. (b) SEM of over exposed SiNW-net. (c) SEM of well-adjusted SiNW-net with supporting pads in HSQ.*

UVN resist. Based on simulation results in section 4.2, the piezoresistor should be placed on supporting ends of SiNW, demanding high alignment accuracy. In our device fabrication, the supporting pad and SiNW-net were exposed simultaneously in the same layer to ensure alignment. However, the backscattering electrons from the huge supporting pads could subsequently expose the SiNW-net [96], ultimately resulting in lithography failure, as illustrated in Fig. 4.7(a) and (b). To avoid cross exposure, we optimized the exposure step with a locally adjusted dose map. The supporting pad was exposed with low electron dose, whereas higher dose was used to expose the SiNW-net. Finally, the SiNW-net combined with supporting pads was successfully exposed in the same layer after developing as shown in Fig. 4.7(c).

## 4.3.2 SiNW-net suspension

The conventional method to releasing SiNW is simply aqueous HF etching to remove the sacrifice layer and leave the SiNW suspended. It is feasible to suspend short SiNW below 10 μm length. However, when the SiNW was further elongated, the collapsed SiNW was observed as shown in Fig. 4.8(a). There are a few factors that could destroy the suspended structure, such as gravity, built-in stress, and capillary force in the drying step [97]. The calculated gravity force of a SiNW with a dimension of 100 nm × 100 nm × 10 μm ($w*h*l$) is only $2\times10^{-15}$ N. Comparing with the simulation results under $1\times10^{-11}$ N, the generated stress at the fixed end is around 100 Pa under gravity, which could be ignored. If the built-in stress causes the collapse, both upward curvature and downward curvature are expected to be found, while we only saw downward curvature. The built-in stress is thus ruled out. Eventually, we attribute the collapse to the capillary force between SiNW and bulk Si surface underneath after the aqueous HF etching, as illustrated in Fig. 4.8(a). The capillary force results in deformation up to 145 nm (BOX thickness) and permanent plastic deformation. As the capillary force exists between two surfaces in close vicinity, naturally, a straightforward way to eliminate capillary force is to remove one
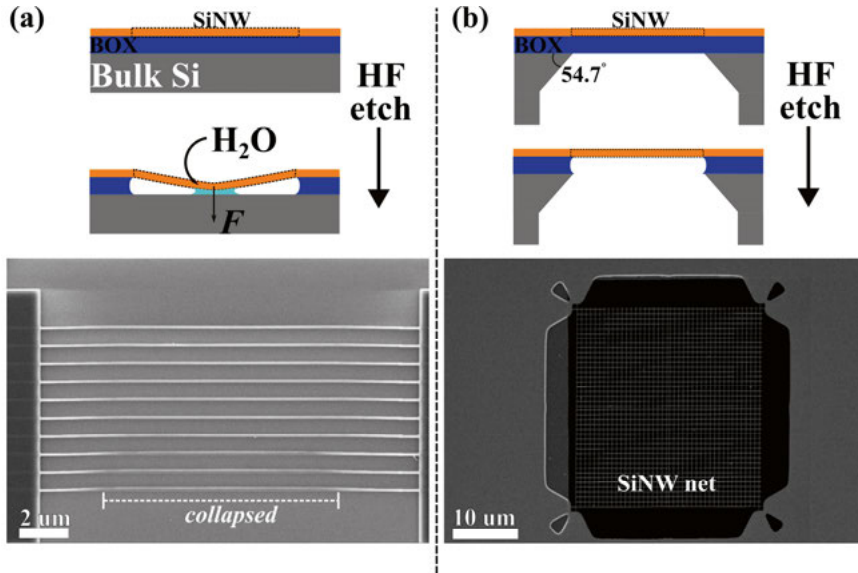


*Figure 4.8. Schematics of SiNW suspension process with corresponding SEM image of (a) top side HF etching, and (b) etching first from bottom side, followed by top-side etching.*

of the surfaces. Consequently, we optimized the etching step as follows. First, a trench in the substrate was formed by deep reactive ion etching (DRIE), followed by KOH wet etching stopped by the BOX layer. In this way, a freestanding membrane comprised of top Si structures and a BOX layer was formed. Afterward, the membrane could be safely processed with aqueous HF, and a suspended SiNW-net was achieved without visible deformation as shown in Fig. 4.8(b).

### 4.3.3 Metal arm formation on suspended SiNW-net

To calibrate the sensitivity of our SiNW-net electromechanical sensor, we designed and fabricated a metal Lorentz arm on top of the suspended SiNW-net. A desired Lorentz force could then be precisely generated on the SiNW-net by passing current through the metal Lorentz arm in a supplied magnetic field. However, the metal layer is not compatible with aqueous HF etching, while a suspended SiNW-net cannot sustain resist spin and lift-off process either. Then, we developed a metal deposition process by combining metal lift-off with vapor-phase HF etching.
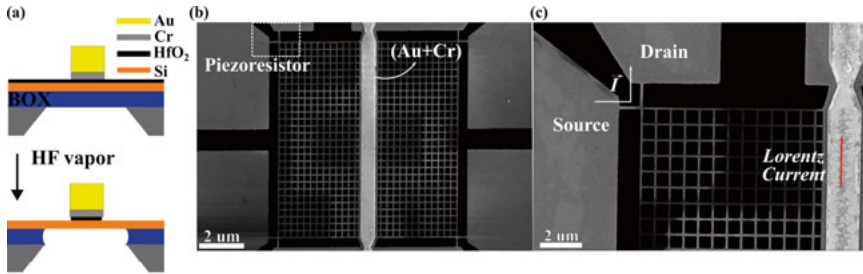


*Figure 4.9. (a) Schematics of SiNW releasing process with metal arm, (b) SEM of suspended SiNW-net with metal arm formed, and (c) zoom-in SEM of supporting corner of SiNW-net.*

After forming the freestanding membrane by KOH wet etching, the top surface was passivated with $HfO_2$ via ALD to isolate the metal loop from the silicon structure. Then Cr and Au layers were deposited by evaporation and lift-off process. Vapor-phase HF was applied to etch the BOX layer, containing the vapor of HF and $H_2O$. A trace amount of $H_2O$ vapor plays the role of catalyst, which only appears on the surface of $SiO_2$, thus the metal will not be damaged in the absence of aqueous HF. The schematics of the process and SEM of the resulting device are presented in Fig. 4.9.

The Lorentz loop can provide the desired loading force in magnetic field. However, the thick metal layer also shares the generated stress. To assess the stress applied to piezoelement, we conducted an FEM simulation using COMSOL as shown in Fig. 4.10(a). The force is uniformly loaded on the Lorentz loop and the stress could still be concentrated at the supporting corner. The strain and maximum displacement are plotted versus the thickness of the Au layer in Fig. 4.10(b). As Au gets thicker, the stress and displacement will be diluted by ten times when thickness reaches 150 nm. In order to strike a balance between conductivity and strain, the thickness is determined to be 50-60 nm.
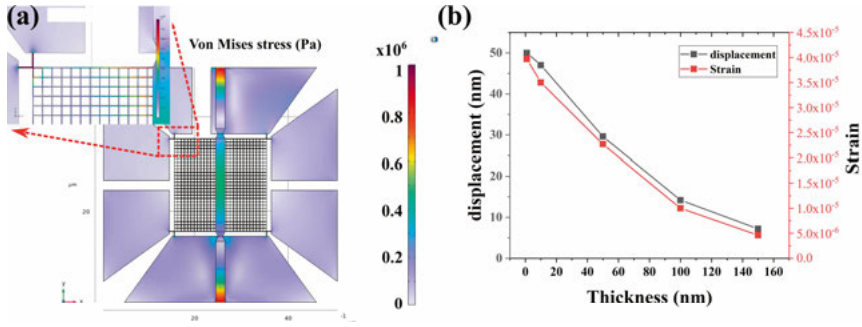


Figure 4.10. (a) Simulated Von Mises stress distribution on SiNW-net. (b) maximum displacement and strain on piezoresistor versus thickness of Au layer.
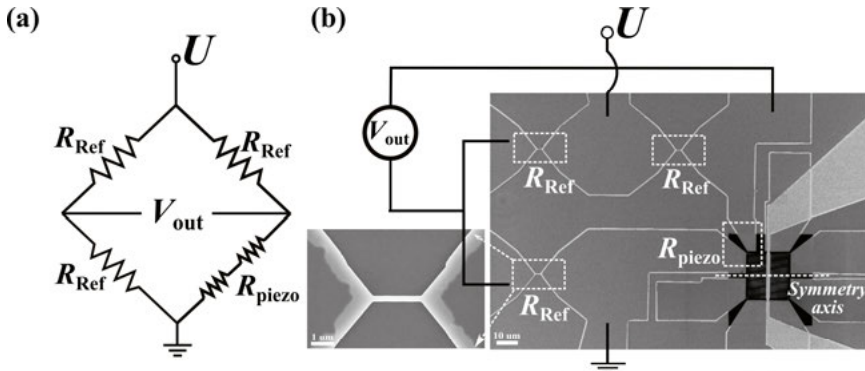


Figure 4.11. (a) Diagram of Wheatstone bridge and (b) SEM of Wheatstone in device with reference resistor.

## 4.4 SiNW-net calibration actuated by Lorentz force

As discussed in section 4.2, the simulated stress $\sigma_{xx}$ reaches $7.5\times10^5$ Pa at the top surface of SiNW, and the estimated relative resistance change is $5.7\times10^{-4}$ under $1\times10^{-11}$ N loading force. To detect such small resistance variation, we integrated the SiNW-net into a Wheatstone bridge with short SiNWs as reference resistors presented in Fig. 4.11. By measuring output voltage across the bridge, relative resistance change can be read out as

$$V_{out} = \frac{\Delta R}{2R+\Delta R} \cdot \frac{U}{2} \approx \frac{\Delta R}{R} \cdot \frac{U}{4}. \tag{4.11}$$

With Wheatstone bridge circuit design, the thermal heating effect and signal drift can be also eliminated, as they contribute to all resistors equally. Therefore, the pseudo signal from the environment can be filtered out through the bridge.

To accurately read out real-time signals, a lock-in amplifier was utilized which can also supply Lorentz current from reference AC output terminals as shown in Fig. 4.12. Here, the working principle of a lock-in amplifier is briefly introduced. Assume that the input signal $s(t)$, the reference signals $r_x(t)$, and $r_y(t)$ from the oscillator are

$$s(t) = \sqrt{2}V_{sig}\sin(2\pi f_{sig}t + \theta_{sig}),$$

$$r_x(t) = \sin(2\pi f_{ref}t + \theta_{ref}), and\ r_y(t) = \cos(2\pi f_{ref}t + \theta_{ref}), \tag{4.12}$$

where $V_{sig}$ is the root mean square (RMS) amplitude, $f$ denotes frequency, and $\theta$ is phase. The mixed signal $V_x(t)$ and $V_y(t)$ from signal mixer can be derived as

$$V_x(t) = (V_{sig}/\sqrt{2})\begin{Bmatrix} \cos(2\pi[f_{sig}-f_{ref}]t + \theta_{sig}-\theta_{ref}) \\ -\cos(2\pi[f_{sig}+f_{ref}]t + \theta_{sig}+\theta_{ref}) \end{Bmatrix},$$

$$And\ V_y(t) = (V_{sig}/\sqrt{2})\begin{Bmatrix} \sin(2\pi[f_{sig}-f_{ref}]t + \theta_{sig}-\theta_{ref}) \\ +\sin(2\pi[f_{sig}+f_{ref}]t + \theta_{sig}+\theta_{ref}) \end{Bmatrix}. \tag{4.13}$$

Our low-pass filter (LPF) in the lock-in amplifier will eliminate the high-frequency term $(f_{sig}+f_{ref})$ and will only allow the left term with $(f_{sig}-f_{ref)}$

limited around 0 by bandwidth. Therefore, the signal $V_{sig}$ at frequency close to $f_{ref}$ can be extracted from $V_x$ and $V_y$ as

$$V_{sig} = \sqrt{V_x^2 + V_y^2}, \ and \ \theta = tan^{-1}(V_x/V_y). \tag{4.14}$$

In our device measurement (see Fig. 4.12), the reference AC outputs from
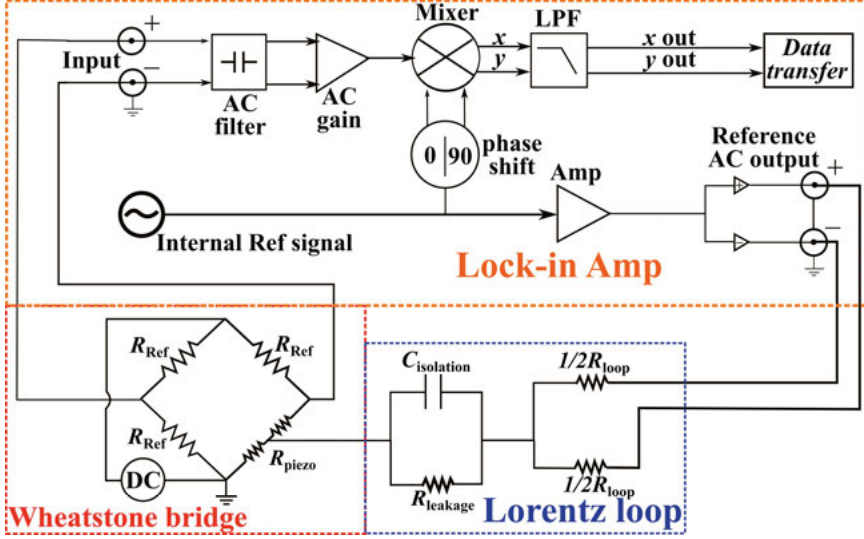


*Figure 4.12. Equivalent circuit diagram including Wheatstone bridge, Lorentz loop, and lock-in amplifier.*

the amplified internal oscillator are connected to the Lorentz loop with a reference frequency, $f_{ref}$. Therefore, the piezoresistive signal stimulated by Lorentz force will be in the same frequency as $f_{ref}$. Thus, only the stimulated signal at $f_{ref}$ could be measured by a lock-in amplifier, and the low-frequency noise would be filtered out.

To reveal the piezoresistive signals, the signal detection limit could be improved by enhancing the piezoresistive gain or suppressing noise. The piezoresistive gain has been discussed in the simulation and fabrication sections. Considering the noise suppression during measurement, there are two dominant noise sources, $1/f$ device noise and interference from the Lorentz loop via capacitance coupling. When reference frequency, $f_{ref}$, increases, the picked $1/f$ device noise will be reduced, whereas the interference from the Lorentz loop will

be enhanced due to lower capacitive reactance between the Lorentz loop and Wheatstone bridge. To minimize total noise, we set the frequency to 50 kHz.

As illustrated in Fig. 4.12 (Lorentz loop module), the interference should be zero if the Lorentz loop is perfectly symmetrical relative to the piezoresistor, thus the interference from the positive port could neutralize that of the negative port. In fact, the interference always exists due to geometric asymmetry (see
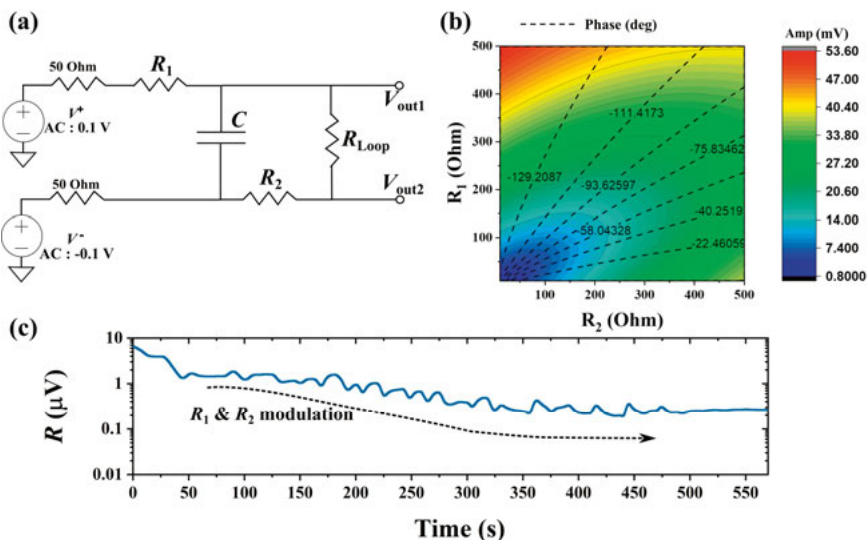


Figure 4.13. (a) Diagram of compensation circuit, (b) phase and amplitude map of ($V_{out1}$ + $V_{out2}$) versus $R_1$ and $R_2$, and (c) Lorentz interference noise optimization by modulating $R_1$ and $R_2$.

Fig. 4.11(b)). To overcome this issue, we designed a compensation circuit connected to the Lorentz loop as depicted in Fig. 4.13(a). The $R_{Loop}$ mimics the resistance of the Lorentz loop (2 kΩ). $R_1$ and $R_2$ are modulated to control the current through a capacitor ($C$) and the voltage drop across $R_{Loop}$, which could adjust the phase and amplitude of the effective stimulating signals ($V_{out1}$, $V_{out2}$) on the Lorentz loop as shown in Fig. 4.13(b). The asymmetric capacitive coupling between the Lorentz loop and bridge could then be well compensated by adjusting the pre-built phase and amplitude shift of the stimulating signals. Indeed, by altering $R_1$ and $R_2$, the interference from the Lorentz loop can be effectively suppressed from ~10 μV to 300 nV (see Fig. 4.13(c)).

To supply a controllable magnetic field, we designed a homemade electromagnet as shown in Fig. 4.14(a) and (b). The core was made of ferrites N87, a kind of ceramic material containing MnZn, which is usually used in power transfer with high flux permeability. The coil is twined by copper wire with 1.5
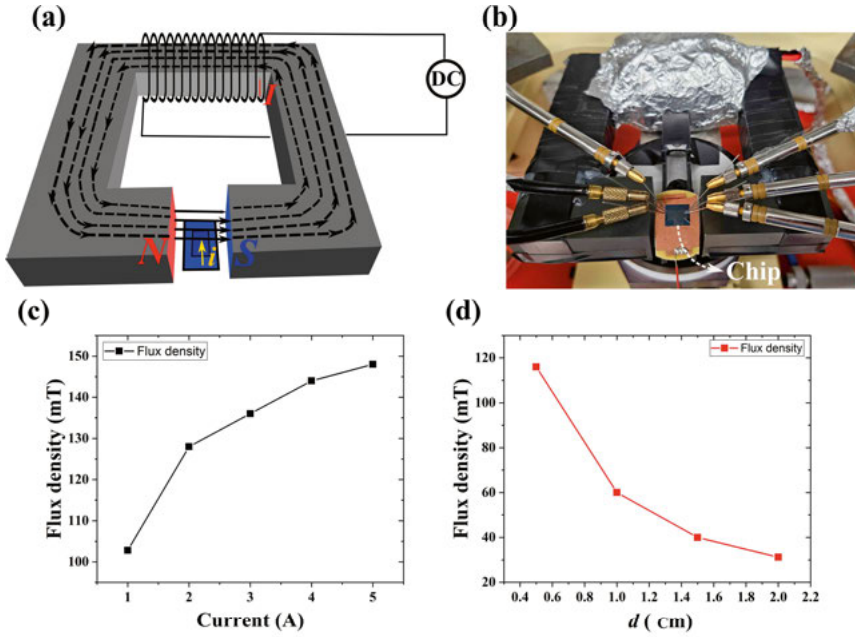
*Figure 4.14. (a) Schematic of the electromagnet, (b) photo image of setup, (c) measured flux density vs. current with 5 mm polar distance, and (d) flux density vs. polar distance under 1 A coil current.*

$\Omega$ total resistance powered by a DC source. In Fig. 4.14(c), the magnetic flux density measured by a Hall sensor is plotted versus current showing that the flux density increases with more current supplied in coil, but it cannot raise linearly due to decreased permeability under higher flux density. When polar faces are separated, the flux will disperse into surrounding space, resulting in reduced flux density in front of the polar surface as shown in Fig. 4.14(d). During measurement, we got 50 mT flux density with a 2 cm gap distance which could provide 0.1 nN under a Lorentz current of 50 μA in a 50-μm suspended Lorentz loop.

Currently, we achieved a 30-μm suspended SiNW-net with metal loop stacked on top. The lock-in measurement setup was optimized to effectively suppress interference from Lorentz current to ~300 nV. And 0.1 nN Lorentz force was loaded on a suspended net by an electromagnet. However, the piezoresistance signal has not been observed as we predicted. Most probably, the implanted dopants were not located correctly in the thin SiNW. And the traps induced by ion implantation might deplete carriers on the surface, thus inhibiting piezoresistive signal. To further optimize the piezoresistor, the autodoping

process observed during RTP) could offer a promising solution, which will be introduced in the next section.

# 4.5 Shallow junction formation via lateral autodoping

Autodoping is a well-known phenomenon of unwanted dopant transfer in the silicon epitaxy process [98]. However, in this thesis work, we discovered boron lateral autodoping in the normal rapid thermal process (RTP), and it could potentially be used to form the shallow peizoelement at the SiNW surface.

To evaluate the autodoping results, we prepared test samples on SOI wafers. The process started with thermal oxidation to form a 5-nm thick cap oxide. Then 8-mm long UVN negative resist strips with varying widths ranging from 100 µm to 500 µm were exposed in repeating 1 cm × 1 cm chips on the wafer by electron beam lithography (EBL) as implantation mask. $BF_2^+$ ions with 25 keV energy and at a dose of $1\times10^{15}$ cm$^{-2}$ were implanted into the masked wafer. After the UVN photoresist removal, an array of 10 four-point probe test structures surrounded by 2 µm wide gaps at their boundaries were patterned by EBL in each of the unimplanted regions, as presented in Fig. 4.15(a). The gap was etched by reactive ion etching to completely separate the test structure from the implanted area. Right after the cap oxide stripping in 50:1 HF solution, the samples were loaded to a RTP furnace (RT600s system from Modular Process Technology Corporation) for annealing at 950 °C in 80 psi $N_2$ ambient. The ramp rate of the RTP is about 45 °C/s.

Then the autodoping result was confirmed by quick two-terminal tests between $V_s$ (grounded) and $V_d$ on the four-point test structure depicted in Fig. 4.15(a). The $I_d$ vs $V_d$ curves for samples under different process conditions are shown in Fig. 4.15(c). For the sample without cap oxide, the measured $I_d$ increased linearly with increasing $V_d$ and reached ~100 nA at 0.1 V $V_d$. This measured conductivity indicates that the unimplanted area is doped by boron via the ambient since the solid-state diffusion to the test structure is blocked by
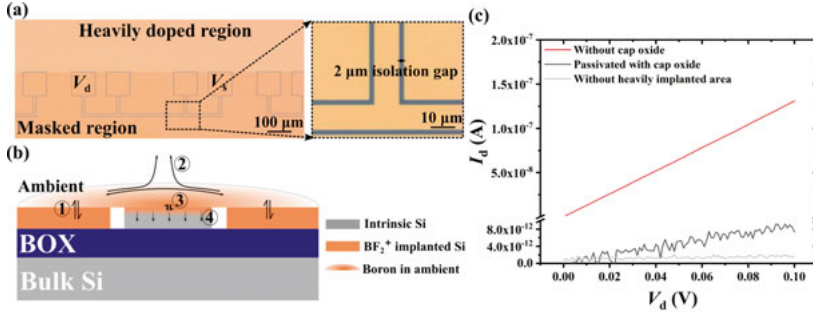
Figure 4.15. (a) Left: Optical image of a four-point test structure surrounded by a 2 μm wide isolation gap in the unimplanted area; right: zoom-in view of the isolation gap. (b) Schematic of boron autodoping process including boron evaporation from heavily implanted area (step 1), transport in gas phase (step 2), redeposition to unimplanted surface (step 3) and solid phase diffusion (step 4). (c) Two terminal $I_d$ vs. $V_d$ test results on the test structure processed under different RTP conditions.

the isolation gap. Furthermore, the ohmic contact behavior to the test structure also implies high concentrations of surface dopants. The autodoping can be well blocked by a 5-nm cap oxide, as evidenced by the $I_d$-$V_d$ plot measured in an otherwise identical sample capped with 5 nm $SiO_2$ (Fig. 4.15(c)). To further rule out possible dopant sources in the RTP furnace, a reference chip without any implanted area or cap oxide was annealed at the same annealing condition. The measured current is still in the pA range (Fig. 4.15(c)), which confirms that the implanted area is the source of dopants in the autodoping process.
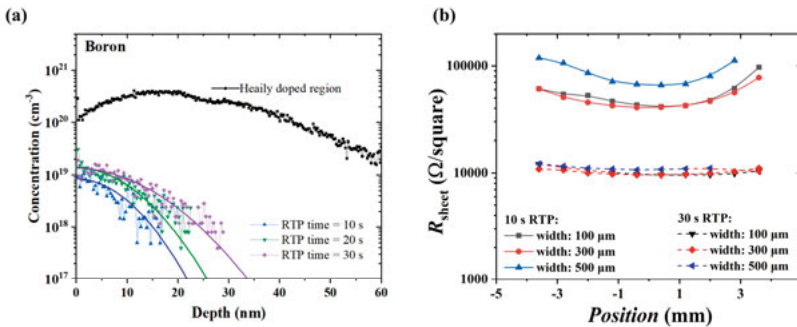


Figure 4.16. (a) Boron ToF-SIMS depth profiles and their fitting curves of the center of the 100 μm wide unimplanted area on samples with different RTP annealing times (10 s, 20 s, and 30 s). (b) Sheet resistance mapping unimplanted region with different $W_{window}$ and annealing time at 950 °C on a single chip.

76

The sequence of the lateral boron autodoping process during the RTP is illustrated in Fig. 4.15(b): evaporation of boron from the implanted area to the gas phase (step 1); boron transport in the gas phase (step 2); boron redeposition to the surface of the unimplanted area (step 3); and boron diffusion from the surface to the bulk of the unimplanted area (step 4). To further confirm and understand boron autodoping in the unimplanted area, the implanted samples were annealed at 950 °C in RTP for different times after the removal of the cap oxide. Additionally, ToF-SIMS measurements were carried out in the center of the unimplanted area as shown in Fig. 4.16(a). No detectable fluorine signal was found in the unimplanted area, confirming this area was very well blocked by the photoresist mask during the $BF_2$ implantation process. No boron signal was detected in the unimplanted area of a control sample before the RTP annealing either. In direct contrast, in the annealed samples boron concentration reaches $10^{19}$ cm$^{-3}$ at the surface of the unimplanted area and declines to $5\times10^{17}$ cm$^{-3}$ (boron detection limit in the ToF-SIMS analysis) with increasing depth. The boron depth profiles also exhibit a clear dependence on the annealing time, which could be predicted by the diffusion equation as [99]

$$C(x,t) = k_e C_m [erfc\left(\frac{x}{2\sqrt{Dt}}\right) - erfc(\frac{x}{2\sqrt{Dt}} + h\sqrt{\frac{t}{D}})], \qquad (4.15)$$

in which $k_e$ is the effective segregation coefficient, $C_m$ is the boron gas phase concentration, $D$ is the diffusivity, and $h$ is the boron evaporation coefficient. The detailed equation derivation can be found in **Paper V**. As shown by the solid lines in Fig. 4.16(a), all three boron diffusion profiles from 10 s to 30 s RTP annealing can be fitted with Eq. (4.15). Furthermore, the average boron diffusivity, $D$, extracted from the fitting is $2.2\pm0.5\times10^{-14}$ cm$^2$/s, which is close to the reported values [100], [101]. The extracted evaporation coefficient, $h$, is $2.8\pm0.3\times10^{-9}$ cm/s.

The sheet resistance distribution in 1 cm scale is shown in Fig. 4.16(b). The measured sheet resistance shows location dependence after 10 s processing. Since the width of the unimplanted area (100 μm to 500 μm) is significantly smaller than the dimension of the chip (1 cm), the chip center can be regarded as being fully surrounded by heavily implanted regions. Therefore, boron is readily supplied from the gas phase of the whole surrounding area. However, test structures close to the chip edge can only receive dopants from one side,

requiring longer time for the gas phase above to form balance with that on the heavily implanted area. This leads to less boron redeposition in the chip edge, resulting in higher measured sheet resistance. As the gas phase will be much more uniform with maximum boron concentration after the gas phase is balanced with the heavily doped area, a slight extension of the annealing time under this condition with uniform and higher boron redeposition rate could potentially overwhelm nonuniformity generated at the initial stage of the RTP. Indeed, after the annealing time was extended to 30 s, sheet resistance measured in different locations of the unimplanted areas decreased to 10 kΩ/sq and became much more uniform as shown in Fig. 4.16(b). These results evidence that the use of the boron lateral self-doping process holds great promise to form uniform shallow junctions without the need for advanced doping facilities and high process cost. The damage from ion implantation can be avoided by using the diffusion method, which could potentially satisfy our desired piezoresistor at the top of SiNW. Please see **Paper V** for more discussion.

In the next stage, the autodoping process will be applied to ensure surface shallow doping and proper sheet resistance of the piezoresistor. Once the piezoresistive output gets calibrated, we will proceed with the bacterial motility test.

# 5. Conclusion and Future Perspectives

The ultimate goal of my work is to realize rapid antibiotic susceptibility tests using SiNW-based electronic sensors. Both extracellular pH and bacterial motility have been selected as indicators of bacterial activity. The real-time monitoring of extracellular pH was achieved using a multiplexing SiNWFET array, demonstrating rapid AST capabilities within 30 minutes. Furthermore, the bacterial metabolic early response under ampicillin treatment was carefully studied. To further improve the detection limit of our SiNWFETs, SJGFETs with ultra-low device noise were developed, followed by systematic low-frequency noise analysis. For the purposes of bacterial motility detection, a novel nanoelectromechanical sensor based on SiNW-net was introduced, including FEM simulation, device fabrication, and measurement setup build-up. The major achievements in this thesis are summarized as follows.

1. Rapid antibiotic susceptibility test was achieved using SiNWFET sensors array with a total assay time of less than 30 minutes for different bacterial strains, i.e., *E. coli*, *S. aureus*, and *S. saprophyticus*. The sensors also showed the capabilities of distinguishing bactericidal mechanisms for different antibiotics and quantifying bacteria density in an unknown sample. Based on the monitored pH results, the acidification kinetic parameters can be quantitatively determined, revealing an accelerated $H^+$ production rate at high cell density.

2. The early metabolic response of *E. coli* to ampicillin treatment was systematically investigated using SiNWFET sensors. The dependences of extracellular pH, as a proxy of glucose metabolism activity, on environmental factors, such as cell distribution, temperature, carbon source, and oxygen level, were carefully evaluated first. Our sensors detected early metabolic response indicated by medium alkalization before cell lysis, for the bacteria sample exposed to near-MIC AMP. The detected early response was attributed to acetate uptake due to the accelerated TCA cycle induced by AMP. The sensors also revealed attenuated antibiotic lethality to gene-engineered mutant with suppressed metabolism.

3. Ultra-low noise was demonstrated in SJGFETs on high-quality bonded SOI substrate, by replacing the gate oxide/Si interface of the SiNWFETs with a PtSi/Si Schottky junction. The best achieved $S_{vg}$ are $1.2 \times 10^{-10}$ and $1.1 \times 10^{-11}$ $V^2\mu m^2/Hz$ at 1 Hz and 10 Hz, respectively. These devices can greatly relieve the concern about intrinsic device noise in future biochemical sensing applications.

4. A thorough investigation of LFN in SOITEC-SJGFETs has been performed using the CNF + CMF model specifically modified for SJGFET structure on SOI substrate. It was found that CMF associated with the Coulomb scattering near the BOX/SiNW channel interface plays an insignificant role in the SOITEC substrate. Therefore, confining the current path in the channel bulk brings limited gain in terms of LFN performance. The observed LFN dependence on $V_{sub}$ and $w$ is mainly ascribed to the nonuniform energy distribution of $N_t$. Our experimental results also suggest a possible transition of mobility fluctuation mechanism from Coulomb scattering to surface roughness scattering when the current path is pushed away from the BOX/SiNW channel interface to the channel bulk.

5. A novel SiNW-net-based nanoelectromechanical sensor was developed for bacterial motility detection. Currently, we achieved a 30 μm suspended SiNW-net with a metal Lorentz loop stacked on top. The lock-in measurement setup was optimized to effectively suppress interference from Lorentz current to ~300 nV. And 0.1 nN Lorentz force was loaded on a suspended net by a homemade electromagnet. However, the piezoresistance signal has not been observed as we predicted. Most probably, the implanted dopants didn't locate correctly in thin SiNW. The traps induced by ion implantation might deplete carriers on the surface, thus inhibiting piezoresistive signal.

6. During the SiNW-net sensor fabrication process, we discovered boron lateral autodoping in normal RTP and used it to form shallow junctions with good uniformity for device fabrication. The redeposition of the boron from the gas phase to the solid surface was identified to be the limiting step of the boron incorporation into the undoped silicon area in the RTP process. The autodoping could therefore be engineered by modulating the boron concentration in the gas phase or enhancing the boron transfer rate in the gas-solid interface. Moreover, the autodoping process also avoids the traps and defects induced by the implantation process, which could be applied to form shallow-doped piezoresistors in SiNW-net sensors.

Through this work, extensive knowledge and techniques about bacterial metabolism, antibiotic lethality, device noise, and SiNW sensors fabrication have been accumulated. More efforts should be invested to consummate our bacterial sensing system.

1. An oxygen-sensitive electrode should be integrated into the SiNWFET sensor, thus the oxygen consumption rate can be monitored to directly evaluate the bacterial respiration activity, as compensation for the extracellular pH signal.

2. The gate-all-around SJGFET is expected, which holds great promise to reach extremely low device noise. By optimizing the sensing layer, the detection limit could be vastly improved to meet the requirements of low cell density testing.

3. Boron autodoping process will be involved in SiNW-net fabrication to achieve surface shallow doping for the piezoresistor. After device calibration, bacterial motility tests will be carried out.

# Sammanfattning på Svenska

Det finns ett omedelbart behov av snabb och tillförlitlig testning av antibiotika-känslighet (AST) för att diagnostisera bakteriella infektionssjukdomar och und-vika missbruk av antibiotika. Sådana tester kan ge värdefull information om effektiviteten av antibiotika och dosering. De nuvarande fenotypiska AST krä-ver vanligtvis tillväxt av bakterier till kolonier, vilket ofta tar mer än två dygn. I denna avhandling används nanotrådsfälteffekttransistorer i kisel (SiNWFET) för att bygga snabba AST. En ny upphängd SiNW-nätsensor har också utveck-lats som en potentiell plattform för bakteriell motilitetsdetektering.

Avhandlingen ägnas först åt SiNWFET-sensorer för snabb AST. Den extra-cellulära pH-förändringen som genereras av bakteriell metabolism är en effek-tiv indikator på bakteriell aktivitet, övervakad av våra SiNWFET-sensorer. Snabb AST nås genom att använda SiNWFET-sensorer med en total analystid på mindre än 30 minuter för olika bakteriestammar. Som en fortsättning stude-ras systematiskt det metabola svaret av bakterien *E. coli* under ampicillinbe-handling. När den utsätts för bakteriedödande antibiotika kommer bakteriens andningshastighet att ökas, vilket ökar antibiotikans bakteriedödande förmåga. Detta arbete visar på SiNWFET möjlighet för snabb AST och undersökningar av bakteriell metabolism.

För att ytterligare förbättra detektionsgränsen med SiNWFET föreslås en Schottky Junction-Gated SiNWFET (SJGFET), där det brusiga Si-kanal/gate-oxidgränssnittet ersätts av en PtSi/Si-övergång. Ultralågt lågfrekvent brus de-monstreras i SJGFET tillverkade på ett högkvalitativ kisel-på-isolator (silicon-on-insulator, SOI) substrat. De bäst uppnådda $S_{vg}$-värdena är $1,2 \times 10^{-10}$ och $1,1 \times 10^{-11}$ V$^2$µm$^2$/Hz vid 1 Hz respektive 10 Hz. En grundlig undersökning av lågfrekvent brus (LFN) med användning av CNF + CMF-modellen, specifikt modifierad för SJGFET-struktur på SOI-substrat, har utförts. Det observerade LFN-beroendet av $V_{sub}$ och $w$ förklaras huvudsakligen av den olikformiga ener-gifördelningen av $N_t$.

För att detektera bakteriell mobilitet föreslås en ny SiNW-nätbaserad nano-elektromekanisk sensor, med ett 30 µm upphängt SiNW-nät och en metallisk

Lorentz-ögla ovanpå. Mätning med en lock-in-förstärkare är optimerad för att avsevärt reducera bruset i systemet. Under snabb termisk aktivering (RTP) under tillverkning av komponenten har borautodopning upptäckts, vilket tillskrivs diffusion från omgivningen, begränsad av återdeponering vid ytan. Denna teknik möjliggör grunda övergångar och kommer att integreras i SiNW-nättillverkningen för att bilda välkontrollerade piezoresistorer.

# Acknowledgement

Foremost, I would like to express my heartfelt gratitude to my main supervisor, Prof. Zhen Zhang, who opened the door to the world of semiconductor and scientific research for me. Your profound knowledge and warm encouragement have guided me from being an ignorant student to becoming a doctoral candidate. I am immensely proud to be a member of our research group under your supervision. The time spent with you will definitely enrich my future carrier and life.

I would also give sincere gratitude to my cosupervisor, Dr. Paul Solomon, for your tremendous support and genius suggestions. Whenever I got tired of thinking, those energetic and innovative impression of yours could always inspire me. I am also extremely grateful to my former cosupervisor Dr. Si Chen. You taught me all the basic skills of writing, modelling, analysis, and instruments controlling. I could not complete this work without your participation.

My warm gratitude also goes to Prof. Shili Zhang, who stands as a role model in my mind, with inexhaustible energy and shining spirit. Your semiconductor course provided me the theoretical base of this entire thesis. I also want to express my sincere appreciation to Prof. Sanna Koskiniemi for your generous support and fruitful discussion, through which I got a lot of knowledge of bacteria. Prof. Daniel Primetzhofer, I am deeply grateful for your support on ion implantation, which is extremely critical for all of my devices. I would also like to thank Prof. Ted Johansson for your patient review and time spent on this thesis.

I would also like to express my appreciation to all the people involved in my research life. My gratitude goes out to Prof. Zhibin Zhang, Prof. Tomas Kubart, and Prof. Tomas Nyberg for your courses and knowledge. Thank you, Dr. Allison Jones, your assistance and expertise in the field of bacteria are greatly appreciated. Thank you, Dr. Örjan Vallin. Your consistently reliable and timely assistance with various instruments in the cleanroom is immensely appreciated. Thank you, Dr. Rimantas Brucas for your training in lithography and wire bonding. Thank you, Dr. Sven Noren, for safeguarding us against potential

hazards in the cleanroom. In addition, my cordial thanks also go to Prof. Per-Erik Hellström and Dr. Yongbin Wang for your assistance in resolving troubles from P5000 and RTP tools.

I am also extremely grateful to all group members. It is a great fortune to work with you. Special thanks to Qitao Hu for delivering those skills of semiconductor processing to me. In a sense, you played a role as a teacher in my earlier PhD life. Thank you, Xi Chen, Xingxing Xu, Shuangshuang Zeng, Chenyu Wen, Shiyu Li, Lukas Jablonka, Chiao-Wei Tseng, Jiyue Wu, Robert Zando, Quentin Palomar, Zheqiang Xu, Yuan Zhu, Funing Liu, Yihan Wang and George Alhoush. Your companionship made this journey unforgettable, and those memories will be treasured throughout my life.

I would also like to thank my colleagues and friends in the division. Thank you, Maria Brandt and Linn Eriksson for the help on daily issues. Many thanks are given to Ngan Pham, Moein Talebian Gevari, Renbin Tong, Yao Yao, Libo Wang, Jiaqi Xing, Yupeng Yang, *etc*.

Many thanks to my friends in Sweden for the wonderful moments we experienced in travelling, board games, parties, and warm talking. Thank you Xueying Kong, Yu Pan, Shan Jiang, Huan Wang, Shengyang Zhou, Chao Xu, Qian Shi, Yuan Cui, Zhenhua Liu, Jing Xu, Chencheng Liang, Chenjie Lu, Yawen Liu, Yayuan Chen, Zunyuan Zheng, Bolin Wu, Lie Tian, Rui Sun, Pei Fu, Jiaqi Lu, Ruochen Wang, Yupei Li, Xiangyu Luan, *etc*.

感谢爸爸妈妈从来无条件的支持与理解，每一份或大或小的进步都离不开你们 27 年来的辛劳和牵挂。能够在你们的爱护下成长就是我生来最大的幸运。

Yingtao Yu
于英涛
2023-10-17

# References

[1] A. Fleming, 'On the Antibacterial Action of Cultures of a Penicillium, with Special Reference to Their Use in the Isolation of B. influenzae', *Clin. Infect. Dis.*, vol. 2, no. 1, pp. 129–139, Jan. 1980, doi: 10.1093/clinids/2.1.129.

[2] E. P. Abraham *et al.*, 'FURTHER OBSERVATIONS ON PENICILLIN', *The Lancet*, vol. 238, no. 6155, pp. 177–189, Aug. 1941, doi: 10.1016/S0140-6736(00)72122-2.

[3] M. I. Hutchings, A. W. Truman, and B. Wilkinson, 'Antibiotics: past, present and future', *Curr. Opin. Microbiol.*, vol. 51, pp. 72–80, Oct. 2019, doi: 10.1016/j.mib.2019.10.008.

[4] C. Lee, 'Life-Cycle Saving in the United States, 1900-90', *Rev. Income Wealth*, vol. 47, no. 2, pp. 165–179, Jun. 2001, doi: 10.1111/1475-4991.00010.

[5] A. I. Dawson, 'BACTERIAL VARIATIONS INDUCED BY CHANGES IN THE COMPOSITION OF CULTURE MEDIA', *J. Bacteriol.*, vol. 4, no. 2, pp. 133–148, Mar. 1919, doi: 10.1128/jb.4.2.133-148.1919.

[6] R. Velez and E. Sloand, 'Combating antibiotic resistance, mitigating future threats and ongoing initiatives', *J. Clin. Nurs.*, vol. 25, no. 13–14, pp. 1886–1889, Jul. 2016, doi: 10.1111/jocn.13246.

[7] J. M. A. Blair, M. A. Webber, A. J. Baylay, D. O. Ogbolu, and L. J. V. Piddock, 'Molecular mechanisms of antibiotic resistance', *Nat. Rev. Microbiol.*, vol. 13, no. 1, pp. 42–51, Jan. 2015, doi: 10.1038/nrmicro3380.

[8] J. L. Martínez, 'Antibiotics and Antibiotic Resistance Genes in Natural Environments', *Science*, vol. 321, no. 5887, pp. 365–367, Jul. 2008, doi: 10.1126/science.1159483.

[9] B. Khameneh, R. Diab, K. Ghazvini, and B. S. Fazly Bazzaz, 'Breakthroughs in bacterial resistance mechanisms and the potential ways to combat them', *Microb. Pathog.*, vol. 95, pp. 32–42, Jun. 2016, doi: 10.1016/j.micpath.2016.02.009.

[10] C. Willyard, 'The drug-resistant bacteria that pose the greatest health threats', *Nature*, vol. 543, no. 7643, pp. 15–15, Mar. 2017, doi: 10.1038/nature.2017.21550.

[11] Y.-Y. Liu *et al.*, 'Emergence of plasmid-mediated colistin resistance mechanism MCR-1 in animals and human beings in China: a microbiological and molecular biological study', *Lancet Infect. Dis.*, vol. 16, no. 2, pp. 161–168, Feb. 2016, doi: 10.1016/S1473-3099(15)00424-7.

[12] S. Puttaswamy, S. K. Gupta, H. Regunath, L. P. Smith, and S. Sengupta, 'A Comprehensive Review of the Present and Future Antibiotic Susceptibility Testing (AST) Systems', *Arch. Clin. Microbiol.*, vol. 09, no. 03, 2018, doi: 10.4172/1989-8436.100083.

[13] L.-L. Zhong *et al.*, 'Coproduction of MCR-1 and NDM-1 by Colistin-Resistant Escherichia coli Isolated from a Healthy Individual', *Antimicrob. Agents Chemother.*, vol. 61, no. 1, pp. e01962-16, Jan. 2017, doi: 10.1128/AAC.01962-16.

[14] B. Behera *et al.*, 'Emerging technologies for antibiotic susceptibility testing', *Biosens. Bioelectron.*, vol. 142, p. 111552, Oct. 2019, doi: 10.1016/j.bios.2019.111552.

[15] A. W. Bauer, W. M. M. Kirby, J. C. Sherris, and M. Turck, 'Antibiotic Susceptibility Testing by a Standardized Single Disk Method', *Am. J. Clin. Pathol.*, vol. 45, no. 4_ts, pp. 493–496, Apr. 1966, doi: 10.1093/ajcp/45.4_ts.493.

[16] J. H. Jorgensen and M. J. Ferraro, 'Antimicrobial Susceptibility Testing: A Review of General Principles and Contemporary Practices', *Clin. Infect. Dis.*, vol. 49, no. 11, pp. 1749–1755, Dec. 2009, doi: 10.1086/647952.

[17] J. A. Poupard, S. F. Rittenhouse, and L. R. Walsh, 'The Evolution of Antimicrobial Susceptibility Testing Methods', in *Antimicrobial Susceptibility Testing*, vol. 349, J. A. Poupard, L. R. Walsh, and B. Kleger, Eds., in Advances in Experimental Medicine and Biology, vol. 349. , Boston, MA: Springer US, 1994, pp. 3–14. doi: 10.1007/978-1-4757-9206-5_2.

[18] J. Picard, 'Applied Veterinary Bacteriology and Mycology: Bacteriological Techniques', *Univ. Pretoria Afrivip Pretoria South Afr.*, 1990.

[19] M. L. Sanchez and R. N. Jones, 'E test, an antimicrobial susceptibility testing method with broad clinical and epidemiologic application', *Antimicrob. Newsl.*, vol. 8, no. 1, pp. 1–7, Jan. 1992, doi: 10.1016/0738-1751(92)90015-3.

[20] M. Balouiri, M. Sadiki, and S. K. Ibnsouda, 'Methods for in vitro evaluating antimicrobial activity: A review', *J. Pharm. Anal.*, vol. 6, no. 2, pp. 71–79, Apr. 2016, doi: 10.1016/j.jpha.2015.11.005.

[21] A. C. Fluit, M. R. Visser, and F.-J. Schmitz, 'Molecular Detection of Antimicrobial Resistance', *Clin. Microbiol. Rev.*, vol. 14, no. 4, pp. 836–871, Oct. 2001, doi: 10.1128/CMR.14.4.836-871.2001.

[22] M. B. Miller and Y.-W. Tang, 'Basic Concepts of Microarrays and Potential Applications in Clinical Microbiology', *Clin. Microbiol. Rev.*, vol. 22, no. 4, pp. 611–633, Oct. 2009, doi: 10.1128/CMR.00019-09.

[23] Y. Li, P. Fan, S. Zhou, and L. Zhang, 'Loop-mediated isothermal amplification (LAMP): A novel rapid detection platform for pathogens', *Microb. Pathog.*, vol. 107, pp. 54–61, Jun. 2017, doi: 10.1016/j.micpath.2017.03.016.

[24] F. R. Cockerill, 'Genetic Methods for Assessing Antimicrobial Resistance', *Antimicrob. Agents Chemother.*, vol. 43, no. 2, pp. 199–212, Feb. 1999, doi: 10.1128/AAC.43.2.199.

[25] E. K. Kastanos, A. Kyriakides, K. Hadjigeorgiou, and C. Pitris, 'A novel method for urinary tract infection diagnosis and antibiogram using Raman spectroscopy', *J. Raman Spectrosc.*, vol. 41, no. 9, pp. 958–963, 2010.

[26] T. J. Moritz, C. R. Polage, D. S. Taylor, D. M. Krol, S. M. Lane, and J. W. Chan, 'Evaluation of Escherichia coli cell response to antibiotic treatment by use of Raman spectroscopy with laser tweezers', *J. Clin. Microbiol.*, vol. 48, no. 11, pp. 4287–4290, 2010.

[27] W.-H. Lee, M.-L. You, P.-K. Wei, P.-S. Chung, K.-L. Lee, and W.-C. Tian, 'Ultra-sensitive and label-free biosensors using surface plasmon resonance of nano-grating structure in nanofluidic preconcentrator', in *2015 IEEE SENSORS*, IEEE, 2015, pp. 1–4.

[28] H. Leonard, S. Halachmi, N. Ben-Dov, O. Nativ, and E. Segal, 'Unraveling antimicrobial susceptibility of bacterial networks on micropillar architectures using intrinsic phase-shift spectroscopy', *ACS Nano*, vol. 11, no. 6, pp. 6167–6177, 2017.

[29] E. Nazemi, W. M. Hassen, E. H. Frost, and J. J. Dubowski, 'Monitoring growth and antibiotic susceptibility of Escherichia coli with photoluminescence of GaAs/AlGaAs quantum well microstructures', *Biosens. Bioelectron.*, vol. 93, pp. 234–240, 2017.

[30] Ö. Baltekin, A. Boucharin, E. Tano, D. I. Andersson, and J. Elf, 'Antibiotic susceptibility testing in less than 30 min using direct single-cell imaging', *Proc. Natl. Acad. Sci.*, vol. 114, no. 34, pp. 9170–9175, Aug. 2017, doi: 10.1073/pnas.1708558114.

[31] J. Johari, Y. Hübner, J. C. Hull, J. W. Dale, and M. P. Hughes, 'Dielectrophoretic assay of bacterial resistance to antibiotics', *Phys. Med. Biol.*, vol. 48, no. 14, p. N193, 2003.

[32] D. C. Spencer, T. F. Paton, K. T. Mulroney, T. J. J. Inglis, J. M. Sutton, and H. Morgan, 'A fast impedance-based antimicrobial susceptibility test', *Nat. Commun.*, vol. 11, no. 1, p. 5328, Oct. 2020, doi: 10.1038/s41467-020-18902-x.

[33] L. M. Goncalves, W. F. Callera, M. D. Sotomayor, and P. R. Bueno, 'Penicillinase-based amperometric biosensor for penicillin G', *Electrochem. Commun.*, vol. 38, pp. 131–133, 2014.

[34] G. Longo *et al.*, 'Rapid detection of bacterial resistance to antibiotics using AFM cantilevers as nanomechanical sensors', *Nat. Nanotechnol.*, vol. 8, no. 7, pp. 522–526, 2013.

[35] P. Bergveld, 'Development of an ion-sensitive solid-state device for neurophysiological measurements', *IEEE Trans. Biomed. Eng.*, no. 1, pp. 70–71, 1970.

[36] P. Bergveld, 'Thirty years of ISFETOLOGY: What happened in the past 30 years and what may happen in the next 30 years', *Sens. Actuators B Chem.*, vol. 88, no. 1, pp. 1–20, 2003.

[37] M. J. Schöning and A. Poghossian, 'Recent advances in biologically sensitive field-effect transistors (BioFETs)', *Analyst*, vol. 127, no. 9, pp. 1137–1151, 2002.

[38] R. E. G. Van Hal, J. C. T. Eijkel, and P. Bergveld, 'A general model to describe the electrostatic potential at electrolyte oxide interfaces', *Adv. Colloid Interface Sci.*, vol. 69, no. 1–3, pp. 31–62, 1996.

[39] D. E. Yates, S. Levine, and T. W. Healy, 'Site-binding model of the electrical double layer at the oxide/water interface', *J. Chem. Soc. Faraday Trans. 1 Phys. Chem. Condens. Phases*, vol. 70, pp. 1807–1818, 1974.

[40] L. Bousse, N. F. De Rooij, and P. Bergveld, 'Operation of chemically sensitive field-effect sensors as a function of the insulator-electrolyte interface', *IEEE Trans. Electron Devices*, vol. 30, no. 10, pp. 1263–1270, 1983.

[41] O. Stern, 'Zur theorie der elektrolytischen doppelschicht', *Z. Für Elektrochem. Angew. Phys. Chem.*, vol. 30, no. 21-22, pp. 508–516, 1924.

[42] B. Enjalbert, P. Millard, M. Dinclaux, J.-C. Portais, and F. Létisse, 'Acetate fluxes in Escherichia coli are determined by the thermodynamic control of the Pta-AckA pathway', *Sci. Rep.*, vol. 7, no. 1, p. 42135, Feb. 2017, doi: 10.1038/srep42135.

[43] B. Xu, 'Glucose over̄ow metabolism and mixed-acid fermentation in aerobic large-scale fed-batch processes with Escherichia coli'.

[44] Y. Sowa and R. M. Berry, 'Bacterial flagellar motor', *Q. Rev. Biophys.*, vol. 41, no. 2, pp. 103–132, 2008.

[45] T. Minamino and K. Imada, 'The bacterial flagellar motor and its structural diversity', *Trends Microbiol.*, vol. 23, no. 5, pp. 267–274, 2015.

[46] S. Kojima and D. F. Blair, 'The bacterial flagellar motor: structure and function of a complex molecular machine', *Int. Rev. Cytol.*, vol. 233, pp. 93–135, 2004.

[47] N. Li, S. Kojima, and M. Homma, 'Sodium-driven motor of the polar flagellum in marine bacteria Vibrio', *Genes Cells*, vol. 16, no. 10, pp. 985–999, 2011.

[48] M. Karimzadehkhouei, B. Ali, M. Jedari Ghourichaei, and B. E. Alaca, 'Silicon Nanowires Driving Miniaturization of Microelectromechanical Systems Physical Sensors: A Review', *Adv. Eng. Mater.*, vol. 25, no. 12, p. 2300007, Jun. 2023, doi: 10.1002/adem.202300007.

[49] R. He and P. Yang, 'Giant piezoresistance effect in silicon nanowires', *Nat. Nanotechnol.*, vol. 1, no. 1, pp. 42–46, Oct. 2006, doi: 10.1038/nnano.2006.53.

[50] J. Hu, M. Yang, G. Gompper, and R. G. Winkler, 'Modelling the mechanics and hydrodynamics of swimming E. coli', *Soft Matter*, vol. 11, no. 40, pp. 7867–7876, 2015, doi: 10.1039/C5SM01678A.

[51] Y. Magariyama, S. Sugiyama, and S. Kudo, 'Bacterial swimming speed and rotation rate of bundled flagella', *FEMS Microbiol. Lett.*, vol. 199, no. 1, pp. 125–129, May 2001, doi: 10.1111/j.1574-6968.2001.tb10662.x.

[52] Y. Kanda, 'Piezoresistance effect of silicon', *Sens. Actuators Phys.*, vol. 28, no. 2, pp. 83–91, Jul. 1991, doi: 10.1016/0924-4247(91)85017-I.

[53] R. Sánchez-Clemente, M. I. Guijo, J. Nogales, and R. Blasco, 'Carbon Source Influence on Extracellular pH Changes along Bacterial Cell-

Growth', *Genes*, vol. 11, no. 11, p. 1292, Oct. 2020, doi: 10.3390/genes11111292.

[54] I. L. M. M. Tack, P. Nimmegeers, S. Akkermans, F. Logist, and J. F. M. Van Impe, 'A low-complexity metabolic network model for the respiratory and fermentative metabolism of Escherichia coli', *PLOS ONE*, vol. 13, no. 8, p. e0202565, Aug. 2018, doi: 10.1371/journal.pone.0202565.

[55] A. R. Fernie, F. Carrari, and L. J. Sweetlove, 'Respiratory metabolism: glycolysis, the TCA cycle and mitochondrial electron transport', *Curr. Opin. Plant Biol.*, vol. 7, no. 3, pp. 254–261, 2004.

[56] B. Xu, M. Jahic, and S.-O. Enfors, 'Modeling of Overflow Metabolism in Batch and Fed-Batch Cultures of Escherichia coli', *Biotechnol. Prog.*, vol. 15, no. 1, pp. 81–90, Feb. 1999, doi: 10.1021/bp9801087.

[57] T.-M. Pan and C.-L. Chan, 'High Sensing Performance of Nanoimprinted HfO2 Sensing Membrane for Electrode-Insulator-Semiconductor pH Sensors', *J. Electrochem. Soc.*, vol. 168, no. 2, p. 027502, 2021.

[58] V. Grudtsov, D. Ryazantsev, O. Gubanova, E. Eganova, and A. Kuznetsov, 'High-Performance ISFET pH Sensor with HfO 2 Sensing Film Using Post-CMOS Processing', in *2023 IEEE Ural-Siberian Conference on Biomedical Engineering, Radioelectronics and Information Technology (US-BEREIT)*, IEEE, 2023, pp. 117–119.

[59] N. A. Curtis, D. Orr, G. W. Ross, and M. G. Boulton, 'Affinities of penicillins and cephalosporins for the penicillin-binding proteins of Escherichia coli K-12 and their antibacterial activity', *Antimicrob. Agents Chemother.*, vol. 16, no. 5, pp. 533–539, Nov. 1979, doi: 10.1128/AAC.16.5.533.

[60] M. A. Kohanski, D. J. Dwyer, B. Hayete, C. A. Lawrence, and J. J. Collins, 'A Common Mechanism of Cellular Death Induced by Bactericidal Antibiotics', *Cell*, vol. 130, no. 5, pp. 797–810, Sep. 2007, doi: 10.1016/j.cell.2007.06.049.

[61] J. J. Foti, B. Devadoss, J. A. Winkler, J. J. Collins, and G. C. Walker, 'Oxidation of the guanine nucleotide pool underlies cell death by bactericidal antibiotics', *Science*, vol. 336, no. 6079, pp. 315–319, 2012.

[62] A. Koul *et al.*, 'Delayed bactericidal response of Mycobacterium tuberculosis to bedaquiline involves remodelling of bacterial metabolism', *Nat. Commun.*, vol. 5, no. 1, p. 3369, 2014.

[63] M. A. Lobritz *et al.*, 'Antibiotic efficacy is linked to bacterial cellular respiration', *Proc. Natl. Acad. Sci.*, vol. 112, no. 27, pp. 8173–8180, Jul. 2015, doi: 10.1073/pnas.1509743112.

[64] D. J. Dwyer *et al.*, 'Antibiotics induce redox-related physiological alterations as part of their lethality', *Proc. Natl. Acad. Sci.*, vol. 111, no. 20, May 2014, doi: 10.1073/pnas.1401876111.

[65] C. M. M. Hasan and K. Shimizu, 'Effect of temperature up-shift on fermentation and metabolic characteristics in view of gene expressions in Escherichia coli', *Microb. Cell Factories*, vol. 7, no. 1, p. 35, Dec. 2008, doi: 10.1186/1475-2859-7-35.

[66] A. R. Lara *et al.*, 'Fast dynamic response of the fermentative metabolism of *Escherichia coli* to aerobic and anaerobic glucose pulses', *Biotechnol. Bioeng.*, vol. 104, no. 6, pp. 1153–1161, Dec. 2009, doi: 10.1002/bit.22503.

[67] N. Paczia, A. Nilgen, T. Lehmann, J. Gätgens, W. Wiechert, and S. Noack, 'Extensive exometabolome analysis reveals extended overflow metabolism in various microorganisms', *Microb. Cell Factories*, vol. 11, pp. 1–14, 2012.

[68] S. Zafar *et al.*, 'Silicon Nanowire Field Effect Transistor Sensors with Minimal Sensor-to-Sensor Variations and Enhanced Sensing Characteristics', *ACS Nano*, vol. 12, no. 7, Art. no. 7, Jul. 2018, doi: 10.1021/acsnano.8b01339.

[69] X. Chen, S. Chen, Q. Hu, S.-L. Zhang, P. Solomon, and Z. Zhang, 'Device Noise Reduction for Silicon Nanowire Field-Effect-Transistor Based Sensors by Using a Schottky Junction Gate', *ACS Sens.*, vol. 4, no. 2, Art. no. 2, Feb. 2019, doi: 10.1021/acssensors.8b01394.

[70] E. Simoen and C. Claeys, 'The low-frequency noise behaviour of silicon-on-insulator technologies', *Solid-State Electron.*, vol. 39, no. 7, pp. 949–960, Jul. 1996, doi: 10.1016/0038-1101(95)00427-0.

[71] X. Chen, S. Chen, S.-L. Zhang, P. Solomon, and Z. Zhang, 'Low-Noise Schottky Junction Trigate Silicon Nanowire Field-Effect Transistor for Charge Sensing', *IEEE Trans. Electron Devices*, vol. 66, no. 9, Art. no. 9, Sep. 2019, doi: 10.1109/TED.2019.2930067.

[72] X. Chen, S. Chen, P. Solomon, and Z. Zhang, 'Top-Bottom Gate Coupling Effect on Low Frequency Noise in a Schottky Junction Gated Silicon

Nanowire Field-Effect Transistor', *IEEE J. Electron Devices Soc.*, vol. 7, pp. 696–700, 2019, doi: 10.1109/JEDS.2019.2929163.

[73] V. A. Kushner, K. Park, D. K. Schroder, and T. J. Thornton, 'Low-Frequency-Noise Spectroscopy of SIMOX and Bonded SOI Wafers', *IEEE Trans. Electron Devices*, vol. 54, no. 12, Art. no. 12, 2007, doi: 10.1109/TED.2007.908894.

[74] 'MOSFETs', *Physics of Semiconductor Devices*. pp. 293–373, 2006. [Online]. Available: https://onlinelibrary.wiley.com/doi/abs/10.1002/9780470068328.ch6

[75] G. Ghibaudo, O. Roux, Ch. Nguyen-Duc, F. Balestra, and J. Brini, 'Improved Analysis of Low Frequency Noise in Field-Effect MOS Transistors', *Phys. Status Solidi A*, vol. 124, no. 2, pp. 571–581, Apr. 1991, doi: 10.1002/pssa.2211240225.

[76] K. Martens *et al.*, '1/f Noise in Fully Integrated Electrolytically Gated FinFETs with Fin Width Down to 20nm', in *25th International Conference on Noise and Fluctuations (ICNF 2019)*, ICLAB, 2019.

[77] K. Martens *et al.*, 'BioFET Technology: Aggressively Scaled pMOS FinFET as Biosensor', in *2019 IEEE International Electron Devices Meeting (IEDM)*, San Francisco, CA, USA: IEEE, Dec. 2019, p. 18.6.1-18.6.4. doi: 10.1109/IEDM19573.2019.8993589.

[78] M. S. Keshner, '1/f noise', *Proc. IEEE*, vol. 70, no. 3, pp. 212–218, 1982.

[79] A. L. McWhorter, '1/f noise and germanium surface properties," Semiconductor Surface Physics', *Phila. Univ. Pa. Press*, vol. 1057, p. 207, 1957.

[80] F. N. Hooge, '1/f noise', *Phys. B C*, vol. 83, no. 1, pp. 14–23, 1976.

[81] E. G. Ioannidis, C. G. Theodorou, T. A. Karatsori, S. Haendler, C. A. Dimitriadis, and G. Ghibaudo, 'Drain-Current Flicker Noise Modeling in nMOSFETs From a 14-nm FDSOI Technology', *IEEE Trans. Electron Devices*, vol. 62, no. 5, Art. no. 5, May 2015, doi: 10.1109/TED.2015.2411678.

[82] K. K. Hung, P. K. Ko, C. Hu, and Y. C. Cheng, 'A unified model for the flicker noise in metal-oxide-semiconductor field-effect transistors', *IEEE Trans. Electron Devices*, vol. 37, no. 3, Art. no. 3, Mar. 1990, doi: 10.1109/16.47770.

[83] K. K. Hung, P. K. Ko, C. Hu, and Y. C. Cheng, 'A physics-based MOSFET noise model for circuit simulators', *IEEE Trans. Electron Devices*, vol. 37, no. 5, Art. no. 5, May 1990, doi: 10.1109/16.108195.

[84] G. Reimbold, 'Modified 1/f trapping noise theory and experiments in MOS transistors biased from weak to strong inversion—Influence of interface states', *IEEE Trans. Electron Devices*, vol. 31, no. 9, Art. no. 9, Sep. 1984, doi: 10.1109/T-ED.1984.21687.

[85] X. Chen, S. Chen, P. Solomon, and Z. Zhang, 'Top-Bottom Gate Coupling Effect on Low Frequency Noise in a Schottky Junction Gated Silicon Nanowire Field-Effect Transistor', *IEEE J. Electron Devices Soc.*, vol. 7, pp. 696–700, 2019, doi: 10.1109/JEDS.2019.2929163.

[86] S. T. Martin, G. P. Li, E. Worley, and J. White, 'The gate bias and geometry dependence of random telegraph signal amplitudes [MOSFET]', *IEEE Electron Device Lett.*, vol. 18, no. 9, pp. 444–446, Sep. 1997, doi: 10.1109/55.622524.

[87] K. Akarvardar, B. M. Dufrene, S. Cristoloveanu, P. Gentil, B. J. Blalock, and M. M. Mojarradi, 'Low-frequency noise in SOI four-gate transistors', *IEEE Trans. Electron Devices*, vol. 53, no. 4, Art. no. 4, Apr. 2006, doi: 10.1109/TED.2006.870272.

[88] M. A. Hopcroft, W. D. Nix, and T. W. Kenny, 'What is the Young's Modulus of Silicon?', *J. Microelectromechanical Syst.*, vol. 19, no. 2, pp. 229–238, Apr. 2010, doi: 10.1109/JMEMS.2009.2039697.

[89] B. Lee and R. E. Rudd, 'First-principles study of the Young's modulus of Si ⟨001⟩ nanowires', *Phys. Rev. B*, vol. 75, no. 4, p. 041305, Jan. 2007, doi: 10.1103/PhysRevB.75.041305.

[90] Y.-S. Sohn *et al.*, 'Mechanical Properties of Silicon Nanowires', *Nanoscale Res. Lett.*, vol. 5, no. 1, p. 211, Jan. 2010, doi: 10.1007/s11671-009-9467-7.

[91] J.-K. Kuo, P.-H. Huang, W.-T. Wu, and C.-M. Lu, 'Mechanical and fracture behaviors of defective silicon nanowires: combined effects of vacancy clusters, temperature, wire size, and shape', *Appl. Phys. A*, vol. 114, no. 4, pp. 1247–1256, Mar. 2014, doi: 10.1007/s00339-013-7886-x.

[92] C. S. Smith, 'Piezoresistance Effect in Germanium and Silicon', *Phys. Rev.*, vol. 94, no. 1, pp. 42–49, Apr. 1954, doi: 10.1103/PhysRev.94.42.

[93] A. Koumela *et al.*, 'Piezoresistance of top-down suspended Si nanowires', *Nanotechnology*, vol. 22, no. 39, p. 395701, Sep. 2011, doi: 10.1088/0957-4484/22/39/395701.

[94] J. S. Milne, A. C. H. Rowe, S. Arscott, and Ch. Renner, 'Giant Piezoresistance Effects in Silicon Nanowires and Microwires', *Phys. Rev. Lett.*,

vol. 105, no. 22, p. 226802, Nov. 2010, doi: 10.1103/PhysRevLett.105.226802.

[95] Q. Hu, S. Chen, P. Solomon, and Z. Zhang, 'Ion sensing with single charge resolution using sub–10-nm electrical double layer–gated silicon nanowire transistors', *Science Advances*, vol. 7, no. 49. p. eabj6711, 2021.

[96] T. H. P. Chang, 'Proximity effect in electron-beam lithography', *J. Vac. Sci. Technol.*, vol. 12, no. 6, pp. 1271–1275, 1975.

[97] V. Passi, E. Dubois, A. Lecestre, A. S. Linde, B. D. Bois, and J.-P. Raskin, 'Design guidelines for releasing silicon nanowire arrays by liquid and vapor phase hydrofluoric acid', *Microelectron. Eng.*, vol. 103, pp. 57–65, Mar. 2013, doi: 10.1016/j.mee.2012.09.002.

[98] P. H. Langer and J. I. Goldstein, 'Impurity redistribution during silicon epitaxial growth and semiconductor device processing', *J. Electrochem. Soc.*, vol. 121, no. 4, p. 563, 1974.

[99] O. Karabelchtchikova and R. D. Sisson, 'Carbon diffusion in steels: A numerical analysis based on direct integration of the flux', *J. Phase Equilibria Diffus.*, vol. 27, pp. 598–604, 2006.

[100] G. L. Vick and K. M. Whittle, 'Solid solubility and diffusion coefficients of boron in silicon', *J. Electrochem. Soc.*, vol. 116, no. 8, p. 1142, 1969.

[101] A. T. Fiory and K. K. Bourdelle, 'Electrical activation kinetics for shallow boron implants in silicon', *Appl. Phys. Lett.*, vol. 74, no. 18, pp. 2658–2660, 1999.

# Acta Universitatis Upsaliensis

*Digital Comprehensive Summaries of Uppsala Dissertations from the Faculty of Science and Technology* 2326

Editor: The Dean of the Faculty of Science and Technology

A doctoral dissertation from the Faculty of Science and Technology, Uppsala University, is usually a summary of a number of papers. A few copies of the complete dissertation are kept at major Swedish research libraries, while the summary alone is distributed internationally through the series Digital Comprehensive Summaries of Uppsala Dissertations from the Faculty of Science and Technology. (Prior to January, 2005, the series was published under the title "Comprehensive Summaries of Uppsala Dissertations from the Faculty of Science and Technology".)